THE DEVELOPMENT OF THE STRONG-COUPLING QUANTUM DOT MICROSCOPE

By

Eric William Goodwin

A DISSERTATION

Submitted to
Michigan State University
in partial fulfillment of the requirements
for the degree of

Physics— Doctor of Philosophy

2020

ABSTRACT

THE DEVELOPMENT OF THE STRONG-COUPLING QUANTUM DOT MICROSCOPE

By

Eric William Goodwin

A surge of experimental and theoretical advances in the past two decades have sustained a vigorous interest in studying Majorana zero modes (MZM) in condensed matter systems. Majorana zero modes are spinless zero-energy bound excitations which form a highly degenerate ground-state manifold displaying non-Abelian braiding statistics, making this quasiparticle an attractive candidate for topological quantum computing. Beyond the potential computing applications, MZMs are of general scientific interest, combining two paradigms of condensed matter physics that have dominated research in different eras; superconductivity and topological physics. Evidence confirming the existence of these quasiparticles is mounting, with zero-bias conductance tunneling providing the strongest signature to date, but the development and utilization of other techniques is necessary to provide a smoking-gun signature of Majorana zero modes. Among the most promising proposals are schemes harnessing the quantized nature of quantum dots (QDs) coupled to MZMs, which would probe the most compelling aspects of MZMs.

In this thesis, I will present the development of the Strong-Coupling Quantum Dot Microscope (SCQDM), a novel scanning quantum dot probe potentially capable of uniquely distinguishing Majorana zero modes. In particular, the SCQDM is well suited for Majorana samples that lend themselves to study with scanning probe techniques. The SCQDM utilizes a capacitance scheme, in contrast to related transport techniques, to measure the full counting statistics of electrons entering the apex quantum dot while positioned within

tunneling range of a MZM. We present functional testing of the two most important aspects of the microscope: single electron counting and angstrom distance tunneling at 300 mK. In the Appendix, I will present STM results taken on topological insulator/superconductor bilayer structures, showing evidence of the topologically protected surface state (TPSS) proximitizing to the surface of the superconducting overlayer. Evidence of the Bi_2Se_3 TPSS leaking into a Nb overlayer will be shown, an effect we have dubbed the Dual Topological Proximity Effect (DTPE).

This dissertation is dedicated to my wife Christina Goodwin and my parents Robert and Colleen Goodwin.

ACKNOWLEDGEMENTS

The first person I would like to thank is my constant companion in the lab Michael Gottschalk. Our hours spent together transferring cryogenics, tackling striped samples or deciphering The Colloquium are among my fondest memories in physics. Our conversations, which inevitably ended in politics, always made for lively affairs. I consider you a true friend and I hear they may be hiring in Maryland…

Thank you to Dr. Reza Loloee and Dr. Baokong Bi for your constant experimental support and patience. Thank you to Dr. Mark Dykman and Dr. Johannes Pollanen for helping keep the condensed matter journal club well-attended, and Mark in particular for asking the hard questions that always led to a deeper understanding of the physics. A special thanks to Dr. Scott Pratt for Netflix recommendations when I was sick my first year in graduate school. It was a small gesture, but it reassured me my graduate career was still on track.

Of course, I would also like to thank my committee: Dr. Norman Birge, Dr. Phil Duxbury, Dr. Wade Fisher, and Dr. Filomena Nunes. Each one of our meetings tested my abilities, but I always walked away from them confident and motivated thanks to your continued support.

During my time in graduate school I had the pleasure of overlapping with a number of great physicists and people. Thank you to Joe Kitzman, Kaedon Cleland-Host, Justin Lane, Bob Klaes, Niyaz Beysengulov, and others for the constant friendship and physics discussions. The basement was a better place with you all in it.

Thank you to my parents, Rob and Colleen Goodwin, for enabling me to follow this path, and hours of home improvement. I would not have survived the end of my PhD without you. I would also like to thank my wife Christina. Your constant patience with long hours during data runs, genuine interest in my research, and care for our family kept me on this path. I look forward to where our lives will take us.

Most importantly, I would like to thank my teammates on the 2020 IM basketball championship squad. Entering a PhD program in hopes of winning an IM championship was a questionable move on my part, but you all made it well worth it.

Lastly, I would like to thank Dr. Stuart Tessmer, the single most important figure in my professional and scientific career. For nearly a decade you have believed in my abilities as a scientist, even when my own confidence was faltering. Your enduring optimism and love of teaching physics were instrumental in my success as a researcher. Beyond physics, you are among the most kind and caring individuals I have ever had the pleasure of meeting, and I will cherish our relationship throughout my life.

The work in this dissertation was completed with support from the Department of Education through GAANN Award No. USDE P200A140215, the Peter Schroeder Endowment, the U.S. Department of Energy, Office of Science, Basic Energy Sciences, under Award DE-SC0017888, and the University of Michigan College of Engineering and the Michigan Center for Materials Characterization for use of instruments and staff assistance.

TABLE OF CONTENTS

LIST OF FIGURES

Chapter 1

Introduction

The development of Scanning Tunneling Microscopy [1] in 1981 ushered in a new class of experimental tools for studying condensed matter physics. Collectively known as scanning probe microscopes (SPM), the hallmark of this class of instruments is the ability to precisely position a scanning probe anywhere on the surface of a sample, a distinct advantage over existing methods. In addition to carrying out traditionally static measurements, the ability to dynamically move the experimental probe permits new types of experiments to be done, such as topographic mapping of a tip-sample interaction of the sample surface. The exact interaction mechanism for each SPM probe with the sample is specific to the application, but the relative ubiquity of these types of probes points to the versatility of dynamic probe methods across science. In this thesis, I will focus on condensed matter physics experiments performed using two types of scanning probe microscopy: Scanning Tunneling Microscopy and Strong-Coupling Quantum Dot Microscopy.

Scanning Tunneling Microscopy (STM) is arguably the most successful SPM in condensed matter physics. The basis for STM is the quantum mechanical phenomena known as tunneling, which allows electrons to travel in ways forbidden by classical mechanics. In particular, electrons are capable of traveling through small insulating layers between two conductors. The STM probe is a sharp conductive tip positioned within angstroms of the sample surface. By applying a voltage between the tip and the sample,

electrons from the conductive tip can tunnel through the insulating vacuum gap into the conductive sample. This movement of electrons generates a small current, which is detected and amplified by sensitive electronics. This tunneling current serves as the basis for a number of experiments. By holding the tunneling current constant and rastering the tip across the surface, a topographic map of the sample can be generated. If instead the tip is stationary, and the voltage between tip and sample swept, the local electron density of states can be studied, providing important information about the electronic properties of the sample. Combining the two techniques results in a powerful third measurement known as conductance mapping, which gives spatial information about the density of states. Conductance mapping is especially important for the study of localized energy modes, enabling researchers to pinpoint these modes in energy and real space.

The second SPM method, the Strong-Coupling Quantum Dot Microscope (SCQDM) is a **new tool developed in this dissertation**. The specific goal of the SCQDM is to measure signatures of Majorana zero modes. For this reason, Majorana physics is an important part of this thesis. However with respect to experimental data, Majorana studies will be carried out by my successors in the Tessmer group. The measurements presented here demonstrate the core functionalities of this probe.

Borrowing concepts from Scanning Single Electron Transistor Microscopy (SSETM)[2], subsurface charge accumulation imaging (SCAI)[3], and STM, the SCQDM is potentially a powerful tool for the study of localized effects in condensed matter systems. The SCQDM consists of a sharp glass scanning probe with a small patch of aluminum at the apex, and two metallic leads on either side of the probe. The small island of aluminum at

the apex is known as a quantum dot (QD), a system small enough to show resolvable quantization effects. Specifically, the energy required to add or subtract a single electron from the quantum dot, referred to as the charging energy, is large enough to be resolved spectroscopically. By creating the leads attached to the quantum dot asymmetrically, one lead allows for tunneling single electrons into and out of the quantum dot, while the other lead is coupled capacitively, acting as a passive observer to the changing electron occupation of the quantum dot. By utilizing a High Electron Mobility Transistor (HEMT), the minute change in the capacitance between the quantum dot and capacitance lead can be measured.[4]

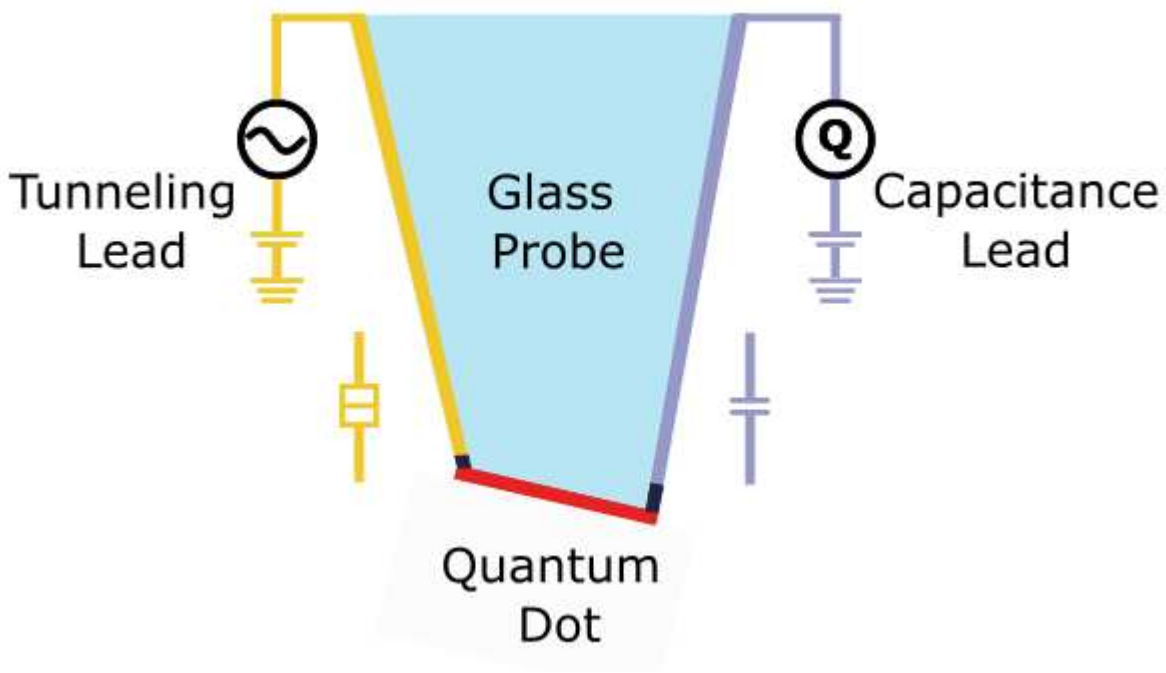

Figure 1.1: Schematic of the Strong-Coupling Quantum Dot Microscope. An asymmetric tip design protects the sensitive tunnel junction (gold-side) from surface interactions, while the capacitance junction (purple-side) provides charge sensing capabilities. An apex quantum dot (red) enables single charge transfer measurements, a key functionality for studying Majorana zero modes. The basis of the SCQDM probe is an etched glass cylinder. Both electrical leads and the quantum dot are aluminum. Tunnel junctions (black) between the leads and quantum dot are aluminum oxide.

In this way, the SCQDM acts as a sophisticated single electron counter. The asymmetrical design further allows the probe to couple strongly to surface features via angstrom distance tunneling, without risk of damaging the sensitive tunneling lead junction. This innovation is the main advantage of the SCQDM over the SSETM, which is not brought within traditional tunneling range of the surface of a sample due to having two sensitive tunnel junctions near the quantum dot apex. The measurement principle relies on the full counting statistics of adding electrons to the quantum changing when coupled strongly to surface features, the most pertinent to this thesis being Majorana Zero Modes.[5]

One of the greatest conceptual simplifications in condensed matter physics is the concept of quasiparticles, or treating complicated many-body effects as *quasi*-particles in the sample with properties that account for the many-body effects. Majorana zero modes (MZMs) are such a quasiparticle found at zero energy. Analogous to Majorana fermions in particle physics [6], a MZM is a particle that is its own antiparticle; indeed, two identical MZMs annihilate each other when brought together. Since MZMs form in pairs, it is necessary to separate the pair spatially to study the physics. Restricted to two spatial dimensions, Majorana zero modes belong to a special class of particles known as anyons. Unlike fermions or bosons, anyons pick up a non-trivial phase when two anyons are exchanged twice. Further, MZMs possess non-Abelian braiding statistics, which indicates that not only are the exchanges of particles non-trivial, but also the order of the exchanges is important.[7] These two properties, non-trivial exchanges and non-trivial ordering of exchanges, have given rise to immense interest in MZMs as the basis for a quantum computer.[8] The reason is that computations for MZMs occur in a highly degenerate ground state, resulting in topological protection of the computation, a distinct advantage

over other quantum computing platforms.[9] Given the potential for quantum information and the fundamental interest in the exotic physics involved, Majorana zero modes are extremely attractive systems to study for theorists and experimentalists alike.

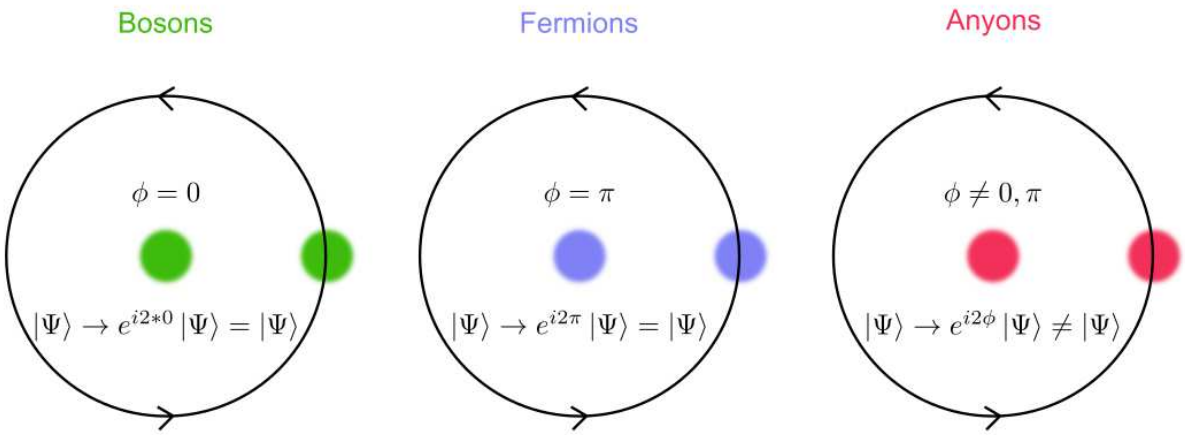

Figure 1.2: Exchange statistics for three types of particles. One exchange between identical particles picks up a dynamical phase ϕ in the two particle wavefunction. A complete rotation (twice exchange) picks up a dynamical phase of 2ϕ. Bosons and fermions return to the original wavefunction upon this twice exchange, while anyons pick up a nontrivial phase of 2ϕ. If this anyon is non-Abelian, this twice exchange takes the original state to a different degenerate state within a highly degenerate ground state manifold, the basis for topological quantum computing using these excitations as the qubit.

Realizing Majorana zero modes has been an intense experimental focus the last decade.[10] Four key ingredients are necessary to engineer MZMs in condensed matter systems: superconductivity, strong spin-orbit coupling, magnetism, and localization/separation. The first three ingredients allow you to create something called a novel topological superconductor, which in principle can support MZMs; the fourth ingredient puts in a symmetry-breaking edge to allow isolated MZMs to localize. [11]

Superconductivity is a well-studied phenomenon by which materials experience zero electrical resistance once cooled below a critical temperature. More importantly to Majorana phenomenon, superconductors form a degenerate ground state comprised of Cooper pairs, which are a bound state of two electrons. The formation of Cooper pairs into a Bose-Einstein condensate opens a gap in the electronic density of states, while providing a symmetry known as particle-hole symmetry. The superconducting energy gap and particle-hole symmetry are the key facets in the creation of Majorana zero modes that superconductors provide. Next, spin-orbit coupling is a strong interaction between the quantum mechanical spin of electrons, and the electron's momentum through a material. Materials with strong spin-orbit coupling, including topological insulators, require that these degrees of freedom are locked together. A somewhat naïve picture of this effect is a material that requires right moving electrons to have spin up and left moving electrons to have spin down. Spin-orbit coupling serves to introduce momentum dependence into the Cooper pairs, providing effective p-wave pairing and removing spin conservation. Third, some magnetic component is required to totally spin-polarize the system, breaking time reversal symmetry and lifting spin-degeneracy. Lastly, Majorana zero modes are particles that are their own antiparticles, and only manifest in pairs. To avoid instantly destroying the Majorana zero modes via annihilation, the pair must be localized and spatially separated. Further, the presence of a domain wall is required to realize these excitations more generally. Several schemes exist to separate these pairs, most notably 1D nanowires systems [12] and superconducting vortices[13]. The combination of these four ingredients, with some clever engineering and parameter choices, should in principle result in the creation of Majorana zero modes.

The central focus of this thesis is the development of a tool to identify and study Majorana zero modes. The most commonly performed measurement of a MZM signature is a quantized zero bias conductance peak.[14,15] Owing to the perfect Andreev reflection MZMs manifest, a quantized zero bias conductance peak is a signature of MZM. Unfortunately, zero-bias conductance peaks can be produced by more common physics, such as the Kondo effect and Andreev bound states.[16] An innovation first proposed in 2011 should provide an even stronger signature of the MZM.[17] This next signature is the unique modification of the single electron counting statistics of a quantum dot (QD) coupled strongly to a MZM. The hybridization of the QD with the MZM results in a distinct single electron signal, which cannot be mimicked by other trivial QD couplings.

The development of this scanning quantum dot microscope potentially enables quantum dot study of an entire class of Majorana samples that are better suited to probing by scanning probe methods as compared to lithographically-defined quantum dots. This includes the "native" topological superconductor FeTeSe,[18] magnetic chain samples,[19] and topological insulator / superconductor heterostructures.[20]

This dissertation will focus on the underlying theory and experimental aspects of the physics discussed above. First, I will introduce the established experimental methods used in the dissertation in Chapter 2. Next, I will introduce the theory of Majorana zero modes in Chapter 3, to motivate the following Chapter 4, which will explore the theory of the Strong-Coupling Quantum Dot Microscope. Chapter 5 is concerned with the fabrication process of the Strong-Coupling Quantum Dot Microscope. Finally, Chapter 6 will present the functional testing of the SCQDM showing its viability as a scanning probe technique. A

discussion of the dual topological proximity effect, additional fabrication details, and extended theory discussion will be found in the appendices.

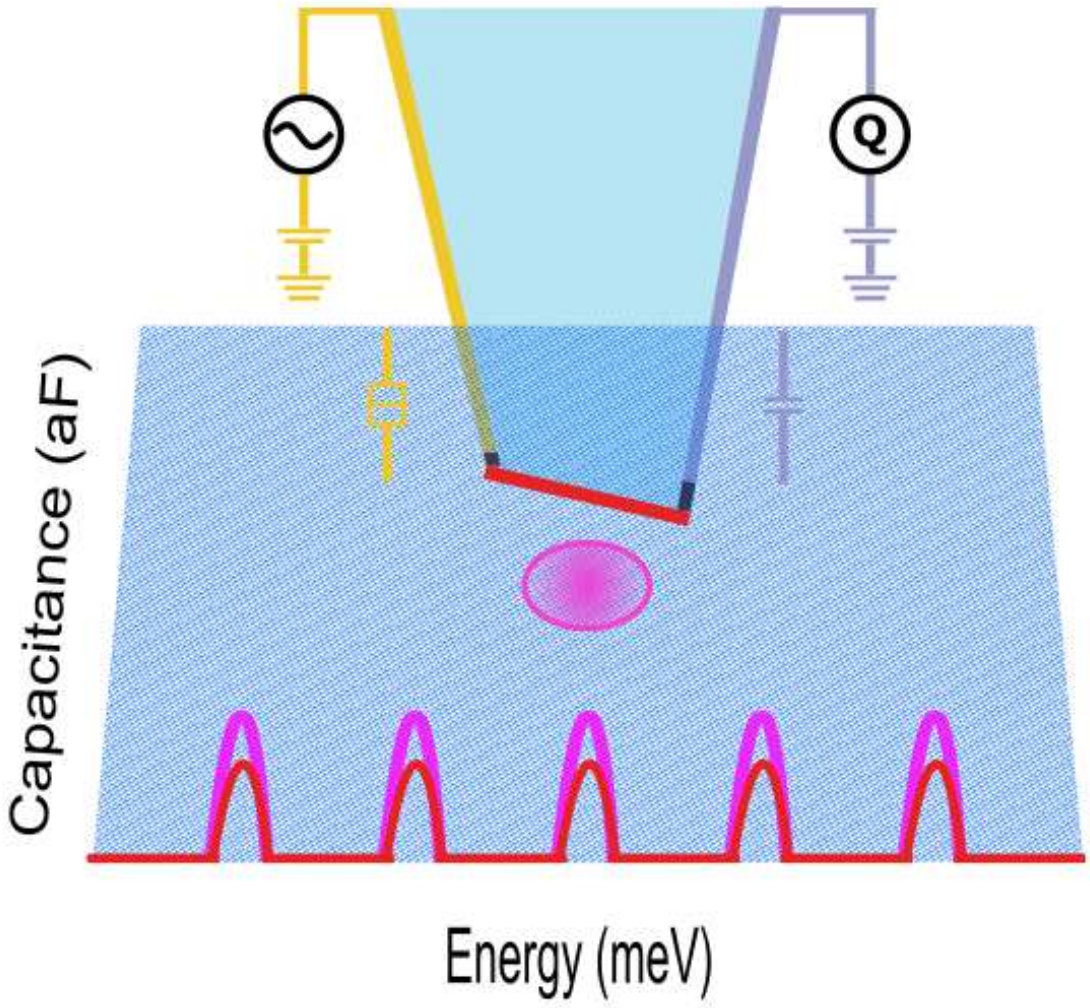

Figure 1.3: Qualitative schematic of the SCQDM measurement of Majorana zero modes. As compared to the capacitance signal for an isolated QD (red plot), a QD coupled strongly to a MZM (purple plot) should see a unique change in the capacitance signal. Here, the change is shown as an increase in the mean peak height of 1.5x, but the underlying theory is more complex. This will be addressed in Section 3.3. Energy and voltage are used interchangeably and are related via E=eV.

Chapter 2

Experimental Methods

Scanning tunneling microscopy (STM) is among the most successful scanning probe methods employed in condensed matter research. The first section is devoted to the theory of quantum tunneling, as well as brief introductions to two types of measurements performed using STM: topography and spectroscopy. The basic component of every measurement is achieved using a sharp, conductive tip brought within a nanometer of the surface of a sample. By applying a bias voltage between the tip and the sample, electrons can tunnel from the tip into the sample (or vice versa), generating a small current which can be amplified and recorded. The ability to tunnel across the small insulating vacuum gap is enabled thanks to quantum tunneling. Recording the response of the tip's piezoelectric control, tunneling current, and the change in the tunneling current can provide information about the topography of the sample, the local electronic density of states, and the spatial presence of various energy modes. The last section will detail the cryostat and microscope scan head used for both STM and Strong-Coupling Quantum Dot Microscopy (SCQDM), the latter of which is the focus of Chapter 4.

2.1 Quantum Tunneling

Quantum tunneling is the basis of scanning tunneling microscopy. Consider an electron traveling to the right towards a potential barrier.

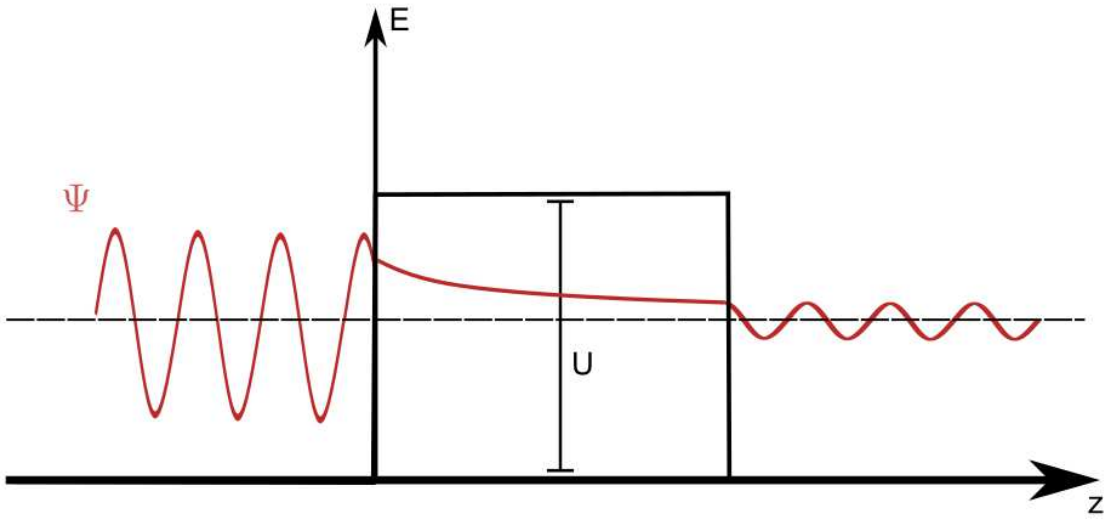

Figure 2.1: Free electron traveling towards a potential barrier. Plotted in red is the real part of the electron's wavefunction as a function of position z. Classically forbidden, the electron's wavefunction is capable of "tunneling" through the barrier U due to the quantum mechanical nature of the wavefunction.

The Schrodinger equation for the electron's wave function is

$$\frac{-\hbar}{2m}\frac{d^2}{dz^2}\psi(z) + U(z)\psi(z) = E\psi(z) \tag{2.1}$$

The solution to the Schrodinger equation in the presence of the potential is

$$\begin{aligned} \psi(z) &= \psi(0)\, e^{-\kappa z} \quad E < U \\ \psi(z) &= \psi(0) e^{\pm ikz} \quad E > U \end{aligned} \tag{2.2}$$

where $\kappa = \sqrt{2m(U-E)}/\hbar$ and $k = \sqrt{2m(E-U)}/\hbar$. The solution to the Schrodinger's equation for the electron wave function is sinusoidal at energies higher than the barrier, indicating unperturbed propagation in the z direction, and exponentially decaying for energies lower than the barrier potential U. Classically, the electron would be forbidden from entering the potential barrier, but quantum mechanics enables the wavefunction,

while still rapidly decaying in amplitude, to penetrate the potential barrier for energy E<U. If the barrier is small enough, the electron can tunnel through the barrier and regain its sinusoidal form on the other side, albeit reduced in amplitude. Quantum tunneling is the basis for STM and for the single electron box, discussed in Section 4.2.

The preceding discussion is simple and general for any tunneling phenomena. Next, we will expand on this basic introduction to better understand the relationship between distance and tunneling current in the context of STM.[21] Consider a sharp STM tip with work function ϕ_{tip} separated from a metallic surface with work function ϕ_{sample} by a distance σ in the z-direction. For an applied bias voltage $e * V < \phi_{sample}, \phi_{tip}$, the potential barrier can be approximated as arectangular barrier, with barrier height U equal to the average of the tip and sample work functions ϕ_{ave}. The width of the barrier is dictated by the tip-sample separation σ.

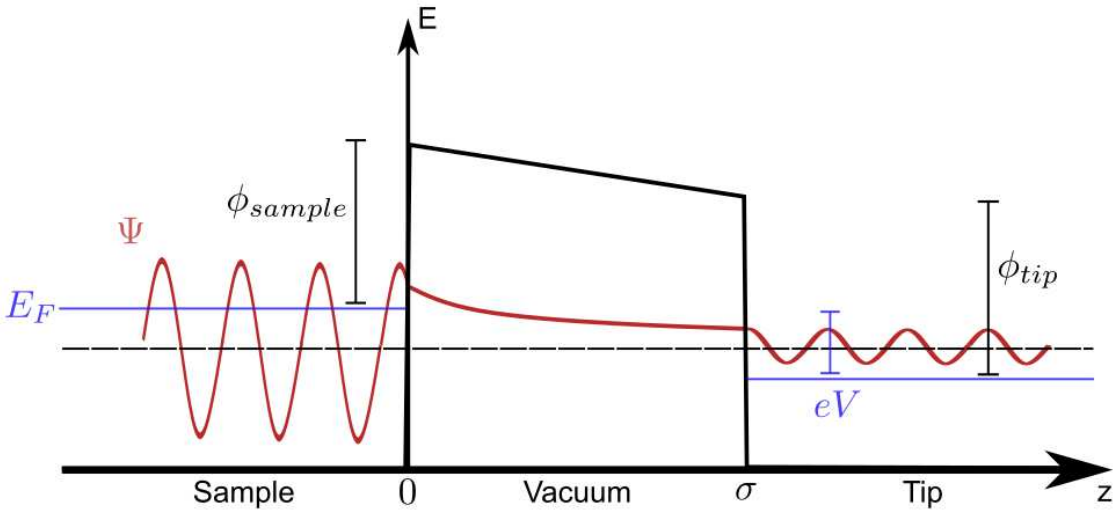

Figure 2.2: Quantum tunneling between a conductive sample and tip. The real part of the electron wavefunction (red) is capable of traversing the vacuum gap, driven by an applied bias voltage eV.

The tunneling electron upon entering the barrier experiences an exponential decay of its wavefunction in space, dictated by the barrier height $e^{\kappa} \alpha e^{\sqrt{\phi_{ave}}}$. Once the electron has tunneled through the barrier, it returns to a reduced amplitude. The reduction in wavefunction amplitude provides a measurement of the transmission coefficient Γ, which once squared is proportional to the tunneling current I. We therefore conclude

$$I \alpha e^{-2\kappa\sigma} \tag{2.3}$$

Equation 2.3 shows the tunneling current through the potential barrier drops off exponentially with distance and barrier height. In the context of STM, the tunnel current drops roughly an order of magnitude for each angstrom of increased distance between tip and sample.

2.2 Topography

Topography is the most basic functionality provided by STM, but its simplicity belies its power as a surface science tool.[22] Topography allows surface characterization on the order of single atoms, allowing researchers to study defects in the lattice and other interesting atomic structures. Topography is performed by fixing the applied bias voltage and tunneling current set point between tip and sample. The tip is then rastered back and forth across the sample surface while the tip's piezoelectric tube moves the tip up and down to maintain the set point current. In general, missing lattice sites and insulating features require the tip to push in, whereas raised step edges and more conductive features require the tip to be pulled out. Plotting the piezoelectric feedback across the scanned area

provides this topographic information and is pivotal in characterizing the sample surface for defect states and structures of interest, such as finding a Josephson junction in a sparse array.

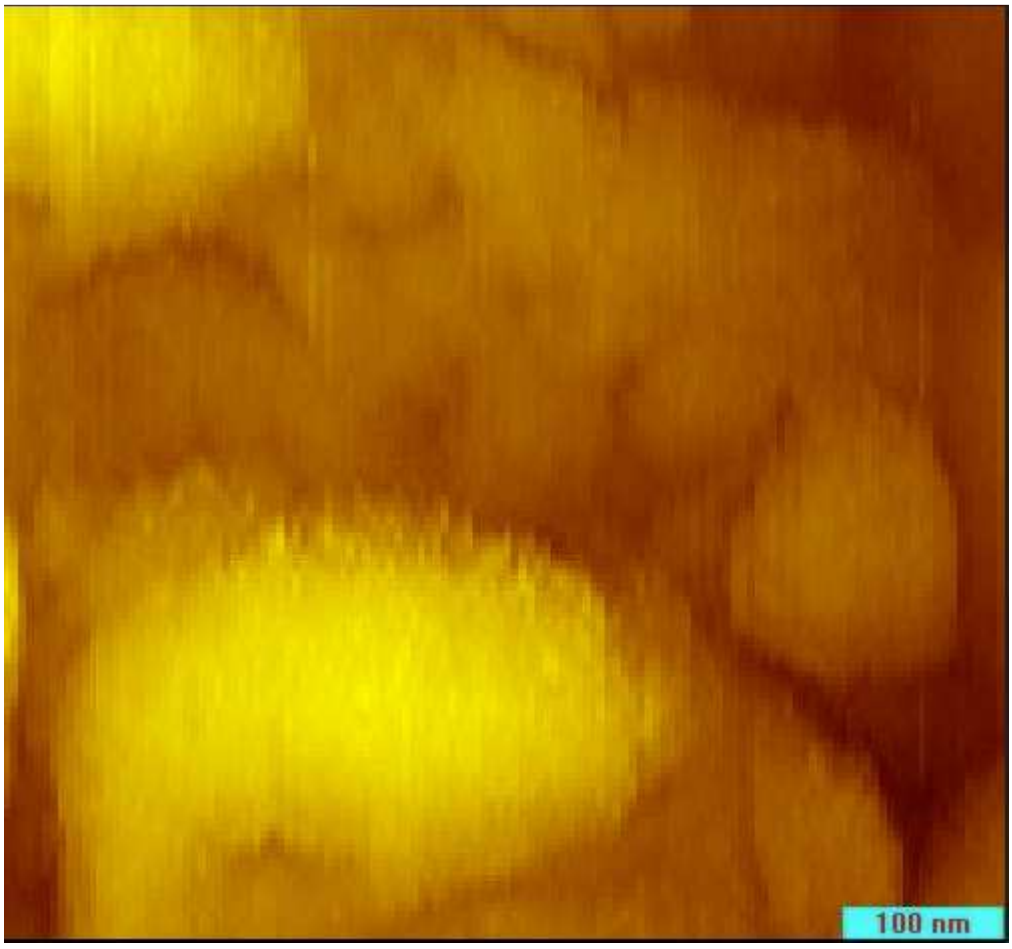

Figure 2.3: Topography performed on 150 nm niobium sputtered onto a silicon substrate. The large circular feature near the bottom of the image is approximately 5 nm tall.

2.3 Scanning Tunneling Spectroscopy

Perhaps the most powerful measurement performed using STM is scanning tunneling spectroscopy (STS). By fixing the tip's position above the sample surface, turning off the piezoelectric feedback, and sweeping the applied DC bias voltage with an AC excitation

voltage superposed, I-V curves and dI/dV can be recorded. At zero temperature, dI/dV is a direct measurement of the local electronic density of states (defined later), making STS an ideal tool to study interesting electronic systems such as topological insulators, superconductors, and Majorana zero modes. At finite temperatures, the measured signal ends up being a convolution of thermal broadening and local density of states, but at low enough temperatures this effect is small. STS presented in this thesis was performed at 4.2K or lower.

To better understand the relationship between local electronic density of states and dI/dV at finite temperature we will go through a standard calculation. The first assumption required is that tunneling transitions occur at constant energy with an applied bias voltage, which is to say the transitions are discrete. The cumulative tunneling current measured is the sum of contributions from each energy level. As mentioned, thermal broadening effects contribute to the tunneling current, which can be expressed using the convolution of the Fermi function

$$f(E) = \frac{1}{1+e^{E/(k_B T)}} \tag{2.4}$$

and the sample's density of states $N_s(E)$, a measure of the number of available electronic states at a given energy level. The occupation of the electronic states in the sample is then given by $N_s(E)f(E)$. Assuming electron tunneling from sample to tip, tunnel events can only occur for filled sample states if a degenerate state is empty inside of the tip (of course, the argument works in reverse as well). The number of tunnel events is further given by $N_t(E - eV)[1 - f(E - eV)]$. The tunneling current from sample to tip can be written as

$$I_{s\to t}\alpha \int_{-\infty}^{\infty}|\Gamma|^2 N_s(E)f(E)N_t(E-eV)[1-f(E-eV)]dE \tag{2.5}$$

where Γ is again the transmission coefficient for tunneling described earlier. Restricting tunneling to close to the Fermi level, where most measurements are performed, allows to a good approximation for this quantity Γ to be independent of E, allowing us to pull it out of the integral. The net tunnel current, which is the difference between tip-sample and sample-tip tunneling events, is then given by

$$I_{net}\ \alpha \int_{-\infty}^{\infty} N_s(E)N_t(E-eV)[f(E)-f(E-eV)]dE \tag{2.6}$$

The use of metallic STM tips (such as PtIr) enables a further simplification to this equation since the density of states for metals near the Fermi level is constant. Differentiating with respect to the applied bias voltage eV then gives us a relationship between dI/dV and local density of states (the net subscript has been dropped)

$$\frac{dI}{dV}(V)\ \ \alpha \int_{-\infty}^{\infty} N_s(E)\left[\frac{\partial f(E-eV)}{\partial(eV)}\right]dE \tag{2.7}$$

Equation 2.7 clearly shows the sample density of states is proportional to dI/dV of the tunnel current. The derivative of the Fermi function is a bell-curve centered at $E = eV$ with a width scaling with temperature k_bT and unitary area beneath the curve. At finite temperatures, this factor is either comparable or small compared to an applied AC excitation voltage, so for practical reasons can be ignored even at very low, but finite temperature. For example, at 4.2 K thermal broadening contributes 1.267 meV of smearing, which is smaller than a typical AC excitation of 4 meV. At zero temperature, this term drops out completely and there is direct proportionality as promised. As an example

of spectroscopy, Figure 2.4 shows several dI/dV curves acquired on the same superconducting niobium sample shown in Figure 2.3 at 4.2 K.

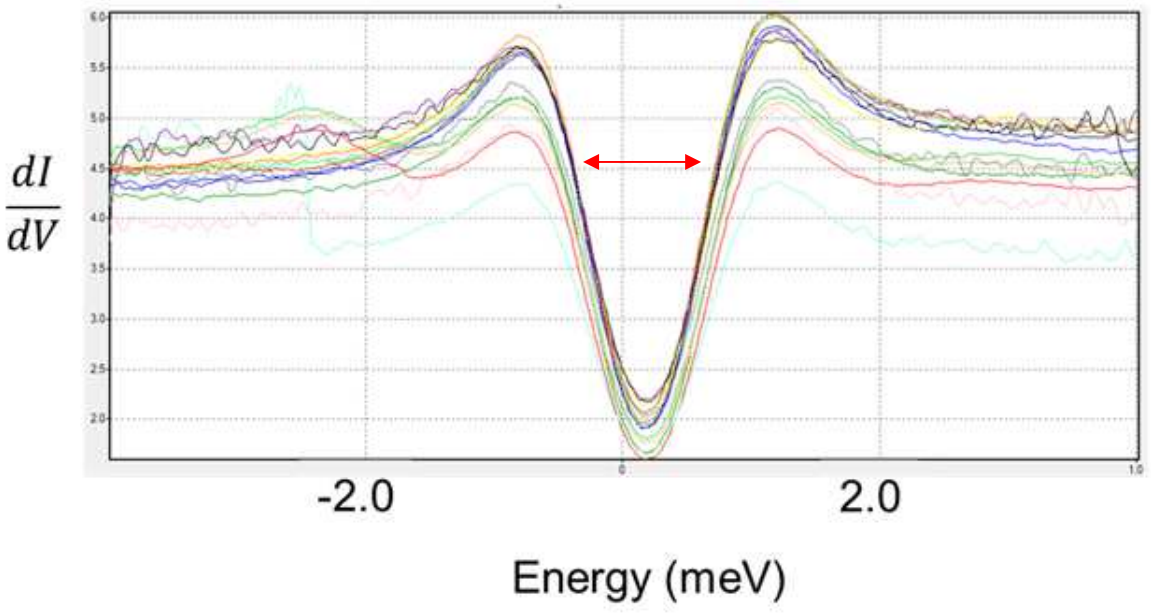

Figure 2.4: Individual spectroscopy curves taken on a 150 nm Nb film on silicon at 4.2 K. Stable STM tips, such as the one used to take this data, are powerful probes of the local electronic density of states. This sample displays clear superconducting coherence peaks and a thermally broadened superconducting energy gap (indicated with red arrows).

2.4 Cryostat

Low-temperature physics is typically done at one of four temperature ranges: 77 K, 4.2 K, 300 mK, or 10 mK. 77 K is accessible using liquid Nitrogen, a cheap and readily available cryogen. 4.2 K is reached using liquid Helium, a more expensive cryogen but necessary for the study of most superconductors. 300 mK can be achieved using either wet cryostats employing a Helium-3 insert or dry dilution refrigerator, the latter of which is capable of

reaching 10s of mK. This thesis is concerned with experiment performed at 300 mK, achieved with a wet cryostat with integrated Helium-3 system.

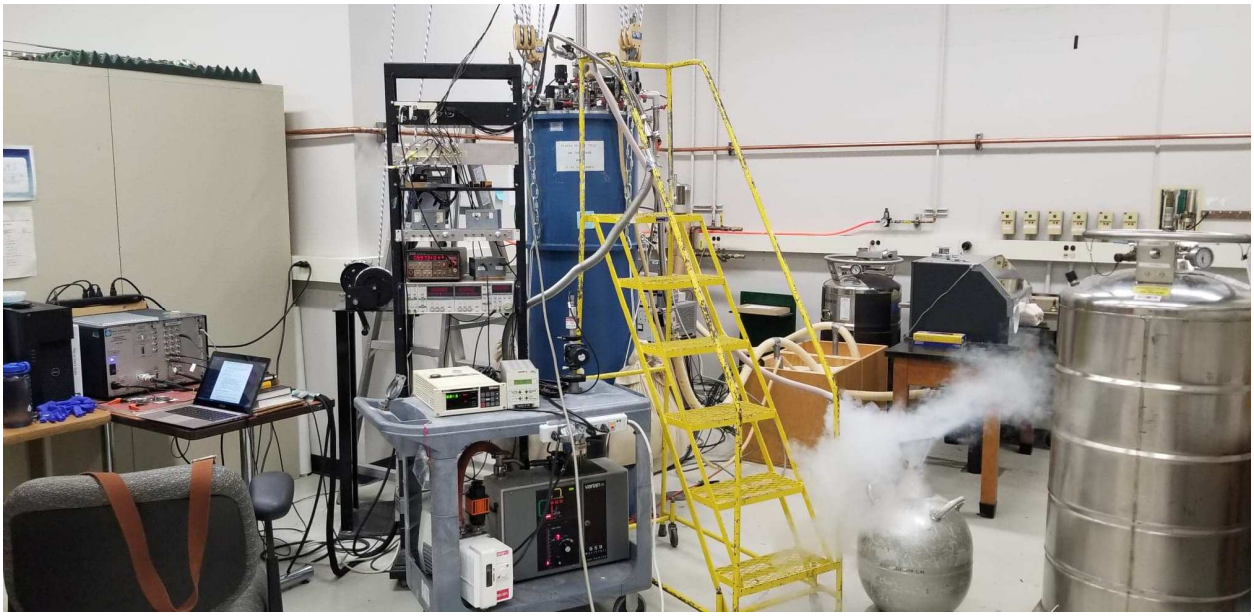

Figure 2.5: Image showing a cryogenic cooldown of the cryostat. The cryostat (blue, background), vacuum cart (foreground), and liquid Helium dewar (right) are shown. At this moment, liquid Nitrogen is being removed and collected from the cryostat to make room for liquid Helium as part of the precooling process. Sub-300 mK temperatures will be later achieved through Helium-3 recondensation.

The cryostat, schematic below, consists of several vacuum chambers and a cryogenic bath which serve to isolate the sample space from the room temperature environment and cool the sample space, respectively. The three main methods of heat exchange are conduction, convection, and radiation. By maintaining vacuums in each of these chambers, the dominate thermal exchange process within the cryostat becomes radiation, the slowest method of heat transfer among the three. Therefore, maintaining high vacuums is necessary for the longevity of low temperature experiments.

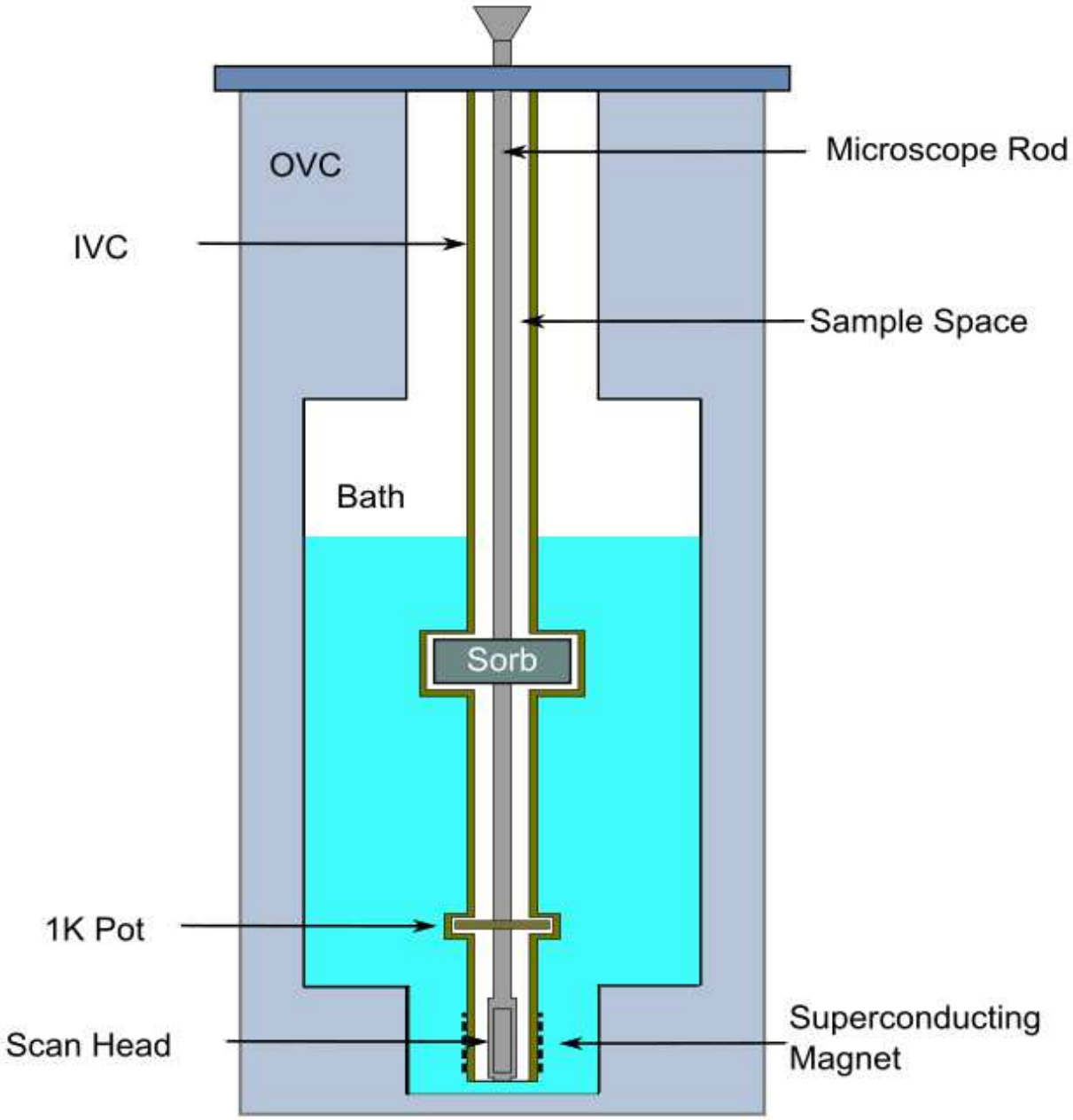

Figure 2.6: Cross-section of the top loading Helium-3 cryostat. The items labeled are in general cylindrical in shape with a hole in the middle to accommodate the microscope. The microscope rod contains the electronic leads from the scan head to connect to room temperature electronics. The Outer Vacuum Chamber (OVC) and Inner Vacuum Chamber (IVC) are maintained at high vacuum to isolate the liquid Helium-4 bath, which contains the superconducting magnet at the bottom of the cryostat. The sample space contains the microscope rod, sorb, 1K pot, and scan head of the microscope. The sorb contains Helium-3, which can be released and condensed at the 1K pot, filling the sample space below and achieving a base temperature of 270 mK at the microscope scan head.

The Outer Vacuum Chamber (OVC) is the first barrier between the ambient room temperature environment and the low temperature sample space where the experiment is carried out. The OVC is a large stainless-steel vacuum chamber that houses multiple layers of mylar sheets inside. The thin mylar sheets serve to prevent thermal transfer between room temperature and the interior wall of the OVC. Prior to every cryogenic data run, the OVC is pumped out using a turbomolecular pump to 10^{-6} Torr over the course of two days. A single threaded port is the only access into the OVC and is only opened when pumping out the OVC. Special care is taken when pumping out the OVC to ensure only small pressure gradients between the OVC and vacuum cart hose to protect the mylar sheets.

The interior wall of the OVC is the exterior wall of the cryogenic bath. The cryogenic bath is roughly 60 L in volume and stores one of two cryogenic liquids depending on the experiment. 77 K experiments use liquid Nitrogen in the bath to maintain the sample space temperature with a typical hold time of 2 weeks. Experiments which take place at 4.2K or lower call for a precooling stage of liquid Nitrogen, which is then blown out of the cryogenic bath and replace with liquid Helium-4, for an experimental hold time of roughly 4-6 days at 4.2 K. The bath has an exhaust port, which allows for a controlled release of cryogenic gases as the liquid evaporates while maintaining a constant bath pressure. The constant pressure is achieved with a soft pressure relief valve. The entry port for the bath is a thin tube which goes to the bottom of the bath, which helps mitigate losses upon cryogenic transfer.

The interior wall of the cryogenic bath is the exterior wall of the Inner Vacuum Chamber (IVC). The IVC is a small, empty vacuum chamber that serves two purposes

during a data run. First, the IVC is filled with gaseous Helium-4 to help equilibrate the temperature of the sample space by providing conduction between it and the cryogenic bath. Once the microscope reaches 4.2 K, the IVC is then pumped to 10^{-6} Torr to thermally isolate the sample space from the cryogenic bath, an especially important step for experiments performed at 300 mK.

The interior wall of the IVC is the exterior wall of the sample space where the microscope is ultimately placed during a data run. The sample space is a thin tube running almost the entire length of the cryostat. In the middle of this tube is a carbon-based sorption pump. The sorption pump is a passive pump that relies on the enormous surface area of charcoal for gas molecules to condense on at low temperatures. At the bottom of the sample space is the 1K pot, and surrounding the bottom of the sample space, but housed in the cryogenic bath, is a superconducting magnet, capable of reaching 10T.

To reach 300 mK, the temperature at which the Strong-Coupling Quantum Dot Microscope is operated, we utilize a process known as Helium-3 recondensation. The sorption pump contains a large quantity of Helium-3, which is released from the pump into the sample space by heating the sorb to 40 K. As the Helium 3 is released, the 1K pot is filled with liquid Helium-4 from the main bath and pumped on by a mechanical pump in the sub-basement to reach 1.2 K. The released He-3 then recondenses onto the 1K pot surface and falls into the Helium-3 pot at the bottom of the sample space. The sorb heater is then turned off, and the sorption pump slowly begins to cool while simultaneously pumping on the liquid Helium-3, which results in the temperature of the Helium-3 dropping below 300

mK. This Helium-3, depending on the details of the recondensation, can then be maintained for up to 100 hours of operation at sub-300 mK temperatures.

Additionally, the entire cryostat is suspended by bungee cables hung from the ceiling of the laboratory to decouple the microscope apparatus from building vibrations.

Figure 2.7: The entire cryostat, microscope included, can be suspended off the floor by bungee cables, decoupling the cryostat from low frequency building vibrations.

2.5 Microscope Scan Head

The microscope scan head, a Besocke design,[23] consists of three carrier piezoelectric tubes that allow coarse xyz positioning of the sample and one central tip piezoelectric tube responsible for fine xyz positioning and control of the tip during measurements.

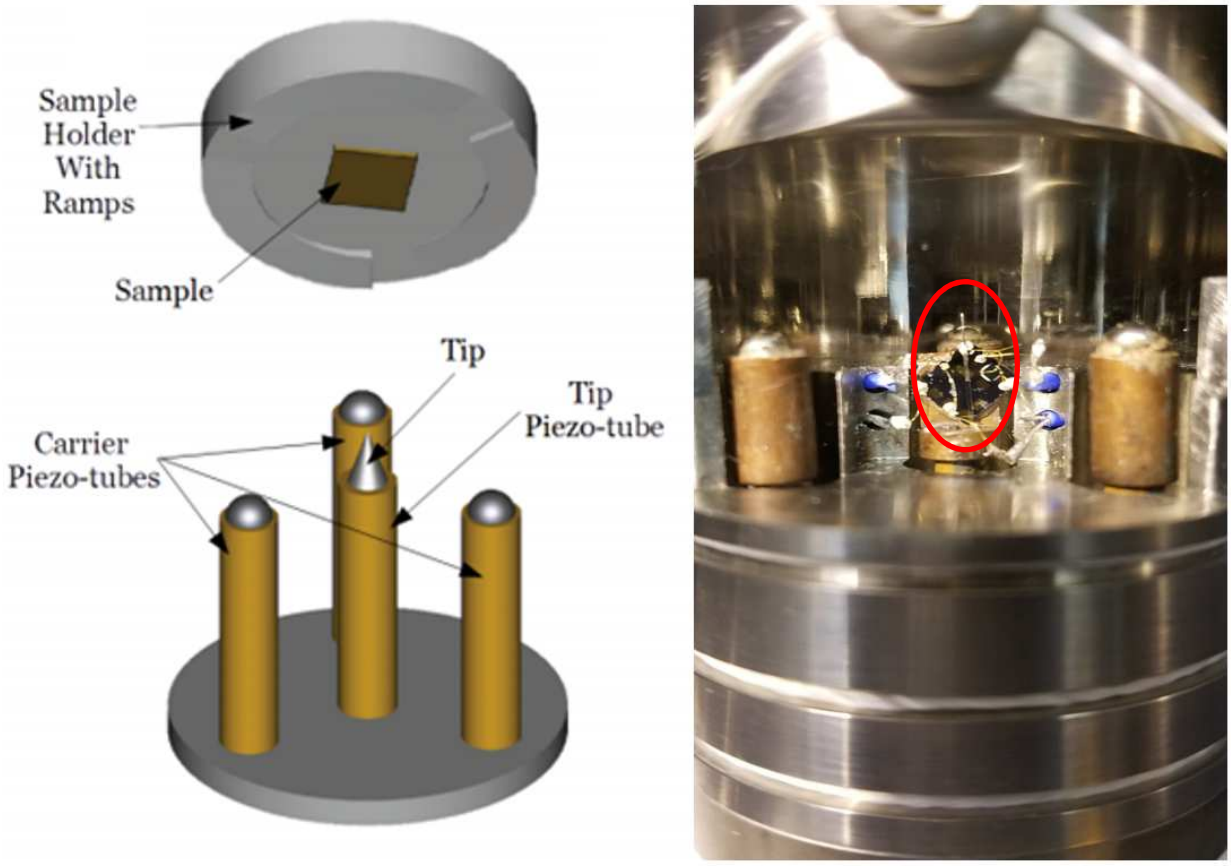

Figure 2.8: The Besocke design microscope scan head. Left: Schematic showing three outer piezo-tubes, responsible for coarse positioning, and a middle piezo-tube, responsible for fine positioning. Positioned above the tip and piezo-tubes is the sample holder with ramps. The ramps enable the stick-slip method to move the sample either up or down, depending on the applied waveform. Right: Image of the scan head, shown with the SCQDM (red circle) mounted. Five electrical leads (one of which is ground) are used to connect the SCQDM to room temperature electronics through the microscope rod.

Piezoelectric materials change shape in response to applied voltages, allowing for extremely precise manipulations. The piezoelectric tubes are segmented into quadrants, each of which can be independently biased with voltage waveforms. With the recent upgrades to our STM control electronics, bipolar 150V waveforms can be applied. To achieve coarse positioning in the xyz directions, pulsed waveforms, either sawtooth or parabolic in shape, are applied to the quadrants of the carrier piezoelectric tubes, which slowly extend and quickly retract to achieve an aggregate twisting motion of the sample. The ramps on which the sample is mounted stick during the slow extension, then slip during the rapid retraction. This stick-slip method, when combined with different pulse patterns, achieves the xyz coarse positioning. Approach of the tip to the sample surface additionally involves the tip piezoelectric tube. After one pulse cycle for coarse approach to the carrier piezoelectric tubes, the tip piezoelectric tube is extended to its maximum z range to determine if the tip is within tunneling range. If the tunneling current of the tip matches the set point current, the tip will retract fully and prompt the user that the tip is in range. If the tip is out of range, the cycle continues.[23] The approach parameters are highly customizable with the new control system, but in general this is the safest and most practical approach setting.

Mounted to the top of the three carrier piezoelectric tubes are brass cylinders capped with steel spheres. The sample contacts these spheres to do the stick-slip motion. A wire threaded through the center of the piezoelectric tube connects the steel spheres to the STM control box and is responsible for the bias voltage between tip and sample. The tip is kept grounded in this configuration. To ensure proper application of the bias voltage, it is

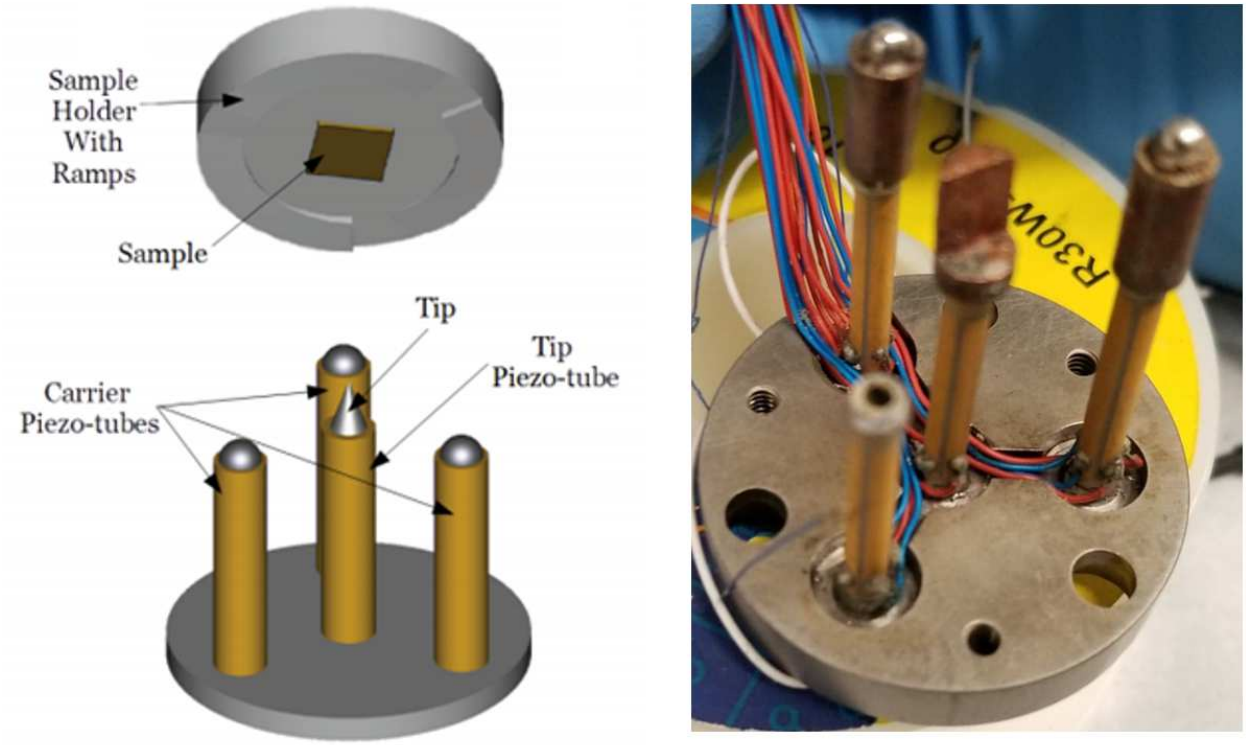

Figure 2.9: Image of the piezo tubes taken during a microscope rebuild. Left: Reproduction of Figure 2.8. Right: Each piezo tube has four external connections, one for each quadrant, with an extra wire threaded through the center. Pulsed waveforms applied to each quadrant of the walking piezo tubes (scanning piezo tube) are responsible for coarse (fine) positioning and approach. Shown here is one piezo tube missing the bronze cap, which is responsible for applying the bias voltage between tip and sample.

important the sample disk is electrically connected to the sample ramps (readily achieved under normal circumstances). Additionally, an Allen Bradley resistor is mounted just above the microscope scan head to serve as a thermometer during microscope push downs.

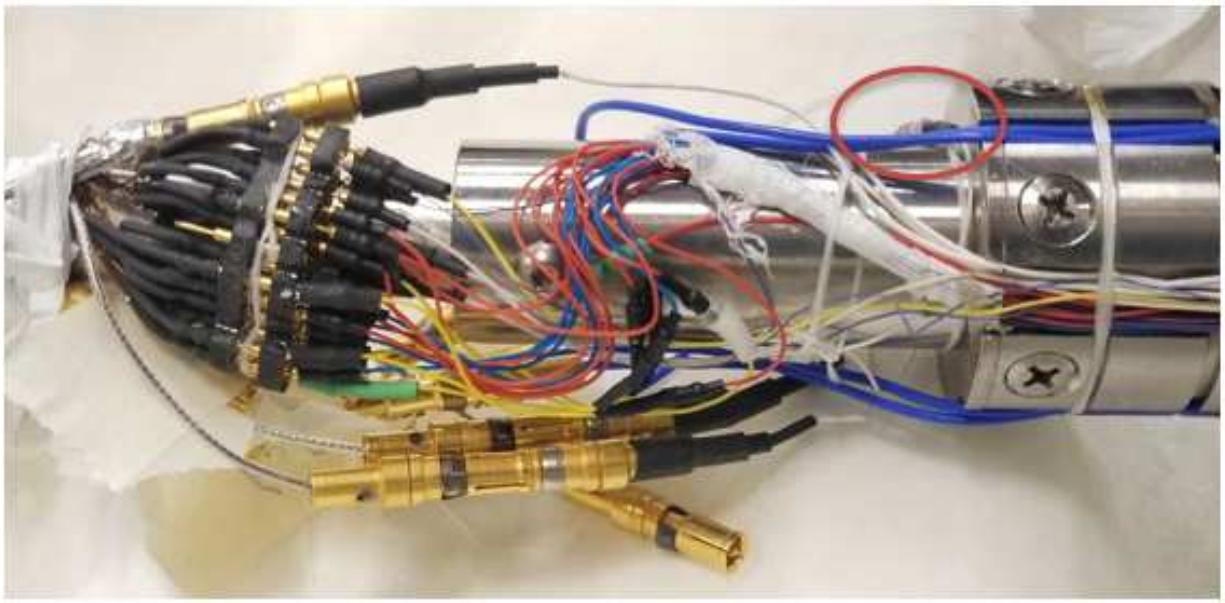

Figure 2.10: Image of the connections above the functional scan head during a rebuild. The blue wires are the four electrical leads used to connect the SCQDM. The large connections are the bias voltages supplied through each of the walking piezo tubes. The smaller connections in black are generally connected to the outside of the piezo tube and are responsible for sending the walking waveform to the appropriate quadrant. Lastly, circled in red is the Allen Bradley resistor, which sits just above the scan head and tracks the temperature of the microscope during push downs.

Chapter 3

Theory: Majorana Zero Modes

This thesis is concerned with the development of a tool, the Strong-Coupling Quantum Dot Microscope, to study Majorana zero modes (MZMS) / Majorana bound states (MBS). While the SCQDM is particularly suited to study a subset of Majorana samples, the details of the sample to be studied is not the focus of this chapter. The goal here instead is to provide a working knowledge of Majorana physics from the perspective of an experimentalist, applicable across Majorana architectures. This section motivates the development of the SCQDM, but ultimately no SCQDM Majorana measurements are presented in this thesis.

The physics of Majoranas is filled with subtleties. Pedagogical introductions to Majorana physics tend to focus on a particular platform for realizing Majorana zero modes. The Majorana nanowire platform is best introduced with the Kitaev toy model,[12] where the discussion then shifts to real semiconducting nanowires and new physics is slowly introduced and parameters tuned to realize MZMs. Another popular method is introducing topological superconductivity and realizing Majorana modes as a natural conclusion to adding boundaries to the system. Each approach to introducing these complicated systems has its own strengths, weaknesses, and peculiarities. In this chapter, we will first introduce the general properties of MZMs and use these properties to motivate four general ingredients necessary to realizing MZMs: superconductivity, strong spin-orbit coupling, magnetism, and localization/separation. Superconductivity will be discussed in detail in the following section. We will then introduce some of the main signatures of MZMs, ending

with a discussion of the QD-MZM measurement which most pertains to the SCQDM. Interested readers can find extended discussions on the other three main ingredients, topological physics, and a discussion on quantized Majorana conductance in Appendix C. For this thesis, the only Majorana excitation considered are Majorana zero modes or Majorana bound states; 1D dispersing Majorana channels and edge modes are another realization of this physics but will not be considered here. [24]

3.1 Introduction

A good starting point to introduce Majorana modes is the creation and annihilation operators for fermions ($f^\dagger$ and f respectively).[25] In the context of condensed matter physics, this is equivalently the creation of a hole f and the creation of an electron $f^\dagger$. These operators satisfy the following standard anticommutation relation and square to zero.

$$\begin{aligned} f^\dagger f + f f^\dagger &= 1 \\ f^2 = f^{\dagger 2} &= 0 \end{aligned} \tag{3.1}$$

The fermionic operators can be expressed in terms of Majorana operators γ if the above relations hold. One such form that maintains these relations is

$$f^\dagger = \frac{1}{2}(\gamma_1 + i\gamma_2), f = \frac{1}{2}(\gamma_1 - i\gamma_2) \tag{3.2}$$

This can be thought of as separating the complex fermionic operator into its real and complex parts. Unlike the fermionic operators we started with, Majorana operators γ_1 and

γ_2 cannot be thought of in the context of traditional creation and annihilation operators. To make this clear, we can explicitly express the Majorana operators in terms of the fermionic operators

$$\begin{aligned} \gamma_1 &= f + f^\dagger \\ \gamma_2 &= -i(f - f^\dagger) \end{aligned} \tag{3.3}$$

using either Equation 3.2 or Equation 3.3 it can also be shown that

$$\gamma_1 = \gamma_1^\dagger, \gamma_2 = \gamma_2^\dagger \tag{3.4}$$

Equation 3.4 implies that **Majorana modes are particles that are their own antiparticle,** while Equation 3.3 requires that Majorana modes display equal characteristics of holes $f^\dagger$ and electrons f. Additionally, the Majorana modes γ_1 and γ_2 are inextricably linked; every individual Majorana mode is paired to another individual Majorana mode. A single Majorana mode is then neither empty nor filled, as is the case with fermionic modes, but is necessarily part of a bound state of two Majorana modes, which together comprise the filled or empty state of a single fermionic mode. The parity of this fermionic mode is ultimately the classical output of a topological quantum computer based on Majorana modes [9].

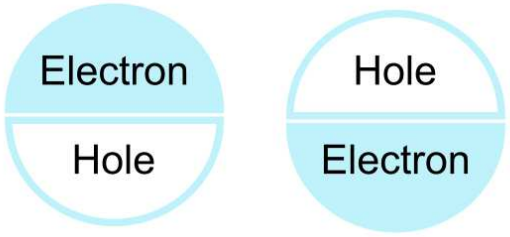

Figure 3.1: Majorana zero modes are particles that are their own antiparticle. Additionally, these excitations form in pairs, each displaying equal characteristics of electron and hole.

It is tempting to think of Majorana modes as the bound state of an electron and hole. A common quasiparticle excitation studied is the exciton, a bound state of an electron in the conduction band and a hole in the valence band of a semiconductor.[26] This quasiparticle is also equal parts hole and electron, which at first glance appears to be the same as a Majorana mode. The difference is subtle. The exciton is a bound state of two fermions, one hole and one electron, that comprise an overall bosonic excitation following Bose-Einstein statistics, much like Cooper pairs in a superconductor. A single Majorana mode is one part of a bound state of two Majorana modes, each of which constitutes equal electron/hole characteristics. As a result, Majorana modes are neither bosons nor fermions but rather satisfy exotic anyonic statistics. These anyonic exchange statistics make MZMs attractive for quantum computation, as mentioned in the introduction. Majorana modes can be studied in proximitized semiconducting systems but are distinct from excitons.

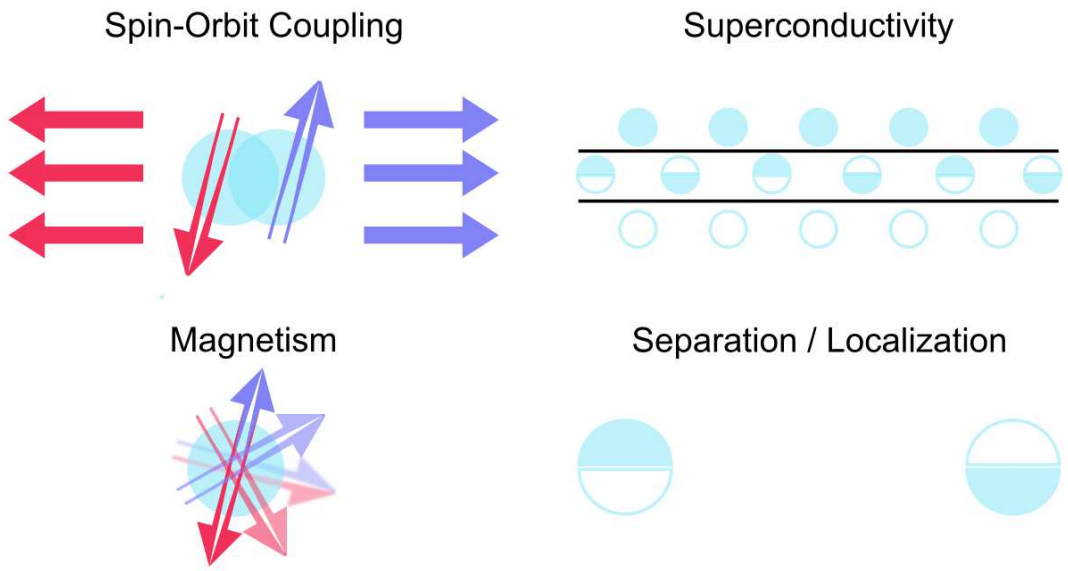

Figure 3.2: Four ingredients for creating Majorana modes. Superconductivity provides a particle-hole symmetric system for these excitations to arise. Spin-orbit coupling removes spin-conservation, while magnetism lifts spin-degeneracy. Introduction of a boundary allows the Majorana zero modes to manifest.

The next property of MZMs will require introducing the first of the four general ingredients towards realizing MZMs: superconductivity. Majorana modes are electron/hole symmetric excitations. A natural place to search for these excitations is in superconducting systems, due to their intrinsic particle-hole symmetry. Particle-hole symmetry can be realized in other systems, but for the purpose of this thesis we will restrict ourselves to superconductors, as this is the most accessible experimental realization of particle-hole symmetry. BCS superconductivity treats electron and hole excitations equally, requiring a hole like excitation at -E to have an electron like excitation at +E. A consequence of this particle-hole symmetry is Majorana modes must occur at zero energy, the only energy for which electronic states and hole-like states are degenerate. Therefore, **Majorana modes are zero energy excitations found in superconductors.**

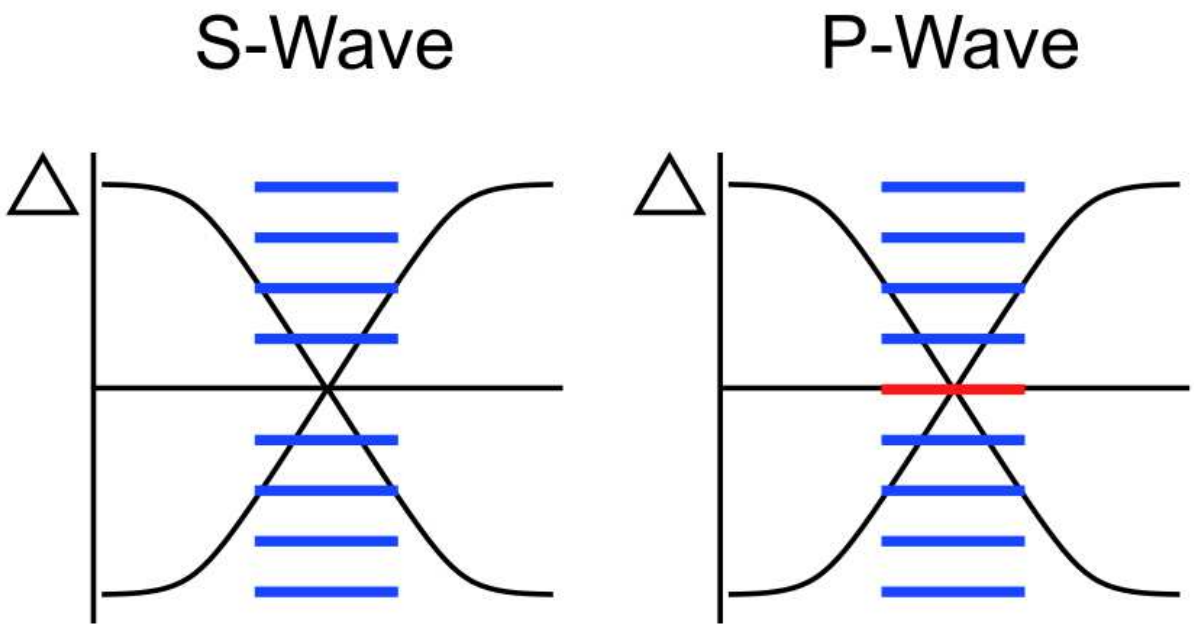

Figure 3.3: Comparison of accessible single particle energy levels inside a superconducting vortex. The presence of zero-point motion for s-wave superconductors prohibits a zero-energy mode. This forbiddance is lifted with p-wave pairing.

Unfortunately, this is not the complete story. Zero energy modes are not accessible with traditional s-wave superconductivity due to zero-point motion.[27] Instead, exotic p-wave superconductivity is necessary to realize these zero energy modes.

Put simply, the Cooper pairs comprising the superconducting condensate require momentum dependence in their pairing potential to allow these zero energy excitations to form. The pairing must be of the spin triplet form (p-wave), rather than the spin singlet form (s-wave). The simplest way to introduce effective p-wave pairing is coupling the superconductor to a strong spin-orbit coupling material, one which locks the spin and momentum degrees of freedom of electrons together. To then correct the previous statement: **Majorana modes are zero energy excitations found in effective p-wave pairing superconducting systems**. This can be achieved by proximitizing strong spin-orbit coupling materials using a trivial s-wave superconductor, among other methods.

The introduction of the Majorana operators and superconductivity up to this point have ignored the spin degeneracy of Majorana zero modes. The particle-antiparticle nature of MZMs requires these excitations to be spinless, as the spin degree of freedom would introduce degeneracy and result in quasiparticles that are not their own antiparticle. Superconducting and spin-orbit coupling samples have spin degrees of freedom, but luckily a completely spin-polarized system behaves similarly enough to a spinless system to realize MZMs. It is tempting to think spin-orbit coupling alone can lift the degeneracy, but the spin-orbit interaction obeys time reversal symmetry, the consequence of which is Kramer's degeneracy. Strong spin-polarization and the breaking of time reversal symmetry (Kramer's degeneracy) can be achieved by locally introducing magnetic

defects/atoms or more simply by applying an external magnetic field. Therefore, **Majorana zero modes are spinless zero energy excitations found in the superconducting energy gap of an effective p-wave superconducting system.**

The bulk-boundary correspondence is a key concept for creating Majorana modes and is described in some detail in Appendix C. For now, one of the requirements for creating MZMs is the presence of a boundary. The boundary between a topological superconductor, the more formal name for the effective system we have created thus far, and a trivial material allows for MZMs to manifest. Another key consideration is the fact that Majorana hybridization occurs when there is significant overlap of the two MZMs wavefunctions, which tends to obfuscate robust signatures of MZMs (this hybridization is necessary for other measurements). The simplest way to separate two Majorana zero modes is to localize each member of a given pair at the ends of a nanowire.[12] MZMs can also be localized to magnetic defects, Abrikosov and Josephson vortices, and antidots.[28]

Presented here was not an exhaustive account of Majorana physics, but rather an intuitive introduction to the main ingredients of any Majorana system. As such, specific details are lacking, and some beautiful arguments for Majorana physics are missing. Elegant discussion on particular systems can be found in reference [25], including p-wave superconductivity and the Majorana nanowire.

The preceding discussion started with a simple expansion of the fermionic creation and annihilation operators into the Majorana basis which illuminated some of the properties of Majorana modes. The rest of the properties were introduced as part of the construction of a system supporting MZMs. The following sections will introduce

superconductivity, the first and arguably most important Majorana ingredient. Discussion of the other three ingredients can be found in Appendix C.

3.2 Superconductivity

Superconductors are materials that, once cooled below a critical temperature T_c, exhibit two effects. The first effect is a change from finite to zero resistance through the material. The second effect (Meissner effect) is the expulsion of magnetic fields from within the material. In 1911 Kamerlingh Onnes cooled mercury below its critical temperature and measured the first transition from finite to zero resistance through any material. The study of superconductivity since has been punctuated by exceptional theoretical and experimental efforts. In 1935 the London brothers developed the first phenomenological theory to help explain the behavior of superconductors in electromagnetic fields,[29] followed by the seminal BCS framework in 1957 by Bardeen, Cooper, and Schrieffer, which provided the first theory describing the microscopic interaction giving rise to superconductivity.[30] The 1980s saw a dramatic disruption in the field with the discovery of lanthanum barium copper oxide (LBCO) and yttrium barium copper oxide (YBCO), the first of a new class of high temperature superconductors which become superconducting above the condensation temperature of liquid Nitrogen (77K). The promise of superconducting qubits for quantum computing and exotic topological superconductivity are now at the forefront of condensed matter research, the latter of which is the focus of the SCQDM. The following sections will introduce the BCS framework then extend this framework in the context of Bougolibov quasiparticles and Majorana modes.

The physics of superconductivity is well-studied, and the purpose of this thesis is to give a flavor of the underlying theory before continuing to its role in Majorana physics. To begin, the breakthrough insight in BCS theory was the presence of an attractive potential between electrons mediated by phonon interaction. Once a superconductor is cooled below the critical temperature T_c, phonon-electron interactions results in a net attraction between electrons near the Fermi level. This attraction results in the formation of Cooper pairs which are bound states of two electrons. Unlike the fermions of which they are comprised, Cooper pairs obey Bose-Einstein statistics and can occupy the same quantum state, resulting in a macroscopic superconducting state. Without the phonon-mediated attractive potential, which becomes dominant over the usual Coulomb repulsion between like charges, electrons cannot form this macroscopic state and must obey the Pauli exclusion principle. Below Tc, the formation of this macroscopic ground state ends up being energetically favorable compared to the ordinary Fermi-sea ground state of the normal state.

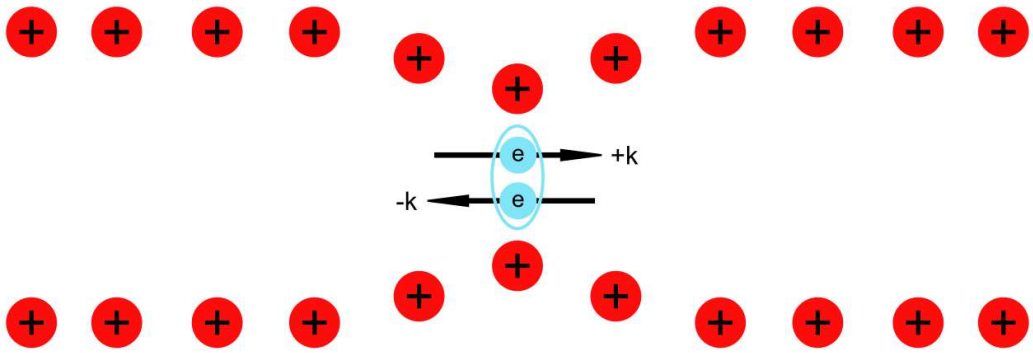

Figure 3.4: Cartoon schematic showing the deformation of the lattice (phonon) as an electron passes. As an electron passes by positive ions in the lattice, the lattice ions move toward the electron. This moves a positive ion closer to a second electron traveling in the opposite direction. This deformation creates an effective positive attraction between two electrons of opposite momentum, resulting in the formation of Cooper pairs.

An intuitive way to think about how the phonon-electron interaction results in this attractive potential between electrons is to imagine two electrons traveling in a lattice of positive ions. As the first electron approaches and then passes any given positive lattice site, the positive ion is perturbed and shifted toward the direction of the first electron's motion. The quantization of lattice vibrations are quasiparticles called phonons. This motion moves the positive lattice site closer to the second electron traveling in the opposite direction, resulting in an effective attraction. If the system is cold enough for phonon-electron interactions to become dominant over thermal excitations in the system, this attractive potential can manifest, overcoming Coulomb repulsion between pairs of opposite momentum electrons, forming Cooper pairs. Cooper pairs are the superconducting charge carrier and exist at the Fermi level, excluding states from a band about the Fermi level, the width of which is determined by the size of the superconducting energy gap Δ. Cooper pairs also have a coherence length, a characteristic length scale over which Cooper pair's wavefunction remains coherent. This length is typically tens or hundreds of nanometers.

A natural language to discuss superconductivity is second quantization. The fermionic operators in superconductivity are the creation operator f (creation of an electron) and the annihilation operator $f^\dagger$ (creation of a hole). For the purposes of this section, we will discuss superconductivity with s-wave pairing. The nomenclature for s-wave pairing comes from atomic orbitals and the shared characteristic is the pairing potential is spherically symmetric with respect to the momentum. A Cooper pair in an s-wave superconductor is created by the term $f_{k\uparrow}^\dagger f_{-k\downarrow}^\dagger$. This term acting on the empty vacuum creates a bound state between a spin-up electron with momentum ħk and a spin-down electron with momentum -ħk. The BCS ground state wavefunction was taken to be

the repeated multiplication of this operator for values of k (with Ψ_0 referring to the vacuum state)

$$|\Psi_{\mathrm{BCS}}\rangle = \prod_{\mathrm{k}}(u_k + v_k f_{k\uparrow}^{\dagger} f_{-k\downarrow}^{\dagger})|\Psi_0\rangle \tag{3.5}$$

$|v_k|^2$ *and* $|u_k|^2$*=1-*$|v_k|^2$ give the probability for occupation and vacancy of the Cooper pair, respectively.

While historically significant, the above form of the BCS wavefunction becomes cumbersome for calculating certain relevant quantities. A more modern framework is a solution by canonical transformation,[31] which gives the model Hamiltonian for the BCS system

$$\mathcal{H}_{model} = \sum_k(\varepsilon_k - E_k + \Delta_k b_k^{\dagger}) + \sum_k E_k(\gamma_{k1}^{\dagger}\gamma_{k1} + \gamma_{k2}^{\dagger}\gamma_{k2}) \tag{3.6}$$

Where $\varepsilon_k = (\hbar^2 k^2/2m) - E_F$ and $b_k = \langle c_{-k\downarrow} c_{k\uparrow}$ [illegible]$_{av}$, the canonical transformation (unimportant for the following discussion). The first sum is a constant equal to the value of the ordinary Fermi-sea ground state energy minus the condensation energy from forming the superconducting condensate of Cooper pairs. In other words, it is the energy of the superconducting ground state. The second sum describes the energy associated with quasiparticle excitations arising in the system. Δ_k represents an energy gap in the quasiparticle density of states. These excitations are known as Bogoliubov quasiparticles. The energy of these excitations γ is given by

$$E_k = \sqrt{\varepsilon_k^2 + |\Delta_k|^2} \tag{3.7}$$

The Bogoliubov quasiparticles are the elementary excitation of superconducting systems. As discussed in the previous section, Majorana modes are excitations also found in superconductors. To look at this relation more closely, we can express the creation and annihilation operators of fermions in terms of Bogoliubov operators, just as we did prior with Majorana operators.

$$\begin{aligned} f_{k\uparrow} &= u_k^{\dagger}\gamma_{k1} + v_k\gamma_{k2}^{\dagger} \\ f_{-k\downarrow} &= -v_k^{\dagger}\gamma_{k1} + u_k\gamma_{k2}^{\dagger} \end{aligned} \tag{3.8}$$

It is important to note either γ operator takes part in both the creation and annihilation of a fermionic mode, just like the Majorana basis discussed earlier. This implies superconductivity is symmetric with respect to electrons and holes. For every +E electron state there exists a -E hole-like state. With the clever choice $u=v^*$ and removal of spin degeneracy, the Bogoliubov operators satisfy the conditions necessary to create Majorana modes in a superconducting system![25] Majorana operators are then just a spinless basis of Bogoliubov operators with $u=v^*$.

Three important relations are included below for completeness, applicable in the case of weak attraction and k independence. The BCS electronic density of states of a superconducting system well-below T_c and in zero magnetic field is given by

$$\frac{N_{BCS}(E)}{N_0} = \begin{cases} \frac{E}{\sqrt{E^2-\Delta_\infty^2}}, E > \Delta_\infty \\ 0 \quad\quad , E < \Delta_\infty \end{cases} \tag{3.9}$$

where N_0 refers to the normal-state density of states and Δ_∞ refers to the constant bulk energy gap. The total number of states is equal between the normal and superconducting

states, with the excess removed from the superconducting energy gap forming the coherence peaks just outside of the gap. The coherence length of Cooper pairs, important for the superconducting proximity effect, is given by

$$\xi_{BCS} = \frac{\hbar v_F}{\pi \Delta_\infty} \tag{3.10}$$

Lastly, the relationship between the zero-temperature superconducting energy gap and temperature is given by

$$\Delta_\infty = 1.76 k_B T_c \tag{3.11}$$

Superconductivity provides two important pieces toward the creation of Majorana modes. First, superconductors have the required particle-hole symmetry, as expressed with Bogoliubov operators, to create Majorana modes. Second, the formation of Cooper pairs in an energy band about the Fermi level, with the included particle-hole protection, provides protection for the Majorana zero modes from energy states outside of the gap.

3.3 QD-MZM Measurement

Providing experimental evidence, so called smoking gun signatures of MZMs is the main focus of experimentalists. A variety of experiments have been proposed and tested, but to date, no smoking-gun signature of MZMs have been measured, though a mounting body of evidence points to their existence. Quantized Majorana conductance was once the leading candidate for a smoking gun signature, but ultimately faces significant experimental challenges.[15,16] This experiment, and its current difficulties, is described in Appendix C.

The most notable experiment not discussed in this thesis is the 4π Josephson effect.[10] The ultimate smoking gun signature of MZMs will be the recording of non-Abelian braiding statistics in an interferometry setup, but this in and of itself requires two well localized and controllable MZMs.[8] Only recently have Abelian anyons been braided after decades of effort, pointing to the difficulty of this type of measurement.[32] One of the leading candidate measurements to provide the most robust signature of the MZMs outside of braiding are QD-MZM measurements.[5,17,33,34,35,36] The promise of QD-MZMs spurred the development of the SCQDM.

The SCQDM was developed to provide a scanning quantum dot microscope capable of measuring MZMs in Majorana platforms that lend themselves to study via scanning probe. As a byproduct of the relative success and accessibility of quantum dots in the Majorana nanowire platform, the proposals for studying MZMs using QDs are calculated in the context of the Majorana nanowire platform. Fortunately, the conclusions are independent of the experimental setup. Presented here is a qualitative explanation of a particular QD-MZM measurement proposed in part by Professor Alex Levchenko.[5]

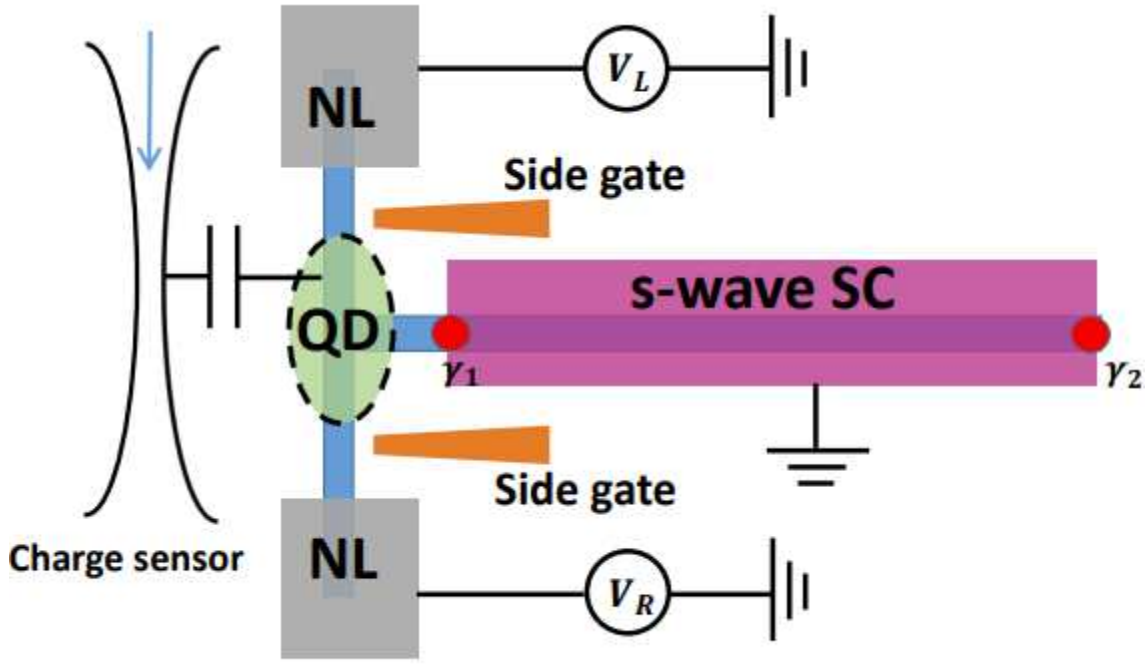

Figure 3.5: Cartoon schematic showing the experimental setup. The nanowire is a semiconductor proximitized by a nearby s-wave superconductor. NL stands for normal leads, of which there are two (left and right in the theory) connected to the QD. Application of a longitudinal magnetic field can induce the topological phase transition to the state supporting MZMs. The MZMs are indicated by red circles. A charge sensor is used to record the conductance through the quantum dot. Reprinted figure with permission from Lui, Levchenko, and Lutchyn. Physical Review B, 92, 205422(2015). Copyright (2015) by the American Physical Society. Abstract can be viewed at https://journals.aps.org/prb/abstract/10.1103/PhysRevB. 92.205422. [5]

The Majorana nanowire platform consists of a strong spin-orbit coupling semiconducting nanowire proximitized by a superconductor in an applied magnetic field. The QD used for the study is defined as part of the semiconducting nanowire via underlying gates. The exact setup for the theory uses two leads coupled to the quantum dot, which is controllably coupled to both MZMs at the ends of the nanowire. A charge sensor is employed, which in principle could be the charge sensing circuit employed in the SCQDM.

The Hamiltonian for this system in the presence of an external magnetic field is

$$H = H_{Leads} + H_{QD-MZM} + H_T \; where \begin{cases} H_{Lead} = -iv_F \sum_{\alpha=L,R} \int dx \psi_\alpha^\dagger(x) \partial_x \psi_\alpha(x) \\ H_{QD-MZM} = \epsilon_d d^\dagger d + i\kappa(d + d^\dagger)\gamma_1 + i\delta\gamma_1\gamma_2 \\ H_T = \sum_{\alpha=L,R}(t_\alpha \psi_\alpha^\dagger(0) d + t_\alpha^* d^\dagger \psi_\alpha(0) \end{cases} \quad (3.12)$$

The summations in H_{Lead} and H_T are done over both the left (L) and right (R) leads. The creation operator for an electron in the leads (QD) is given by $\psi_\alpha^\dagger$ ($d^\dagger$), with the α subscript denoting which lead. v_F refers to the Fermi velocity, the two MZMs are labeled γ_1 and γ_2, and ϵ_d is the energy level in the QD. κ (t_α) refers to the coupling strength between the nearest MZM (leads) and the QD. An additional coupling, δ, gives the amount of overlap between the two separated MZMs, a measurement of the localization of these modes. This Hamiltonian is spinless, but introducing spin only introduces small corrections to the result.

This Hamiltonian is generalizable across QD-MZM theory proposals, but in specific the SCQDM was spurred on [5]. The approach is to calculate the cumulants of the conductance through the quantum dot, the cumulants being the higher order statistics of the conductance signal. The first four cumulants are the mean, variance, skewness, and kurtosis, respectively. Using the above Hamiltonian, a cumulant generating function was calculated and the conductance was computed using a Keldysh path integral approach. Figure 3.6 is reproduced from the paper showing the first four cumulants as a function of the various coupling strengths under realistic experimental settings.

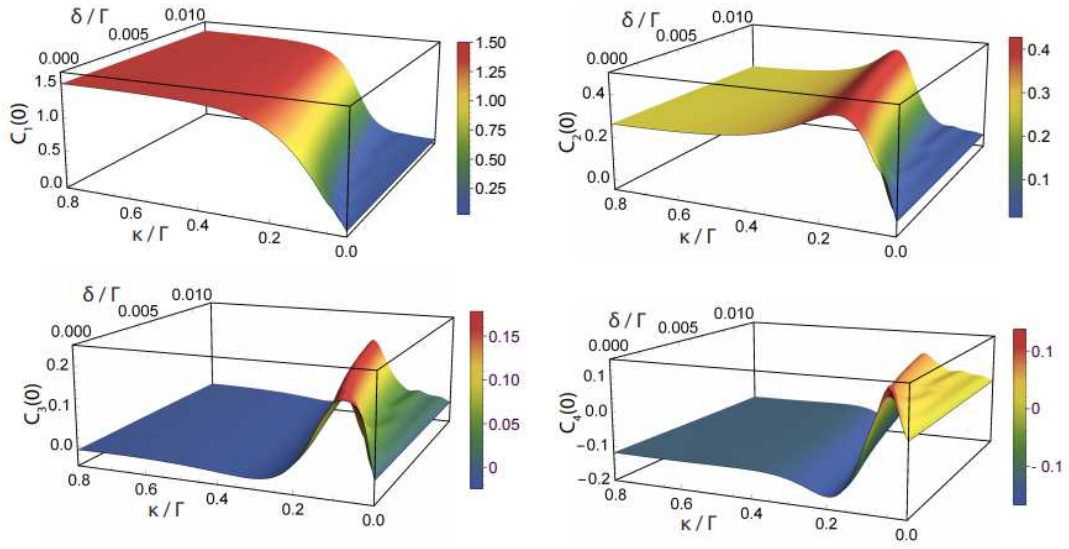

Figure 3.6: The cumulants of the conductance measured through the quantum dot $C_n(0)$ for n=1,2,3,4 as a function of κ, the QD-MZM coupling strength and δ, a measure of the amount of overlap between the two MZMs at either ends of the nanowire. Here $\epsilon_d/\Gamma = -10.0$, $\Gamma_L = \Gamma_R$, $eV/\Gamma = 0.001$ and Λ/Γ=30.0, which are chosen to be realizable experimentally. Reprinted figure with permission from Lui, Levchenko, and Lutchyn. Physical Review B, 92, 205422(2015). Copyright (2015) by the American Physical Society. Abstract can be viewed at https://journals.aps.org/prb/abstract/10.1103/PhysRevB.92.205422.[5]

Following the color scale, the cumulants undergo a clear change in value as a function of κ, the coupling strength between the QD-MZM and Γ, the lead coupling strength. Focusing on the first cumulant, the mean value of conductance, it is clear at $\kappa/\Gamma = 0$ the total conductance is zero but rises to a value of 1.5 as $\kappa/\Gamma \to 0.8$. The other three cumulants follow similar trends as the QD-MZM coupling strength increases. The values of these cumulants are unique to coupling the QD to the MZMs.

Chapter 4

Theory: Strong-Coupling Quantum Dot Microscope

The Strong-Coupling Quantum Dot Microscope was developed over the course of this thesis to study Majorana zero modes in topological superconducting systems. The SCQDM was developed using contributions from two fields: scanning probe microscopy and single charge transfer. At a basic level, the SCQDM is a single electron counter on a scanning probe, capable of accessing the counting statistics of electrons entering the apex quantum dot and angstrom distance tunneling into the surface of a sample. The following sections will develop the theory behind the quantum dots, single electron boxes, the basis of the charge sensing circuit and the operation of the microscope.

4.1 Quantum Dots

A quantum dot is a mesoscopic island of metal or semiconductor with quantized electronic energy levels. Often called artificial atoms, quantum dots are a peculiar mesoscopic system capable of displaying quantization effects apparent up to micron-sized islands.[37] The overall range of sizes and materials for quantum dots starts with single metallic grains and molecules of semiconductors up to semiconducting nanowires and large metallic islands. Quantum dots in condensed matter physics have served as both samples of interest and sensitive detection methods. The power of quantum dots as detectors comes from the ability to tunnel single electrons onto the quantum dot (or for photonic application, the

emittance or capture of photons). The ability to control single electron tunneling, while coupling the quantum dot to dynamical systems allows the quantum dot to illuminate aspects of the coupled system.

Following a semiclassical approach we can consider two relevant energy scales for single electron tunneling into quantum dots: single-particle quantum energy levels and Coulomb charging energy.[38] Quantum energy levels refer to the single-particle energy states available for occupation by electrons, typically modeled as energy levels in a harmonic oscillator potential. The energy spacing for quantum energy levels is given by $E_k = 1/g(\varepsilon_F)V$ where V is the island volume and $g(\varepsilon_F)$ is the density of states on the Fermi surface. Metallic grains and semiconducting systems generally operate in this regime, where the spacing between individual quantum levels is larger than the charging energy $E_k \gg E_C$.

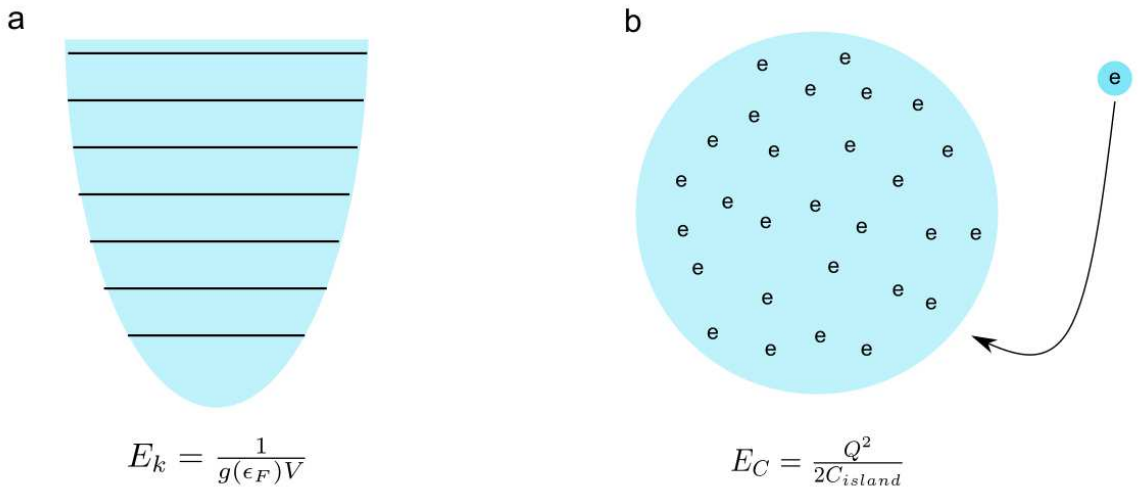

Figure 4.1: Addition energy regimes. (a) In small metallic and semiconducting quantum dots, the dominate energy scale is the quantum level spacing between available energy eigenstates. (b) For large metallic quantum dots, the dominate energy scale is the Coulomb energy, the energy to bring a charge from infinity to the quantum dot overcoming repulsion.

The Coulomb charging energy, given by $E_c = \frac{q^2}{2C}$ where C is the island's capacitance, refers to the classic electrostatic problem involving the energy cost to bring an electron from infinity to a group of clustered charges. Large semiconducting systems and most metallic systems operate in the regime in which the quantum energy level spacing is much smaller than the charging energy $E_C \gg E_k$. One quantity, the addition energy E_a, provides a generalization across quantum dot architectures, $E_a = E_c + E_k$. The mesoscopic size of the quantum dots used in SCQDM (200-400 nm) equates to approximately a million electrons occupying the dot at any one time, resulting in small energy level spacings. For this thesis, addition energy and Coulomb charging energy are synonymous, as the SCQDM operates in the large metallic quantum dot regime $E_C \gg E_k$.

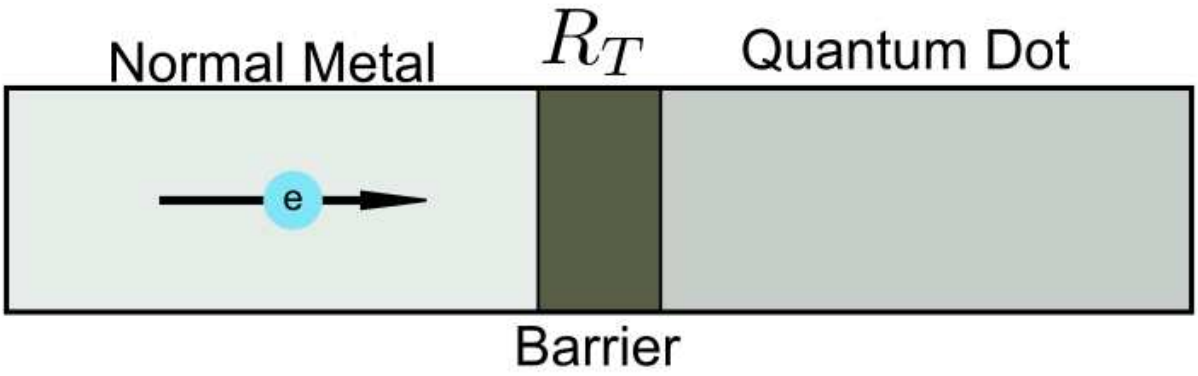

Figure 4.2: Cartoon schematic of single electron tunneling. The barrier and island are key components for observing single-electron tunneling. Additionally, $R_J >> R_K$ and $E_a >> k_BT$. The simple schematic shown is presumably connected to the appropriate voltage source to generate a tunneling current. A specific realization of single-electron tunneling is introduced in the next section.

There are two general requirements for observing single-electron tunneling. Systems that satisfy both requirements are said to be operating in the Coulomb blockade regime.[38] The first requirement results from demanding the tunneling electron's

wavefunction must be localized to the quantum dot after the tunneling event. In other words, the charge on the quantum dot must be quantized and remain on the quantum dot for arbitrary time. This requirement is in part satisfied by the quantum dot. To fully satisfy this requirement, the quantum dot must be connected to one or more electrical leads via tunnel junctions with junction resistance R_J much greater than the resistance quantum R_K defined below

$$R_K = \frac{h}{e^2} \approx 25.8k\Omega \text{ with } R_T \gg R_K \tag{4.1}$$

The phenomenological value of the resistance quantum R_K comes from general consideration of the energy-time uncertainty relation in the context of a voltage applied between two sides of a tunnel junction. Once an electron has tunneled onto the quantum dot, the lifetime of the excess electron on the quantum dot is governed by the effective RC time constant of the tunnel junction, $\tau = R_J C_J$. The corresponding energy uncertainty relation must be smaller than the relevant energy scale, namely the Coulomb energy E_C. Simply put, for single charge tunneling to be observed, the energy required to add the electron to the quantum dot must be greater than the uncertainty in that energy, and the uncertainty is driven by the RC time constant. This is readily achieved in experiments.

The second requirement for single-electron tunneling is the thermal energy $k_b T$ in the system must be much smaller than the addition energy for single-electron tunneling. This requirement is simple. If the thermal energy of the electron is greater than the energy required to tunnel an excess electron onto the quantum dot, thermal fluctuations of the quantum dot's charge will dominate, obscuring any single electron tunneling signal. In

realistic experimental settings, the addition energy needs to be roughly an order of magnitude larger than the thermal energy $E_a \geq 10k_BT$.[37]

4.2 Single Electron Box

The simplest circuit enabling the measurement of single electron tunneling events is the single electron box (SEB), upon which the SCQDM is based.[37] The SEB architecture consists of a single metallic island connected to a simple circuit via one tunnel junction and one capacitance junction. The tunnel junction allows single electron tunneling into and out of the quantum dot, with charge sensing provided by an external charge sensor or integrated into the capacitance lead, as is the case with the SCQDM. The charge sensing circuit is described in Section 4.3.

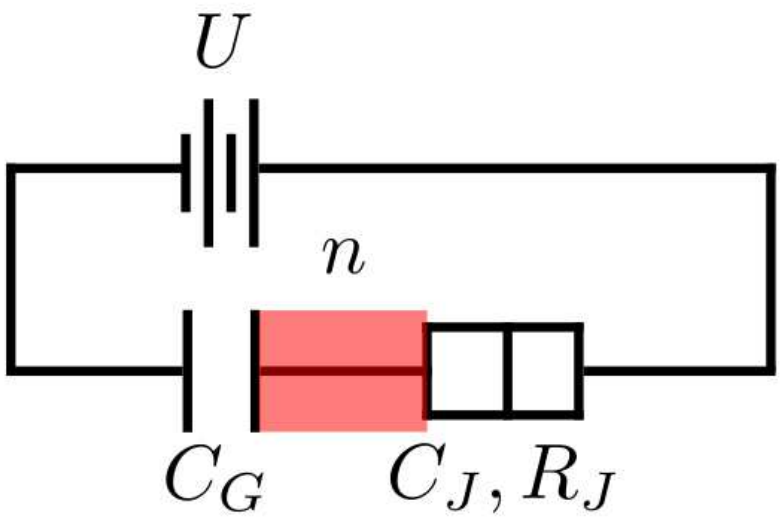

Figure 4.3: Circuit diagram of the single electron box. The quantum dot is highlighted in red. The tunnel junction (right of the red QD) populates the QD, whereas the capacitance junction (left of the red QD) enables a voltage V to be applied across the quantum dot. This is the simplest circuit capable of resolving single electron tunneling events.

The total capacitance of the island is the sum of the gate capacitance and junction capacitance $C_\Sigma = C_G + C_J$. The SEB is dominated by the Coulomb charging energy $E_C = \frac{e^2}{2C_\Sigma}$, resulting in the total electrostatic energy of circuit being

$$E = E_C(n - n_g)^2 \tag{4.2}$$

where n refers to the instantaneous charge added to the quantum dot and n_g refers to the polarization charge added via the gate capacitor $n_g = C_G U/e$. Consecutive single-electron tunneling events can be observed by sweeping the bias voltage U across the quantum dot. Figure 4.4 shows how this scheme manifests using the charge detection circuit employed in the SCQDM (further discussed in Section 4.3). As the sweep approaches the electron addition energy, a single electron will tunnel onto the quantum dot and be sensed by the charge sensing circuit. The spacing of the charge events is expected to be periodic and equal to the electron addition energy.

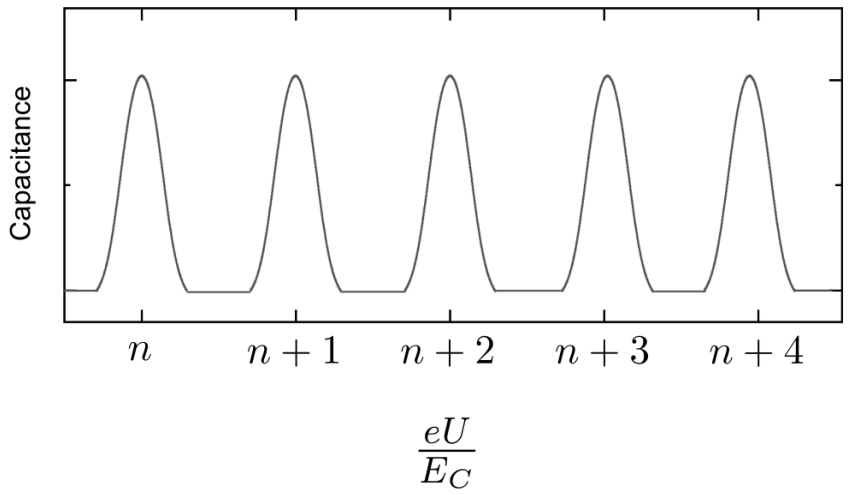

Figure 4.4: Capacitance peaks indicating single electron tunneling as a function of applied sweep voltage eU. Periodic peak spacing is expected for well-resolved QDs and low noise experiments.

The charge sensing scheme employed relates measured charge with capacitance via the relation

$$C_m = \frac{dq}{dV} \cong \frac{\Delta q}{\Delta V} \tag{4.3}$$

At finite temperature, the average charge on the quantum dot is not quantized, but the instantaneous charge change is quantized, which is ultimately what the SCQDM is sensitive to. A Boltzmann weighted average of charge states gives the average charge on the island.[38]

$$\langle n \rangle = \frac{\sum_{n=-\infty}^{\infty} n * \exp(-\frac{E_n}{k_b T})}{\sum_{n=-\infty}^{\infty} \exp(-\frac{E_n}{k_b T})} \tag{4.4}$$

Fortunately, the temperature the SCQDM operates at (300 mK) is typically much smaller than $k_B T$.

4.3 SCQDM Operation

The Strong-Coupling Quantum Dot Microscope is a novel scanning quantum dot microscope which utilizes a sharp glass probe with two aluminum leads deposited along the length of the probe and an apex aluminum quantum dot. In essence, the SCQDM is a single electron box fabricated on the end of a scanning probe, which uses a charge sensing circuit based off single electron capacitance spectroscopy (SECS)[4] and subsurface charge accumulation imaging (SCAI).[3] The SCQDM has two core functionalities: single electron tunneling into the apex quantum dot and angstrom distance tunneling. The latter

technique uses standard STM procedures, described earlier in Chapter 2. A general description of the SCQDM and the charge sensing circuit are the focus of this section.

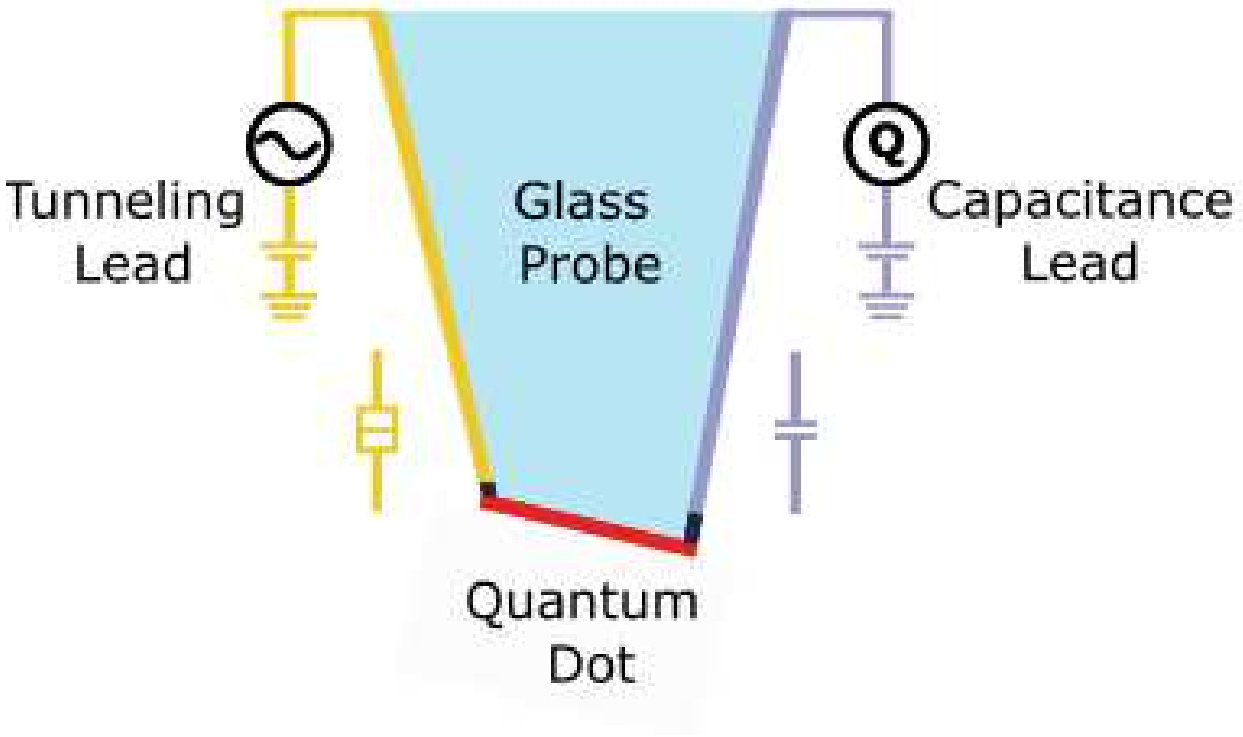

Figure 4.5: Reproduction of Figure 1.1. The tunnel lead (gold), capacitance lead (purple), and quantum dot (red) comprise the functional SEB. The charge sensing circuit is connected to the capacitance lead.

Figure 4.5 shows a schematic of the SCQDM. The tunneling lead (gold) is responsible for populating the apex quantum dot (red). The capacitance lead (purple) is connected to a sophisticated charge sensing circuit which is capable of measuring attofarad (10^{-18} F) capacitance changes due to single electron tunneling events.[39] Separating the quantum dot from each lead are junctions (black), which are asymmetric with respect to each other. The tunnel junction allows single electron tunneling from the lead to the quantum dot, whereas the capacitance junction is fabricated to prevent this charge

transfer. In this way, the capacitance lead instead forms an image charge in response to single electron tunneling into the quantum dot, which can be detected using the charge sensing circuit.

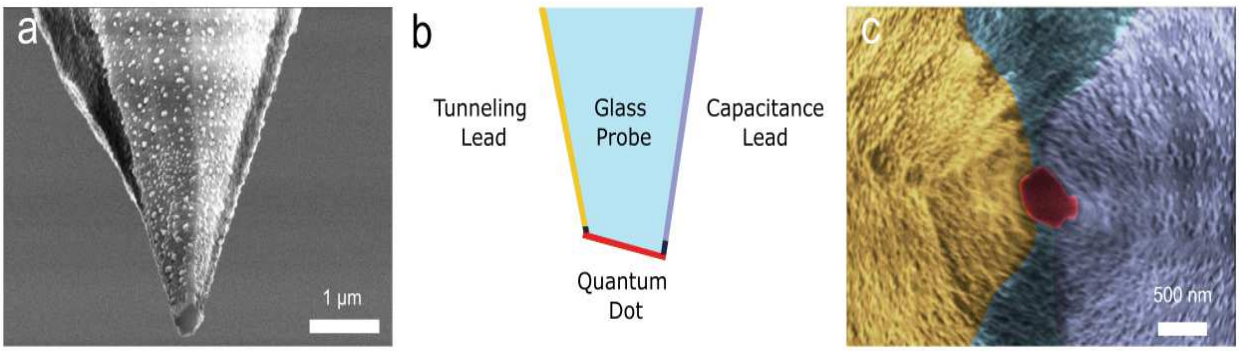

Figure 4.6: SEM images of a functional SCQDM probe. (a) 52 degree angle view of the tip apex, showing the QD (bottom of the image) and tunnel lead (light grey). (c) A false color image of the same SCQDM tip apex, with color guide provided by (b), shows two well-formed and separated leads, as well as a roughly circular apex quantum dot on the order of 400 nm in diameter.

Figure 4.6 shows two scanning electron microscope (SEM) images of a functional SCQDM probe. Figure 4.6a shows the probe from a 52-degree angle relative to vertical, showing both the tunneling lead and apex quantum dot. Figure 4.6c, with color guide provided in the Figure 4.6b, is the same probe from end-on, showing both junctions, clear lead separation, and the apex quantum dot which is approximately 400 nm in diameter.

Operation of the SCQDM for single electron counting is as follows. A DC voltage is maintained between the tunnel and capacitance lead, $V = V_{tunnel} - V_{cap.}$, with a superposed AC voltage at approximately 23 kHz. By sweeping V_{tunnel} relative to $V_{cap.}$, numerous single electron tunneling events can be recorded, with the energy (voltage)

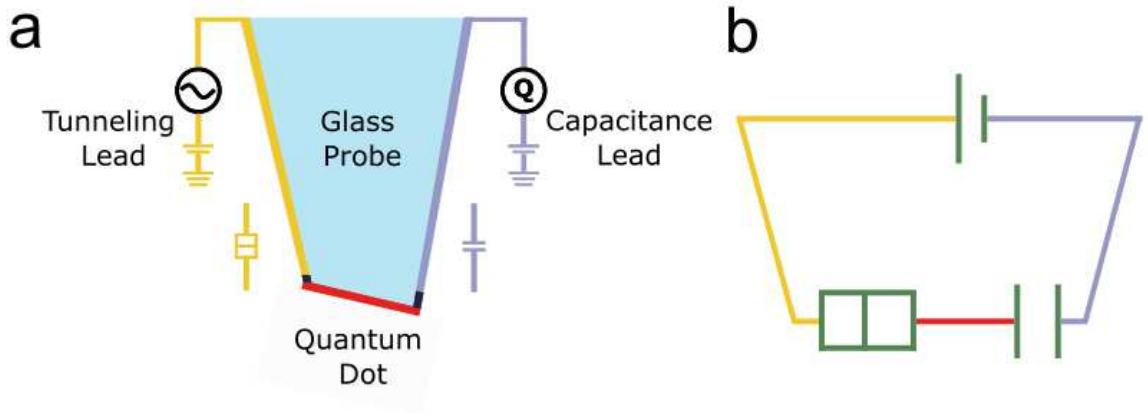

Figure 4.7: Reproduction of Figure 1.1 (a) alongside a color coded SEB schematic (b). The functional part of the SCQDM comprises a SEB architecture, with the junctions provided by aluminum oxide.

spacing determined by the addition energy of the quantum dot (typically on the order of meV or less). As the DC level approaches a single electron addition level, the superposed AC excitation voltage causes the electron to rapidly tunnel on and off the quantum dot from the tunneling lead, inducing an oscillating image charge in the capacitance lead. This oscillating image charge is then detected by the charge sensing circuit to be described. In this manner a large enough DC voltage sweep can capture multiple single-electron tunneling events (see Figure 4.4 and Figure 6.4).

The charge sensing circuit is based off single electron capacitance spectroscopy, a device technique,[4] and subsurface charge accumulation imaging, which first implemented SECS into a scanning probe setup.[5] The technique can resolve fractions of an electron charge, with a noise level of $0.03e/\sqrt{Hz}$ at 300 mK. While the charge sensing circuit ultimately provides a measurement of charge transfer, a more appropriate language to describe its operation is in terms of the capacitance change due to a single electron

tunneling event. The charge sensing circuit measures the change in capacitance between the tunnel and capacitance leads due to single-electron tunneling events into the quantum dot. The capacitance measured C_m is extracted from the oscillating image charge measured and the applied AC excitation voltage

$$C_m = \frac{dq}{dV} \cong \frac{\Delta q}{\Delta V} \tag{4.3}$$

where Δq is the oscillating image charge in the capacitance lead detected by the lock-in amplifier and ΔV is the AC excitation voltage.

The extremely sensitive charge detection is enabled by the High Electron Mobility Transistor (HEMT). A HEMT is a field-effect transistor which uses two materials with dissimilar band gaps to achieve band bending at the interface, creating a highly mobile 2D electron layer. The current through the source-drain channel of the HEMT is highly sensitive to the voltage applied to the gate of the HEMT, which in the SCQDM circuit is connected to the capacitance lead. When an electron tunnels onto the quantum dot, the induced image charge in the capacitance lead shifts the voltage applied to the gate, modulating the source drain current. When measuring the source-drain signal using a lock-in amplifier, which preferentially selects only the frequency the circuit is being driven at, the capacitance change can be measured.

Ambient capacitance signal inside the scan head is much larger than the change in capacitance due to populating the quantum dot. To resolve attofarad capacitance shifts, the overall background capacitance signal needs to be subtracted away. This is achieved through a balancing channel, which in practice is a gold pad defined next to the tip apex. By

applying a 180 degree out of phase AC signal at the driving frequency, the background capacitance signal can be eliminated.

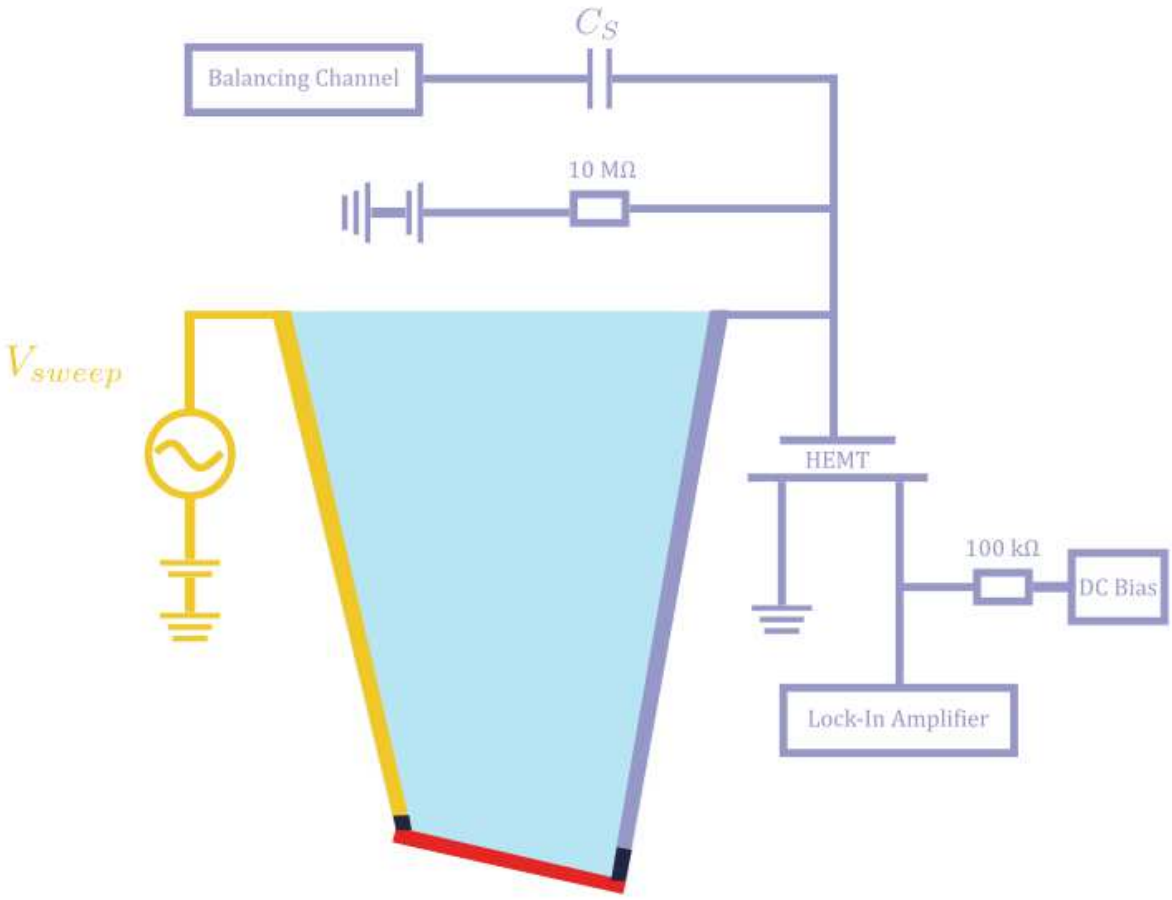

Figure 4.8: Complete circuit diagram of the SCQDM. The AC/DC sweep is provided by a pulse generator attached to the tunnel lead. An induced image charge in the capacitance lead due to a single-electron tunneling events modulates the voltage applied to the gate of the HEMT, which changes the source-drain signal of the HEMT. This change is further detected by a lock-in amplifier, which locks onto the AC frequency the measurement is driven by. An additional balancing capacitor subtracts away the ambient capacitance present in the experiment, allowing the minute capacitance changes to be measured.

Relating the voltage measured by the lock-in amplifier and the capacitance measured requires understanding the capacitances in the system. The capacitance between the tunnel and capacitance leads is in series with the input capacitance of the

HEMT. The large input capacitance of the HEMT (0.4 pF) and relatively small capacitance change due to single electron tunneling into the quantum dot (aF) allows a simplification of this voltage divider. Accounting for the gain of the HEMT G (order unity) and incorporating the AC excitation gives the following equation relating the measured voltage V_m and C_m,

$$V_m = GV_{exc}\frac{C_m}{0.4pF} \tag{4.5}$$

The measured charge Q_m can be readily extracted using C_m

$$Q_m = V_{exc}C_m \tag{4.6}$$

Further, there exists a lever arm parameter in the system. This describes the geometry-dependent ratio of the potential difference between the tunneling lead and quantum dot, divided by the potential difference applied between the tunneling lead and capacitance lead. On a practical level, the lever arm parameter scales the applied voltage to the voltage sensed by the quantum dot. The typical value of the lever arm parameter for the SCQDM is approximately 10. The lever arm parameter α can be extracted using the following equation

$$\frac{1}{\alpha} = \frac{Q_m}{e} \tag{4.7}$$

The inverse lever arm parameter multiplied by the charge of an electron gives the fraction of charge detected by the charge sensing circuit.

A single electron peak fitting model, originally developed and tested with single electron capacitance spectroscopy[4], provides further verification of the presence of single electron tunneling events and is employed in Chapter 6. The model convolutes a half-

ellipse, whose width is set by the experimental value of the excitation voltage, with the derivative of the Fermi function, which incorporates any thermal broadening due to the finite temperature of the experiment (usually approximately 300 mK). An RC integration effect is included, which accounts for the effect of the lock-in amplifier's time constant. This latter effect is pronounced in many techniques using the same charge sensing scheme but is very small and can be ignored in the context of SCQDM. Two free parameters are permitted by the model. First, the baseline of the capacitance signal (sometimes called the zero-level) is free to be defined. The expected capacitance signal is periodic peaks separated by a flat baseline, as seen in Figure 4.4. Second, the lever arm parameter, the geometry-dependent ratio of the potential difference between the tunneling lead and the quantum dot, and the capacitance lead and quantum dot, is a fitting parameter. The lever arm parameter can be found in Equation 4.7. Fitting of single electron peaks with this experimental model provides verification of single-electron tunneling events.

Chapter 5

Fabrication: Strong-Coupling Quantum Dot Microscope

The fabrication of the Strong-Coupling Quantum Dot Microscope has been developed and refined over the course of this thesis work. The following section will provide a roadmap for fabrication of this probe, which comprises the functional part of the SCQDM. Understanding of the fabrication process is necessary for creating the SCQDM and was a large focus of this thesis, but not integral for understanding experiments described in Chapter 6. Further alternatives and considerations for the fabrication process are presented in Appendix A, an important companion text to this chapter for future researchers using the SCQDM.

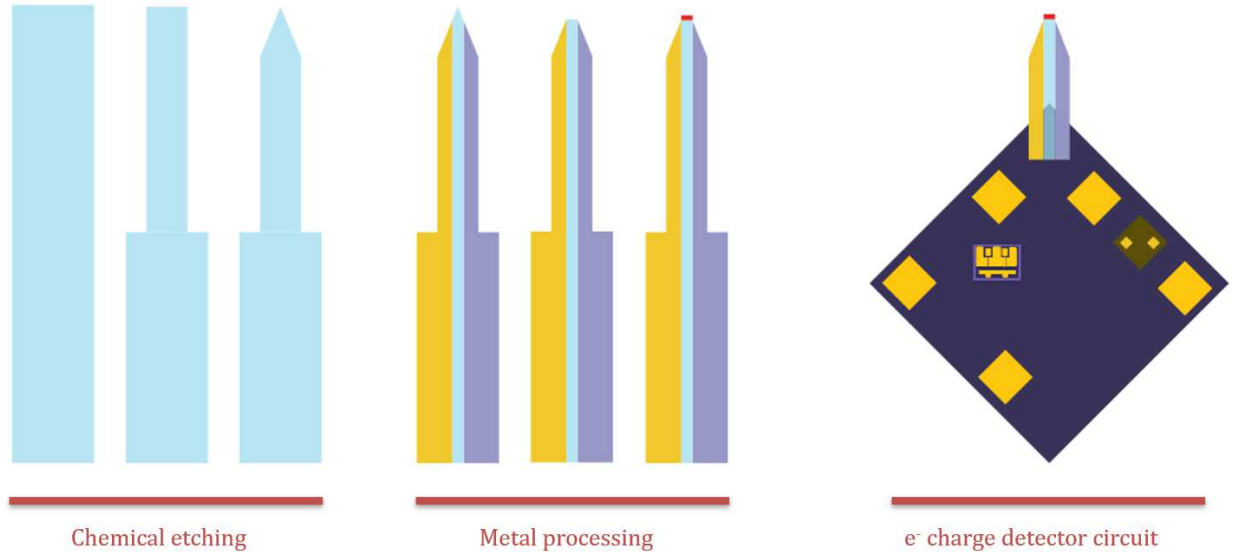

Figure 5.1: Visual roadmap for fabrication of the Strong-Coupling Quantum Dot Microscope.

5.1 Overview

The fabrication of the SCQDM can be summarized into three stages: chemical etching, metal processing, and charge sensing circuit. The first chemical etching stage shapes glass optical fibers into the appropriate shape. The probe must have a small enough apex to create a quantum dot with resolvable electronic levels, as well as reliably tunnel into the surface of the sample. This small shape and roughly circular apex are achieved via etching in hydrofluoric acid and oleic acid.[40] With a pencil shaped probe, the metal processing step defines two aluminum leads, separated from an apex quantum dot by aluminum oxide junctions. An asymmetry is introduced in this step to define one lead as the tunnel junction, used to populate the apex quantum dot, and one as the capacitance lead, used to sense the charge tunneling event. Further, this asymmetry protects the sensitive tunnel junction from surface interactions when the probe is tunneling into the sample surface. The final metal processing step is the deposition of an apex quantum dot, completing the functional probe of the SCQDM. The last step in the fabrication process is mounting the probe onto a charge sensing circuit. Utilizing a High Electron Mobility Transistor, on chip resistor, and a number of wire bonds and epoxy, the circuit allows for connecting the probe to room temperature electronics and provides the charge sensing capability for electrons entering the quantum dot.

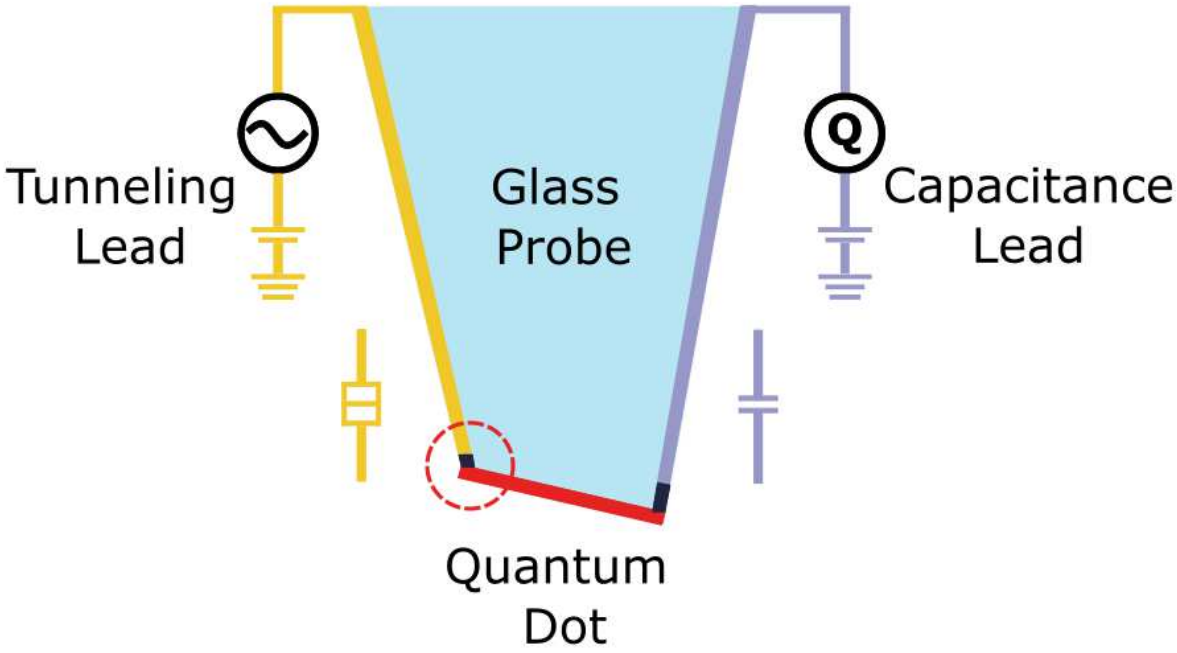

Figure 5.2: The Strong-Coupling Quantum Dot Microscope. The black portions depict the lead's respective junctions. Circled in red is the sensitive tunnel junction, which is tilted away from the tip apex, protecting this junction from surface interactions and preserving the single electron counting capability.

5.2 Chemical Etching

The basis of the functional probe is a silica optical fiber. The insulating properties of the silica and its cylindrical shape allow separate leads, as well as an apex quantum dot, to be defined on the probe with standard thermal evaporation techniques. The first step in creating the probe requires shaping the optical fiber into the optimal geometry, namely a roughly pencil shape with a tip apex on the order of 100-300 nanometers in radius. The related technique, Scanning Single Electron Transistor Microscopy, utilizes a carbon laser pulling method to achieve this tapered end.[2] The high cost of this method required an alternative and the area of Near-Field Scanning Optical Microscopy (NSOM) provided a low-cost, high-throughput method for shaping the optical fibers via chemical etching.[40,41]

The chemical etching process involves etching the optical fibers using hydrofluoric acid and an immiscible overlayer of organic acid. Development of this process, and experimentation with different organic acid overlayers has led to the identification of a group of organic acids that provide a spectrum of etch times and etch angles.[41] Oleic acid is the organic acid chosen for SCQDM.[40] The motivating factor for this choice is the relatively steep etching angle (~75 degrees), an important consideration for oxidizing unwanted aluminum deposited on the leads during the apex quantum dot evaporation step described later.

The optical fiber of choice, the SM-300 by Thorlabs, consists of two parts from the point of view of the SCQDM. The first part is the jacket, a 250um protective coating surrounding the fluorine depressed silica cladding. Within the cladding exists a pure silica

core, but for the purposes of the SCQDM the core/cladding are indistinguishable. The first step in processing is cutting the optical fibers into 2-5cm lengths. 3-8 mm of the protective jacket is then removed from one end of the tip, exposing the 125um core/cladding. These tips are then cleaned of any jacket residue and placed into a custom-made Teflon tip holder. The holder, which contains as many as 30 tips per batch, is then mounted onto a micro-positioner which is attached to a ring stand and placed in a fume hood. The rest of this procedure takes place within the fume hood, while wearing the proper personal protective equipment.

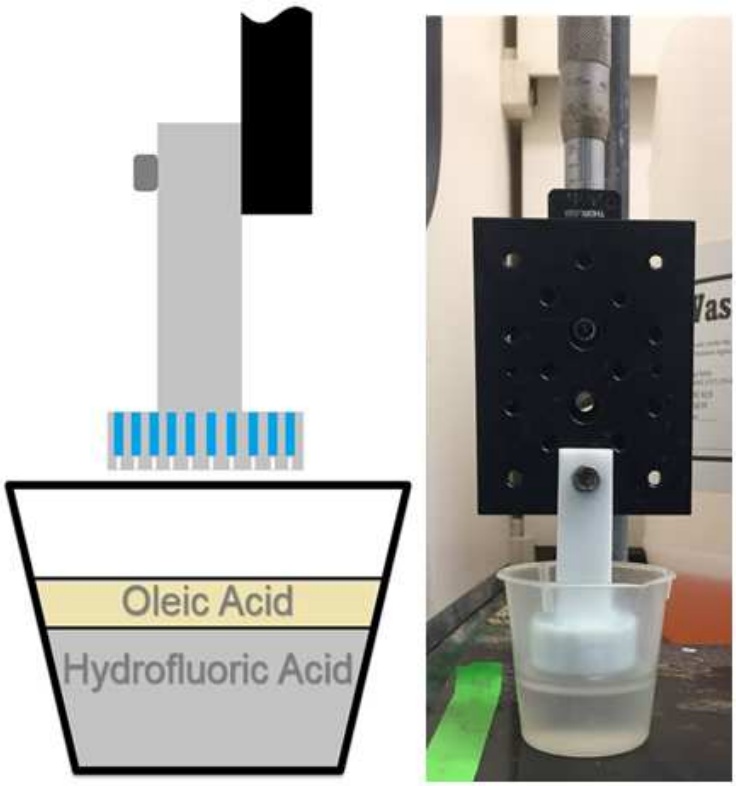

Figure 5.3: Chemical etching process. Left: Cartoon schematic of etching setup, with optical fibers in blue/white. The Teflon holder is shown in grey, with the micropositioner in black. Right: Image of chemical etching process inside a fume hood.

40 mL of 60% Hydrofluoric acid is dispensed into a Teflon beaker, followed by an immiscible layer of oleic acid on top. The only requirement for the oleic acid layer is to totally cover the hydrofluoric acid and is typically dispensed using a long pipet. The beaker with the etching acids is placed beneath the Teflon tip holder. The holder is then lowered using the micro-positioner until the bottom of the Teflon tip holder is flush with the top of the oleic acid. This is often marked by a contrast change in the color of the oleic acid layer.

The minimal/optimal etching time is 38 minutes 30 seconds, with successful batches of tips also etched for up to one minute longer. Once the etch time is complete, the holder is lifted from the beaker. The now etched tips are cleaned using acetone, followed by isopropyl alcohol, followed by deionized water to remove any contaminants on the glass probes. The next step is using an optical microscope at 100x to determine which tips were properly etched. The etching procedure typically results in 80% yield of viable, resulting in roughly 24 viable tips per etch. Viable tips are those which have sub-micron apex diameters as determined by the optical microscope.

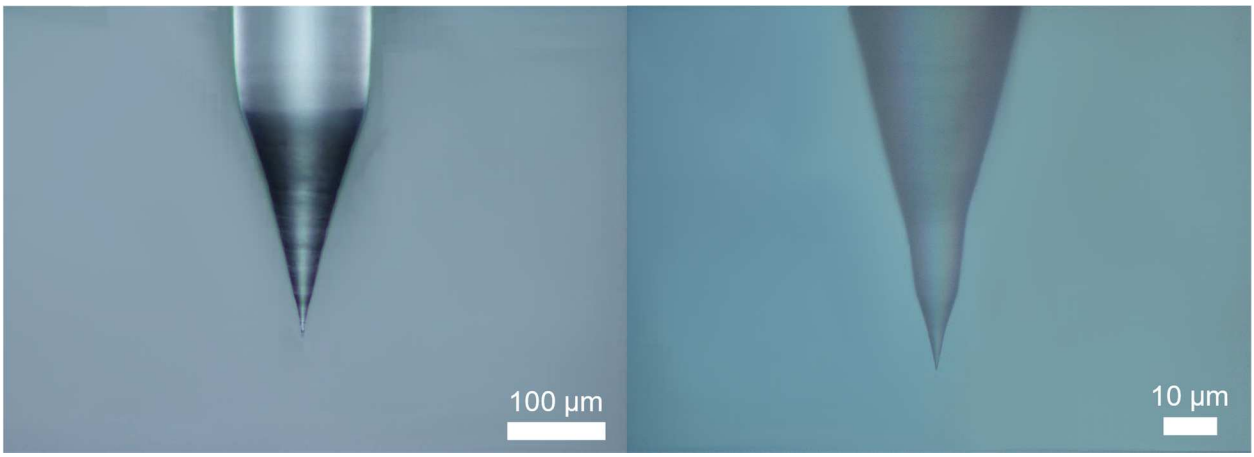

Figure 5.4: Optical images of SCQDM probes after chemical etching. Left: Wide view of the etched portion, showing the clear taper toward the apex. Right: Zoomed-in view of the another probe's apex.

The viable tips are then loaded into custom-made aluminum tip holders, 6 each, for metallic processing. The tips and aluminum holders are then baked at 120 C for ten minutes, to ensure no water vapor is trapped on the surface of the probe or inside the holder.

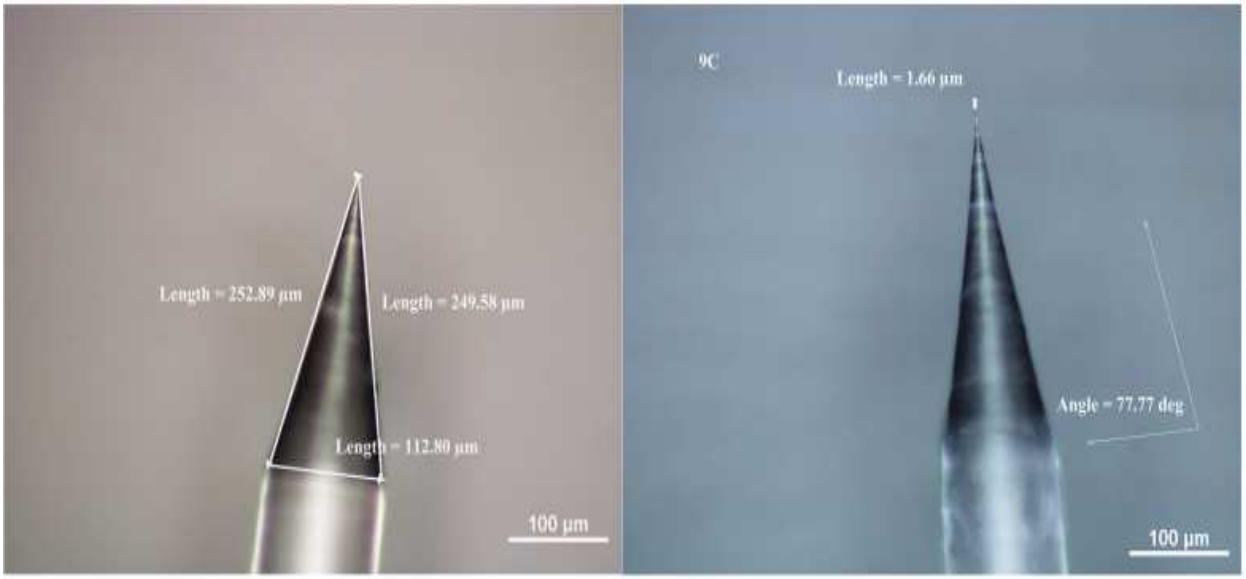

Figure 5.5: Various labeled lengths from a typical etch. Left: Measurements of the tip's slope show a highly symmetric probe. Right: Measurement of the slope angle. The steep angle is key for not shorting the leads during the thermal evaporation step.

5.3 Thermal Evaporation

Batches of 24 etched optical fibers are processed using standard thermal evaporation technique. Three separate evaporations are done to define the tunneling lead, capacitance lead, and quantum dot. Four aluminum tip holders are mounted onto the thermal evaporation plate and loaded into the Edwards Auto 305 thermal evaporator in the Keck Microfabrication Facility.

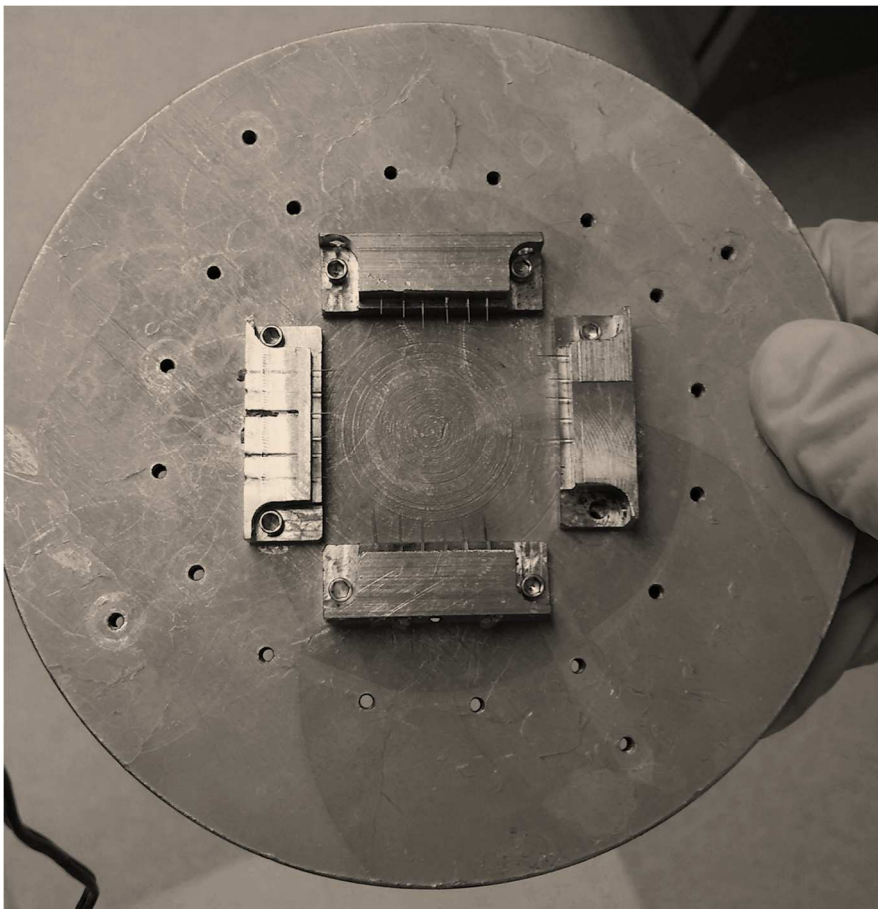

Figure 5.6 Four SCQDM tip holders mounted onto the thermal evaporation plate post thermal evaporation. Each contains 5-6 SCQDM probes ready for metallization.

Using a liquid Nitrogen cold trap and turbomolecular pump, the base pressure inside the deposition chamber is reduced to 10^{-7} Torr over the course of one hour of pumping. To clean the source aluminum, 10 nm of Al are evaporated prior to opening the shutter and depositing onto the optical fibers. At a deposition rate of 2.0 A/s, 15-20 nm of Al are deposited onto the optical fiber in step two to define the tunneling lead (#2). The tip holder is then inverted and a second evaporation of 10-15 nm using the same protocol defines the capacitance lead (#3).

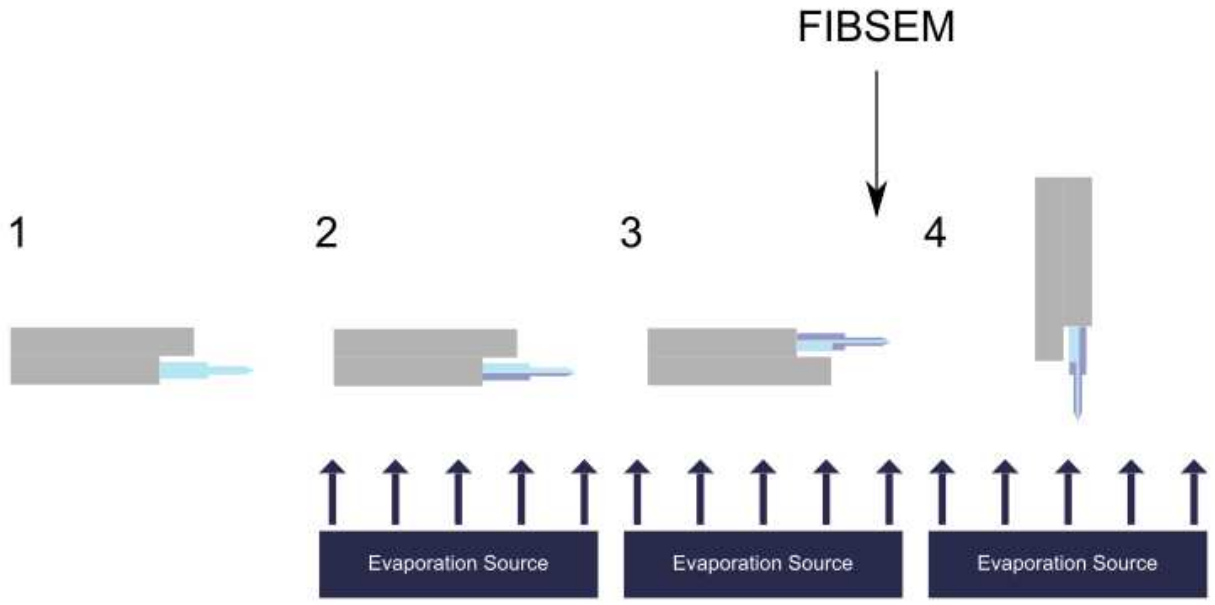

Figure 5.7 Thermal evaporation stages. 1: SCQDM probes loaded into the aluminum tip holder for thermal evaporation. 2: First evaporation of the tunnel lead, typically 15-20 nm. 3: Inverted tip holder evaporation of the capacitance lead, typically 10-15 nm. An intermediate FIBSEM step then occurs. 4: Final end-on evaporation of the QD, typically 5-7 nm.

Prior to evaporation of the apex quantum dot, an intermediate processing step involving focused ion beam milling scanning electron microscopy (FIBSEM) is performed. The novelty of the probe construction is most related to this step and will be discussed in the next section. Following the FIBSEM step, a final end-on evaporation of 5-7 nm is performed using the above protocol to define the quantum dot (#4). The steep angle of the tip's apex ensures any excess aluminum deposited on the sloped surface of the probe is oxidized and does not short the two leads to one another.

5.4 FIBSEM

The SCQDM employs a single electron box architecture to enable angstrom distance tunneling as well as single electron counting of electrons entering the quantum dot. To achieve these goals, the functional probe itself needs to be highly asymmetric, with a clear tunnel junction and capacitance junction. The steps leading up to FIBSEM only define a small asymmetry via lead thicknesses, but this is not sufficient to introduce a large and reliable enough asymmetry between the two junctions. FIBSEM introduces asymmetry to the leads and junctions two ways.[42] First, the tunnel lead is milled at a shallow angle relative to perpendicular. This step has the additional benefit of sloping the quantum dot, resulting in the tunnel junction being 10s of nanometers from the sample surface while in tunneling mode. Second, the tunnel junction site is milled lightly for a short amount of time. Both techniques result in a smoother interface between the tunnel lead and quantum dot and result in enhanced tunneling properties. The capacitance junction is relatively untouched in the FIBSEM step, resulting in a known asymmetry between the two probes, important information when mounting the probe onto the charge sensing circuit.

The aluminum tip holders, following the evaporation of the tunnel and capacitance leads, are loaded into the FIBSEM to be characterized with scanning electron microscopy (SEM). Imaging the probes end-on and perpendicular to the longitudinal direction of the optical fiber provide the information needed to determine a tip's viability. A variety of other angles were used for characterization, but in general just these two angles give a clear enough picture to decide the viability of a scanning probe.

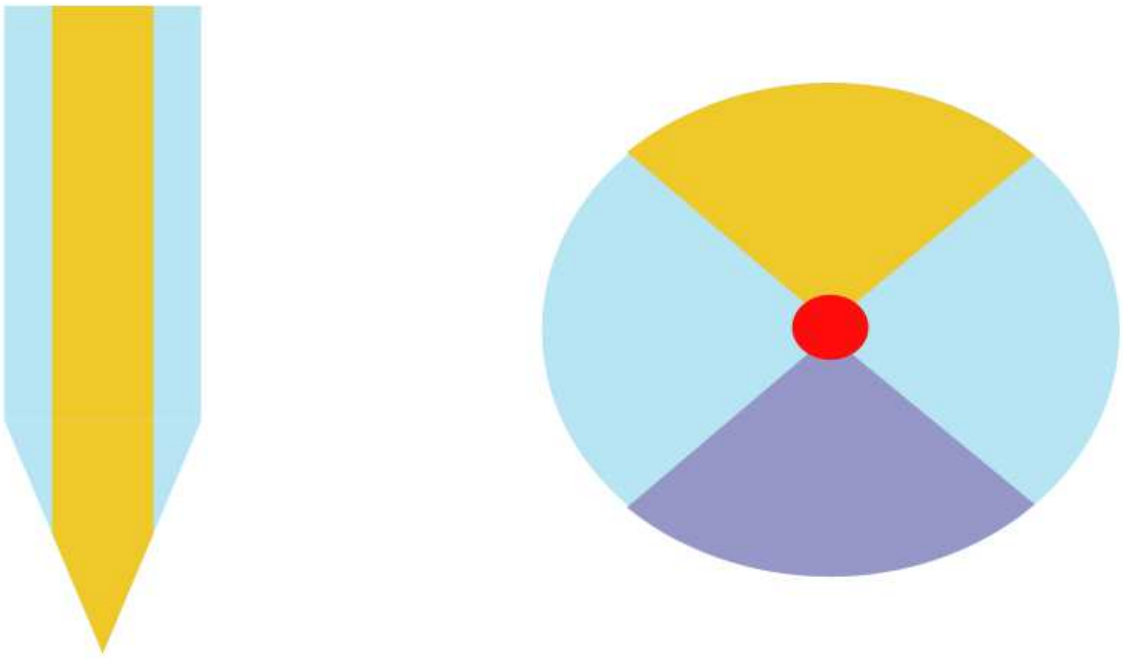

Figure 5.8: SEM characterization perspectives. Color scheme matches the schematics presented throughout. Left: View used for FIB milling and tunnel lead characterization. Right: End-on view of SCQDM probe.

Often, the evaporation stage does not result in aluminum being deposited continuously to the apex for the leads or results in shorts between the leads near the apex. End-on imaging gives the clearest view of the leads' continuity to the apex quantum dot and presence of electrical shorts. Post-FIBSEM this perspective provides the best measure of the QD size. The perpendicular viewing angle, which gives a clear view of the tunnel lead, provides information about the apex diameter, and will be the viewpoint used during the focused-ion beam milling (FIB) step. Generally, a batch of 24 tips across 4 tip holders will produce 5-10 viable SCQDM probes as determined by this characterization step.

The SCQDM probe tends to move in response to the focused-ion beam, which necessitates manual control of the beam shift and live feedback during the milling time. The FEI Helios 650 FIBSEM at the University of Michigan's Center for Materials Characterization has both functionalities and is used exclusively for creating SCQDM probes.

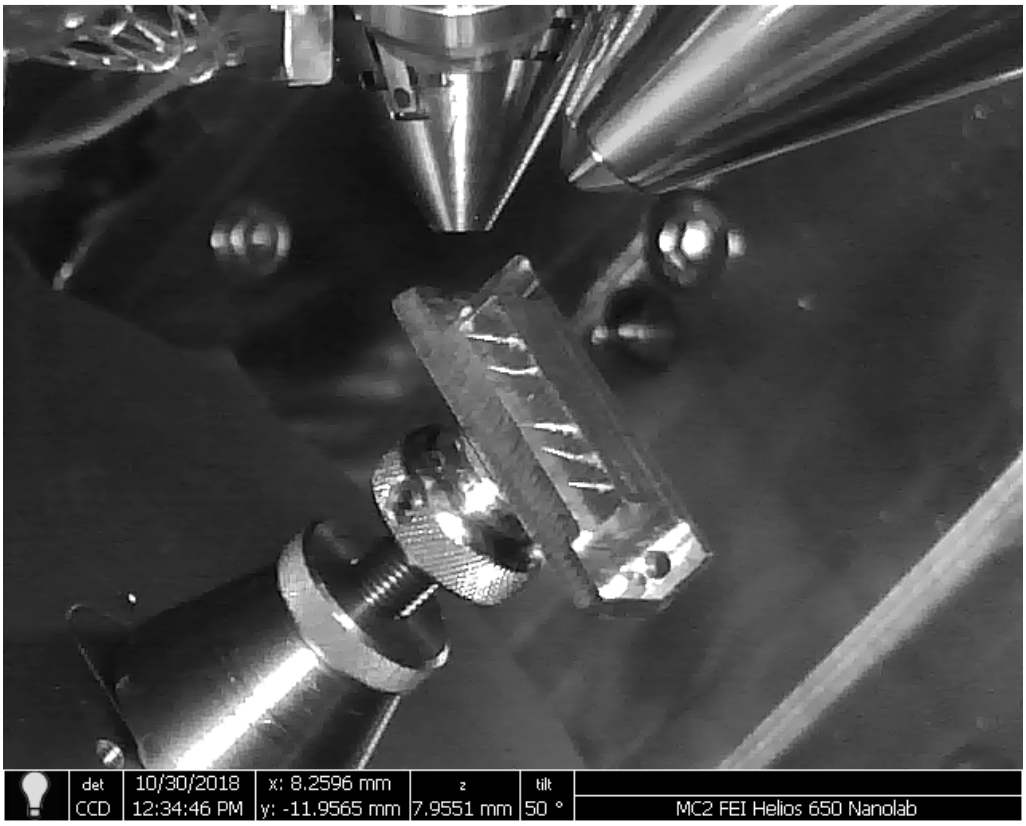

Figure 5.9: FEI Helios 650 FIBSEM. The SEM can be seen as the vertical aperture. The FIB is seen at a 38 degree angle from vertical. Tilting the sample 52 degrees results in a perpendicular cutting angle for FIB mills.

Viable tips are then milled using the focused-ion beam. Tilting the specimen stage 52 degrees results in the ion beam being perpendicular to the longitudinal axis of the optical fiber probes. In general, a 2-5-degree tilt (47-50) is employed to move the sensitive

tunnel junction away from the apex of the tip. This shallow angle over the diameter of the apex quantum dot area results in moving the tunnel junction 10s of nanometers from the tip apex used to tunnel into the surface sample. FIB mills are performed from the perpendicular perspective, to ensure the tunnel lead is continuous to the apex to be defined during the cut. Figure 5.10 shows a before and after of a FIB mill. The resulting quantum dot area for this SCQDM probe can be seen in Figure 4.6.

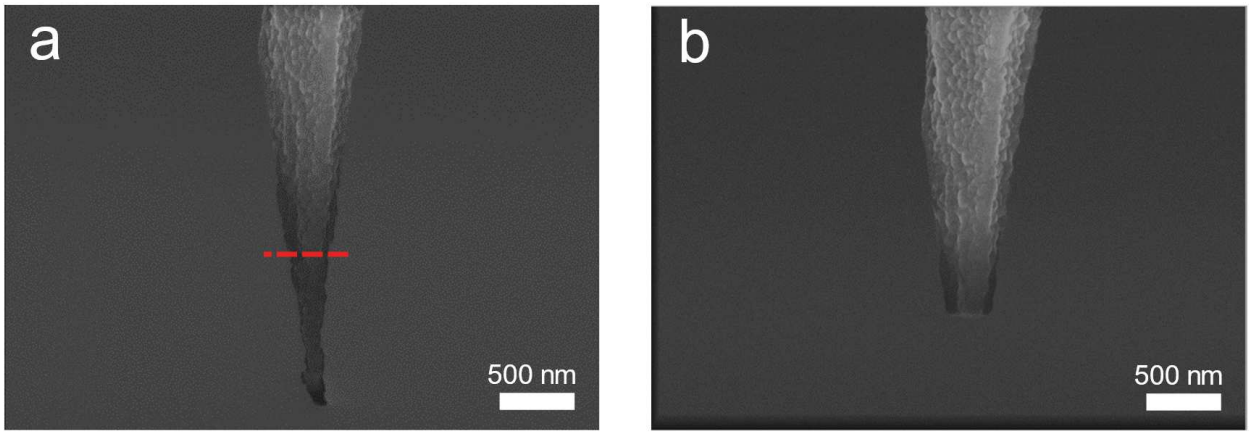

Figure 5.10: SCQDM probe before (a) and after (b) FIB mill. The area below the red line in (a) indicate the material to be milled. A milling step generally takes 10-15 seconds, with manual control of the ion beam required the entire time. A flat area for later quantum dot deposition is achieved in this step.

5.5 Charge Sensing Circuit

The interesting physics occurs on the functional probe of the SCQDM. The charge sensing circuit grants access to this interesting physics by providing the charge detection and platform for connecting this probe to the microscope's scan head and room temperature electronics. This charge sensing circuit was described in detail in Section 4.3.

A pattern of Ti/Au pads (10 nm/100 nm respectively) is sputtered onto a GaAs chip to provide contacts and a template for placing the rest of the components. Five gold wires (0.002 inch) are attached to five gold pads to provide electrical contacts for mounting inside the scanning head. A sixth gold wire (0.001 inch) is additionally epoxied for later contact to the tunnel junction. The epoxy is then cured at 120 C for 15 minutes. Next, a HEMT and 10 MΩ on-chip resistor are epoxied and cured on the GaAs chip. A series of wire bonds are performed to connect the various aspects of the circuit prior to mounting the SCQDM probe. With the circuit built, the SCQDM is mounted using epoxy to the top corner of the GaAs chip with the tunnel lead facing up and capacitance lead facing down. The connection from the HEMT gate to the capacitance lead is done by connecting a gold wire between the L-shaped contact pad and HEMT gate.

The tunnel lead is connected to the driving circuit via a thin gold wire epoxied to tip. A last series of baking solidifies the epoxy. With this final stage, the SCQDM has been built and is ready to mount inside the scan head. After connecting the 5 gold wires inside the scan head, a curve trace is performed to confirm the HEMT is working, followed by tunneling tests to ensure the probe is capable of surface tunneling.

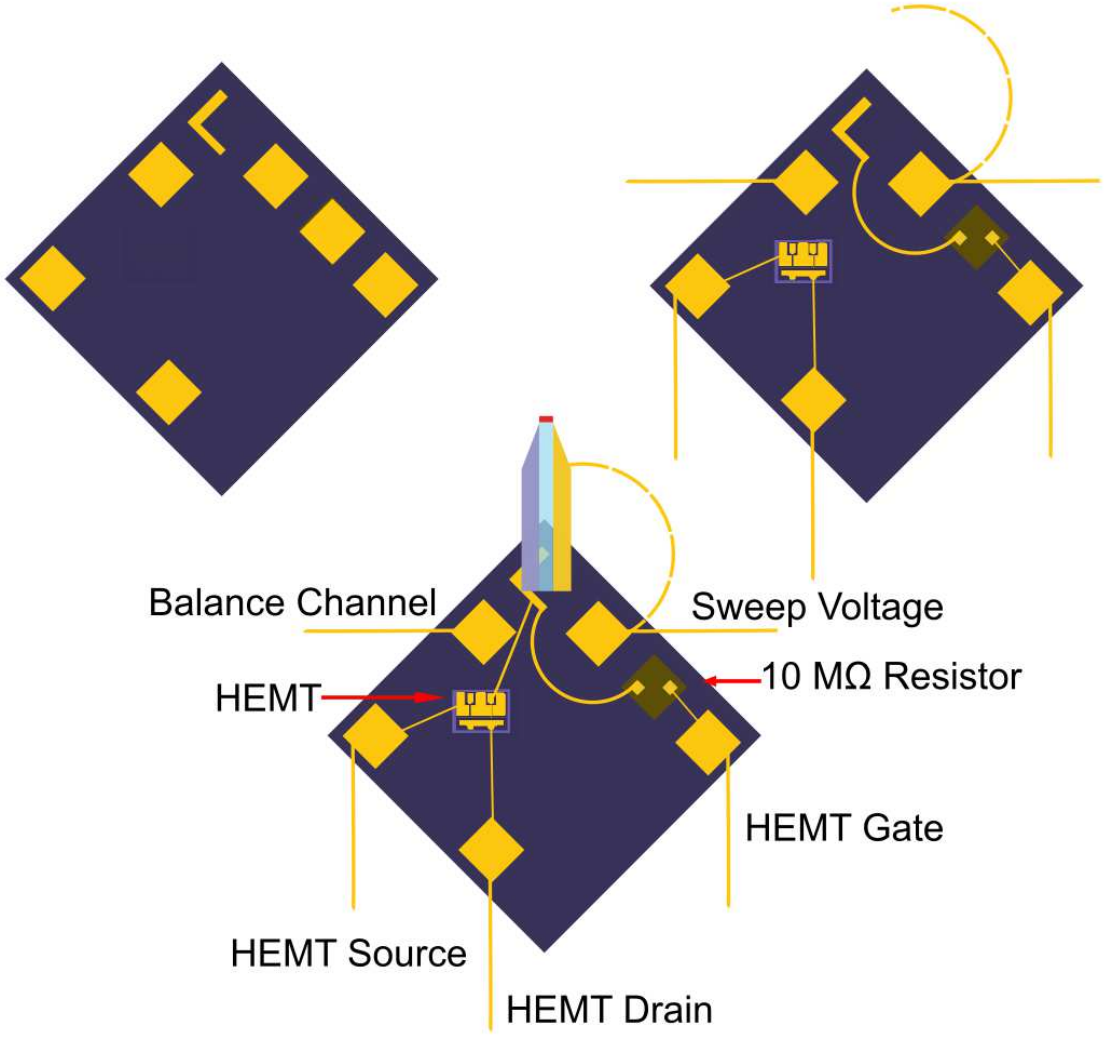

Figure 5.11: Three step process for mounting the SCQDM to the HEMT chip. Top Left: Ti/Au is mask sputtered onto a gallium arsenide chip (chosen to match the thermal expansion of the HEMT) to define the circuit pattern. Top Right: On-chip components and external wires are epoxied and connected. Bottom: The SCQDM is incorporated and connected to the charge sensing circuit and sweep lead using epoxy.

Chapter 6

Measurements: Strong-Coupling Quantum Dot Microscope

This thesis is concerned with the development and functional testing of the Strong-Coupling Quantum Dot Microscope, a scanning quantum dot probe capable of counting single electrons entering the apex quantum dot and angstrom distance tunneling into a sample's surface. Chapter 4 developed the theory behind the SCQDM's operation. Chapter 5 detailed the fabrication of the SCQDM probe and charge sensing circuit. This chapter will show measurements performed by the SCQDM showing single-electron tunneling events and cryogenic surface tunneling. QD-MZM measurements will be later performed by my successor in the Tessmer lab. Four tips have been successfully tested consecutively for single electron counting over the course of five data runs, with numerous SCQDM probes tested for surface tunneling.

6.1 Single Electron Counting

The SCQDM was developed to enable quantum dot measurements of MZMs in a scanning probe experiment. To achieve this goal, demonstration of single-electron tunneling into the apex quantum dot is key. Section 6.1 and 6.3 will detail experiments performed on two SCQDM probes towards this goal. The experiments were performed at 283 mK. Data presented are large averages of many curves taken consecutively to increase the signal to noise ratio, a necessary step considering the attofarad signal size.

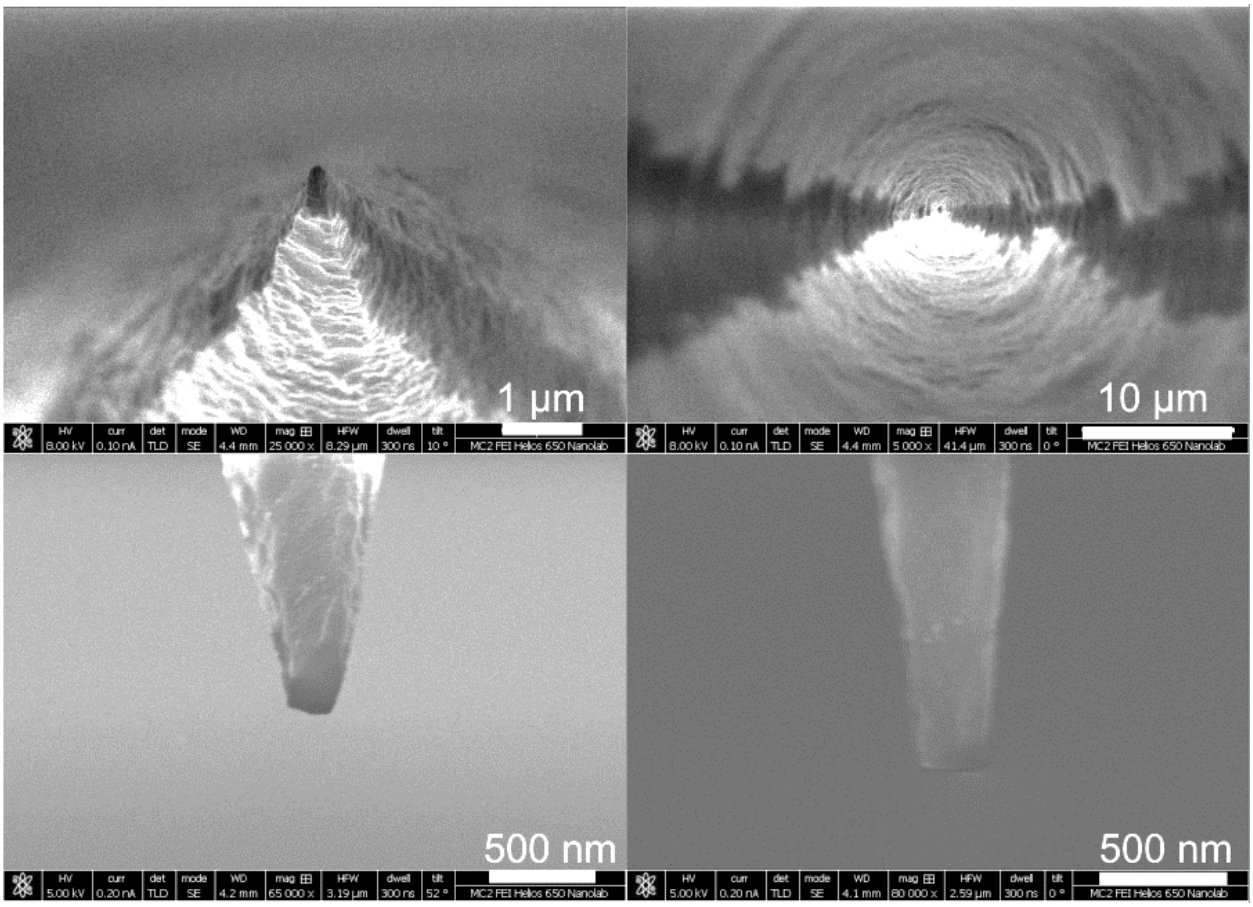

Figure 6.1: SEM images of the SCQDM probe used for Figure 6.2 and 6.3. Top Left: Tilted end-on view of the apex prior to FIB milling. Top Right: Wide end-on view of the tip apex, showing clear lead separation and an evident quantum dot. Bottom Left: 52-degree view showing the FIB mill creating a smooth transition to the quantum dot apex. Bottom Right: Profile view showing the flat apex for the quantum dot.

Figure 6.1 shows four SEM images of the probe used to record the data shown in Figure 6.2 and 6.3. The quantum dot is approximately 300 nm in diameter, with two well-formed and separated leads.

Figure 6.2 clearly demonstrates single-electron tunneling events into the apex quantum dot. The data shown here was taken after thermally cycling the tip, a method known to improve the noise level of related quantum dot microscopes.[43] Figure 6.2a

shows two independent averages of 1000 curves each, taken over the course of 11 hours. Recorded concurrently, the black curve represents even numbered sweeps and the red curve represents odd numbered sweeps. The small offset between the data sets is due to a voltage offset in the control electronics between even and odd sweeps. Averages of this type remove the relative time-dependence between the two curves, at least on the time scale of the entire data run. Time-dependent effects are explored later. Four distinct peaks of roughly equal capacitance height, highlighted with symbols, indicate four independent single-electron tunneling events into the quantum dot. The left-most peak, highlighted by the red star, is a particularly well-isolated single-electron tunneling event.

In-between the main peaks are smaller peaks which reproduce in both averages. We interpret these smaller peaks as likely tunneling events into defects or charge traps unconnected to the apex quantum dot. The charge sensing scheme employed is sensitive to any tunneling event near the tip apex, regardless of origin. Some of these peaks continue to reproduce over days, indicating their stable nature. Other features in the capacitance data tend to change over time, often disappearing completely, which could indicate quasi-static or transient tunneling events.

An experimental mode (see Section 4.3) was used to fit the single-electron peak data. The model convolutes a half-ellipse with the derivative of the Fermi function. With respect to fitting parameters, the width of the ellipse is set by the AC excitation amplitude used in the measurement, the width of the Fermi function is set by the temperature of the experiment, and the RC integration time constant is known. Two free parameters are permitted by the model. First, the baseline of the capacitance signal is free to be defined.

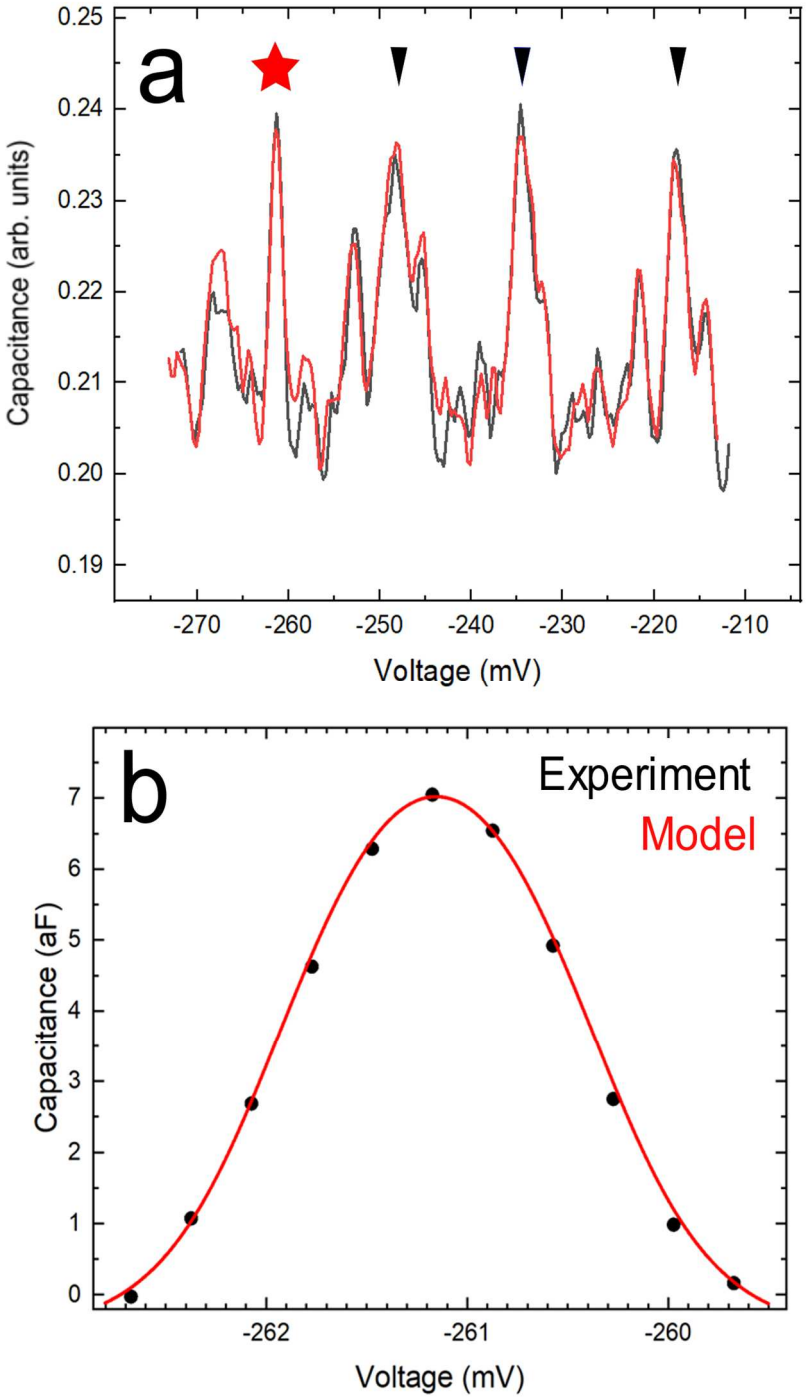

Figure 6.2: Single-electron tunneling events into the apex quantum dot of the SCQDM. (a) Wide sweep range showing four distinct peaks, highlighted by symbols, indicating single electron tunneling. (b) The well-isolated peak in (a) labeled with the red start, fit to an experimental model. The capacitance change corresponding to a single-electron tunneling event is approximately 7 aF.

Second, the lever arm parameter (Equation 4.7), the geometry-dependent ratio of the potential difference between the tunneling lead and the quantum dot, and the capacitance lead and quantum dot, is a fitting parameter. The lever arm parameter is further restricted, as it couples the width of the generated fit with the height. Ultimately, the lever arm parameter for a given experiment is extracted from the fitting function.

The red star peak in Figure 6.2a was fit to this experimental model. The baseline was chosen to be the inflection point to the left of the peak. Using the experimental values for temperature, excitation voltage, and step size, which just determines the data point spacing (283 mK, 1.2 meV, and 300 uV, respectively) the peak was fit with a lever arm parameter of 12.3. As the lever arm parameter further sets the capacitance and voltage scales, the nominally 60 mV DC sweep and 1.2 mV excitation voltage get scaled to 5 mV and 100 uV, respectively. This scaling gives a capacitance height of approximately 7 aF and 1 meV addition energy.

To better understand time-dependent charge noise, eight averages of 200 curves each (each comprising approximately 1 hour of data averaging) are presented in Figure 6.3 in chronological order from bottom to top. The main single electron signal, highlighted in figure 6.2, reproduce with only small deviations, while more minor features tend to fluctuate. For example, a peak at -267mV becomes larger over time, whereas the peak at -258mV disappears over time. Similar trends are seen throughout data runs in each probe tested. Some probes show more prominent "noise" features with less clear single-electron signatures and more changes with time. We have found that thermal cycling reduces these features on average, consistent with similar measurements of scanning single electron

transistor systems.[43] We believe thermal cycling tends to make the charge traps in the oxide barriers more stable. In other words, charges tend to be more deeply trapped in the oxide defects, rather than slowly leaking out and altering the potential landscape of our quantum dot and changing the number available competing electron-trapping sites.

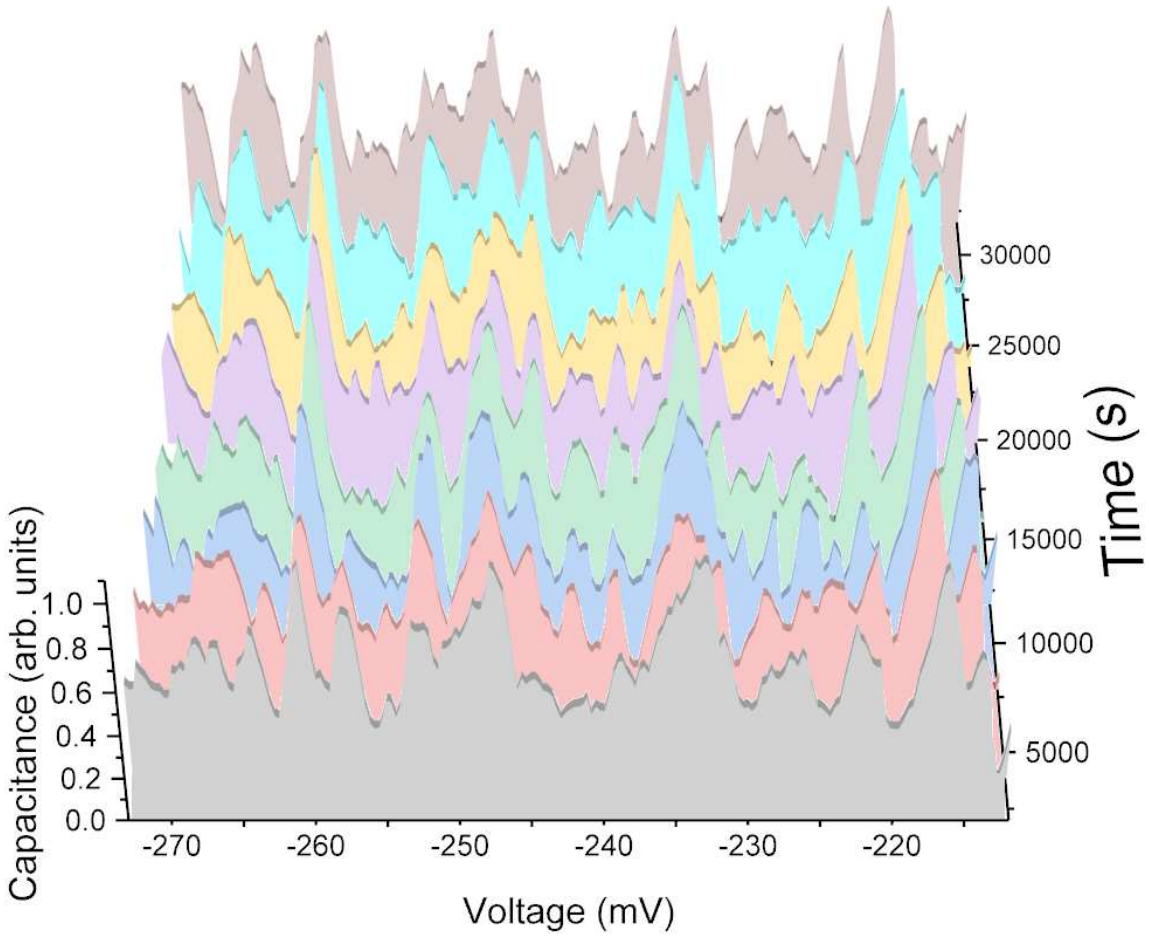

Figure 6.3: Time dependent capacitance data. Each colored curve represents approximately one hour of data, shown chronologically from bottom to top. The robust single electron peaks highlighted in Figure 6.2 reproduce consistently each hour. Other features fluctuate over time. A peak at -273 mV develops over the course of the data run, whereas a peak at -258 mV disappears. Other capacitance signals seem to fluctuate without pattern, indicating a noise floor or fluctuating charging events unrelated to the quantum dot.

6.2 Surface Tunneling

The second important functionality of SCQDM probes is the ability to tunnel into the surface of the sample. This functionality is key for controlling the coupling strength of the SCQDM to the MZM. To create a more robust probe, an asymmetric and tilted design was chosen for the SCQDM which both protects the sensitive tunnel junction from the sample's surface as well as reducing the effective size of the probe's tunneling area. Of the tips tested for single electron counting, two achieved room temperature surface-tunneling into FeTeSe prior to single-electron counting testing, with one successfully repeating surface tunneling at 270 mK after single-electron measurements. FeTeSe is a candidate Majorana sample. [18,24] Single-electron tunneling data from the latter probe is presented in the next section.

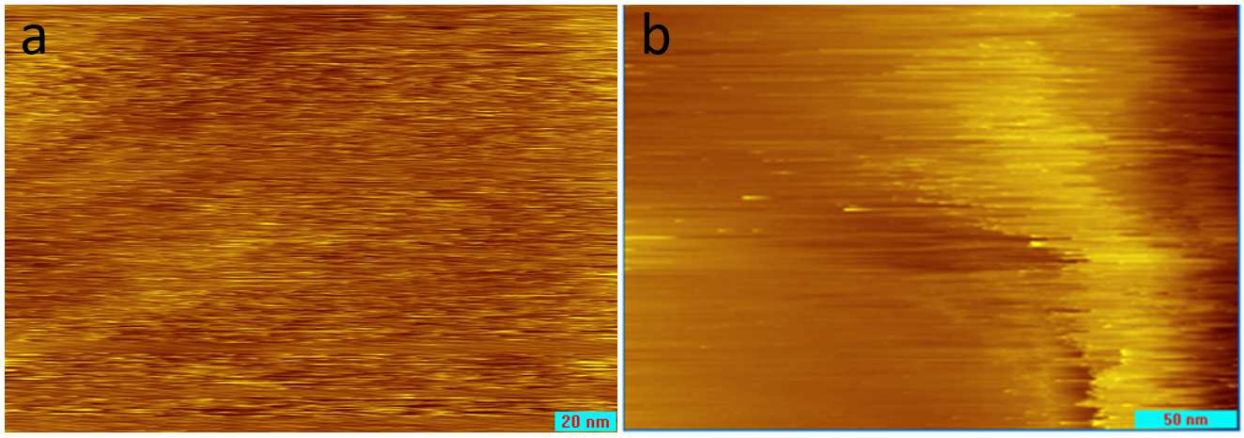

Figure 6.4: Topography recorded using SCQDM probes. (a) Room-temperature topography produces a relatively flat graphite surface, with minimal streaking. (b) Cryogenic topography at 77 K on graphite records a clear step-like feature on the surface. This step-feature reproduced over the course of seven topographies, indicating a highly stable and capable probe.

Extensive room temperature testing was performed with SCQDM probes with well-resolved quantum dots. Over twenty SCQDM probes were tested in this manner, successfully tunneling into the sample surface with varying levels of stability in the tunneling current. In addition, a few tips were tested successfully for topography. Topography is not an intended feature of the SCQDM but is a clear demonstration of the tunneling capability. Figure 6.4a shows room temperature topography performed on graphite with a SCQDM. The topography has minimal streaking and records an overall flat surface. Topographic testing was also performed using a SCQDM probe at 77 K on graphite to test cryogenic tunneling capabilities. This topography is shown in Figure 6.4b. A clear step-like feature is evident and reproduced for seven consecutive topography measurements. As topography is not an intended feature of this probe, , no topography was performed at sub-Kelvin temperatures to avoid damaging viable SCQDM probes.

6.3 Additional Single Electron Counting

One of the key goals for the SCQDM was being able to tunnel the tip into the surface of the sample without destroying the apex quantum dot. The following SCQDM probe was tested for single-electron tunneling events after it had tunneled into the surface of FeTeSe at room temperature. The probe was then able to tunnel into the surface of the sample at 270 mK, an important step towards measuring Majorana samples using the SCQDM. Figure 6.5 shows SEM images of the SCQDM probe used for the data presented in Figure 6.6. Single-electron capacitance data shown here was not taken in coupling range of the MZM.

Figure 6.6a shows a wide voltage range sweep taken with this probe at 283 mK showing numerous single-electron tunneling events with roughly periodic spacing. A background capacitance has been subtracted away. The overall periodic signal is robust, but spurious capacitance signal does also obscure the periodicity at certain energies. Three particularly pronounced and isolated peaks occur around -238 mV. These three peaks have been fit with the same fitting function employed in Figure 6.2, with a lever arm parameter of 9.5. The nominally 120 mV DC sweep and 600 uV excitation voltage are scaled to 12 mV and 60 uV respectively. Applying this scale to the larger data range sets the electronic addition energy at approximately 300 uV for this probe. This is generally consistent with the larger quantum dot of this probe, which reduces the addition energy to add a single electron to the quantum dot. Subsequent measurements repeated this periodic capacitance signal, pointing to a highly robust probe.

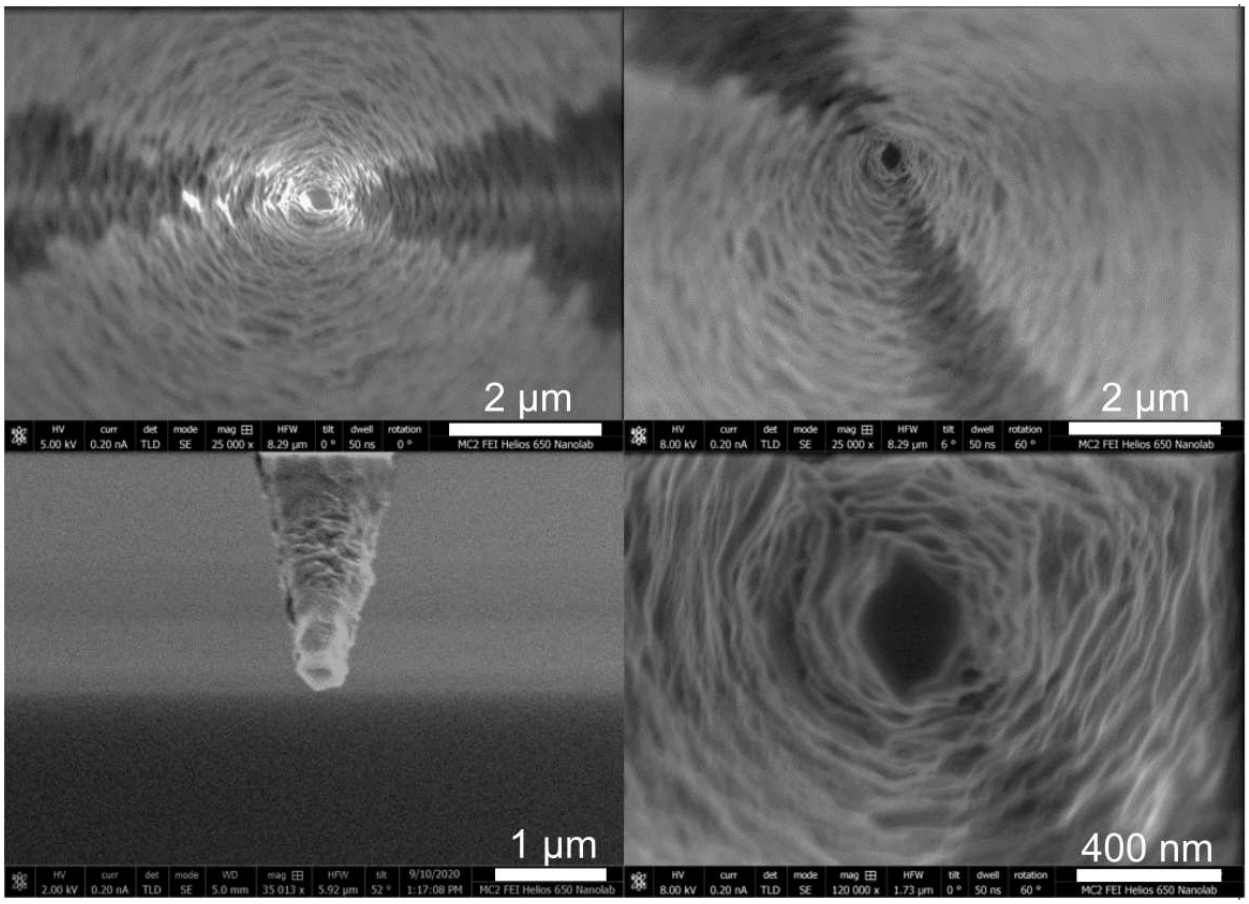

Figure 6.5: SEM images of SCQDM probe used for Figure 6.6. Top Left: Wide end-on view of the apex. Top Right: Tilted end-on view of the apex showing clear lead separation and quantum dot. Bottom Left: 52-degree view showing the apex and tunnel lead. Bottom Right: End-on view showing a well-resolved quantum dot ~400 nm in diameter.

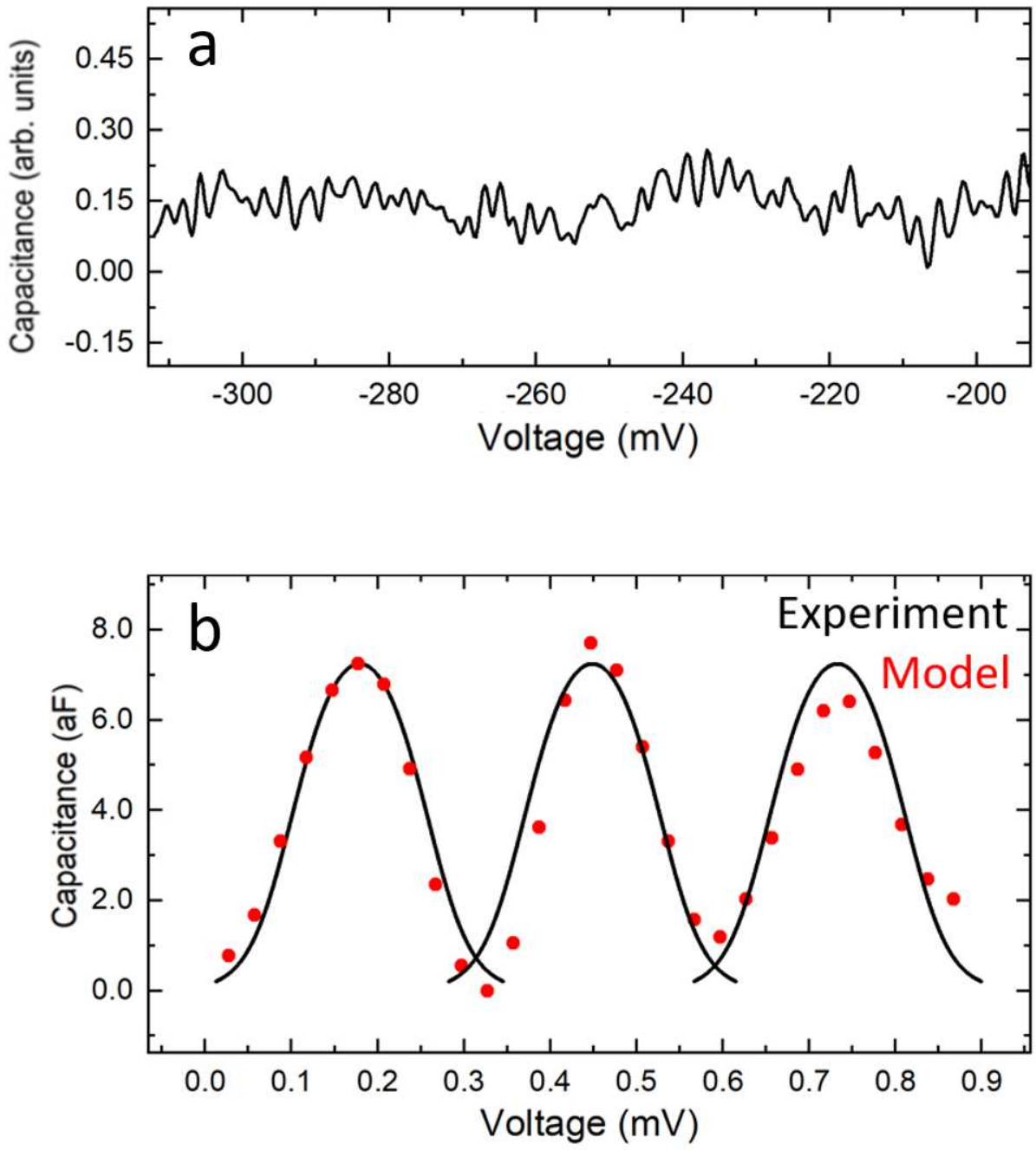

Figure 6.6: Periodic single electron tunneling events. (a) Wide voltage range capacitance sweep showing numerous single electron peaks, with roughly 3 meV periodic spacing. (b) Three well-isolated and pronounced peaks were fit with the same fitting function employed in Figure 6.2. A lever arm parameter of 9.5 fits the data well, indicating a real energy spacing of 300 uV and capacitance signal of approximately 8 aF.

6.4 Outlook

Four consecutive SCQDM probes over five consecutive data runs have generated reproducible capacitance signals with peaks indicating single electron tunneling events. Periodic single electron-tunneling event spacing has also been recorded. The continued success of generating reproducible capacitance signals, numerous successful room-temperature tunneling tests, and cryogenic tunneling indicate the SCQDM is a viable instrument. Moving forward, the intention is to use the SCQDM to perform single-electron tunneling measurements through the QD when coupled strongly to a MZM on the surface of a sample. The modification of the capacitance signal should be unique when coupled to a MZM, as compared to other more trivial modes.[17]

Future experiments using the SCQDM intend to focus on measuring MZMs. The leading candidate samples to be studied are bulk FeTeSe [18], topological insulator / superconductor heterostructures [13], and topological superconducting Josephson junction samples.[10] Each of these sample measurements intend on searching for Majorana zero modes in the core of a superconducting vortex. The FeTeSe sample was shown in this thesis to have been successfully tunneled into using a SCQDM probe, which further counted single electrons entering the quantum dot when positioned away from the sample. Future measurements will attempt to count single electrons in the strong coupling regime between the QD and MZM.

As part of a collaboration with the 2D Crystal Consortium at Penn State University, samples comprised of a bottom layer of superconducting $NbSe_2$ and top layer of Bi_2Se_3 are being prepared. Majorana zero modes are theorized to exist in the core of superconducting

vortex in this sample. Related samples of this kind have been previously probed using STM to search for Majorana zero modes.[20] STM measurements will be performed by our group looking for MZMs. Successful measurement of a zero bias peak using STM will then be followed with a repeat measurement using the SCQDM. Lastly, measurements on Josephson junction samples, using Nb and Bi_2Se_3 as the superconductor and topological insulator respectively, will be carried out in a similar fashion to the heterostructure sample. The vortex in these samples is a Josephson vortex, as compared to the Abrikosov vortex mentioned thus far, but this particular detail does not change the SCQDM measurement.

In conclusion, the Strong-Coupling Quantum Dot Microscope was developed over the course of this thesis. The core functionalities of this probe were demonstrated. Single-electron tunneling events were measured entering the apex quantum dot, measured as a capacitance change using a highly sensitive charge-sensing circuit. Measurement and fitting of individual electron peaks, as well as a periodic pattern of electrons tunneling into the quantum dot, were demonstrated. Surface tunneling was demonstrated repeatedly. Presented here were proof-of-concept topography measurements, showing the SCQDM is a capable surface tunneling probe. The development of this microscope was spurred on by the desire to use quantum dots to measure signatures of MZMs in samples that lend themselves to study by scanning probe methods. Future experiments will carry out these experiments, looking for unique modifications to the single-electron signal when the QD is coupled strongly to MZMs.

APPENDICES

APPENDIX A:

Dual Topological Proximity Effect

The following appendix has been adapted and summarized from reference [44]. Interested readers are directed to the reference for additional details.

A.1 Introduction

Proximity effects are a general phenomenon well-studied in condensed matter physics. At the interface between two materials with different long-range orders, correlations from one material can leak into the other to some finite depth. The superconducting proximity effect, by which the superconducting correlations (Cooper pairs) leak into an interfaced material, is particularly useful in the creation of Majorana zero modes, as evidenced by its ubiquity across distinct Majorana platforms. Ian Dayton, a former member of our lab, performed measurements of PbBi islands on top of the topological insulator Bi_2Se_3, establishing a length scale for this superconducting proximity effect leaking into the surface Bi_2Se_3. Additionally, there were indications the topologically protected surface state (TPSS) of Bi_2Se_3 leaking onto the superconducting islands.[45] Since Ian's measurements and the measurements to be described, an additional group reported this phenomenon in thin film Pb(111) on $TlBiSe_2$ indicating the existence of an inverse effect.[46] This inverse proximity effect, by which the TPSS leaks into the superconductor, has been dubbed the dual topological proximity effect.

This appendix details a series of STM experiments and theoretical efforts towards understanding and characterizing this effect in heterostructures comprising a bottom layer of Bi_2Se_3 with a thin layer of Nb on top. Contrary to previous expectations, we demonstrate the TPSS is not confined to the interface between the superconductor and topological insulator, but instead the TPSS can leak through the superconductor to the superconductor/vacuum interface.

A.2 Samples

The salient features to be studied are the superconducting energy gap of the overlayer of Nb, pinned to the Fermi level, and the Dirac cone of Bi_2Se_3, arising from the TPSS. We present data from two types of samples: A and B. Samples of type A (40 nm and 60 nm Nb) allow us to separately probe both the Dirac cone and superconducting energy gap on the same spectra, as well as an in-situ control sample of Nb without underlying Bi_2Se_3.

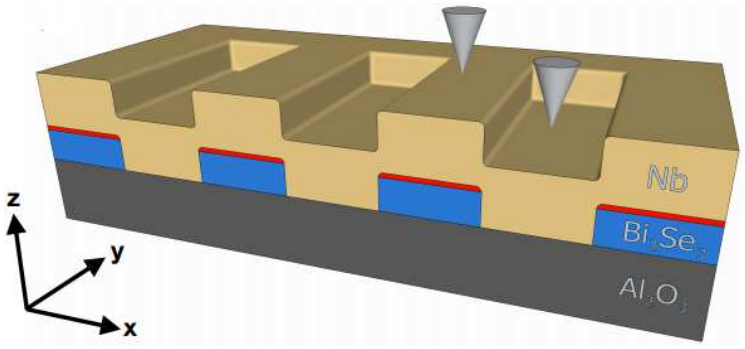

Figure A.1: Schematic of sample type A. Control measurements (right tip) can be performed in-situ to ensure stable tunneling. Measurements done by the left tip then probe the TPSS leaking through the superconductor. Samples of type B do not have control strips.

A schematic of sample type A is shown in Figure A.1. Samples of type B superimpose these features, allowing direct comparison to a phenomenological model of the hybrid system. Samples of type B are 40 nm Bi_2Se_3 with a top layer of 30 nm Nb.

A.3 Measurements

STS is performed by applying a DC voltage between tip and sample, which is summed with a 100 Hz sinusoidal voltage of 0.3-4.0 mV rms. dI/dV-versus-V provides a finite temperature (4.2K) measurement of the density of states, which effectively probes the two salient features.

Measurements on samples of type A take advantage of the energy offset between the Dirac cone of the TI and the superconducting energy gap of Nb. Wide range voltage measurements like Figure B.2b show two features of the underlying TPSS: the Dirac cone, a minimum at -300mV, and a gap-like conduction band feature at 0V consistent with Bi_2Se_3.[47] Closer range measurements reproduce the latter gap, in addition to showing a gap consistent with the superconducting energy gap of Nb (Figure B.1a). Together, these are powerful evidence of the leakage of the TPSS through the overlayer Nb. Additionally, the ability to perform control measurements on pure Nb provides an important verification on the quality of the STM (Figure B.2c). The ability to fit the superconducting energy gaps to a BCS s-wave superconducting energy gap model further solidifies our findings.

Magnetic field measurements provide an avenue for verifying this effect. Figure B.3a shows a wide voltage range measurement on 60 nm Nb on Bi_2Se_3 in a magnetic field.

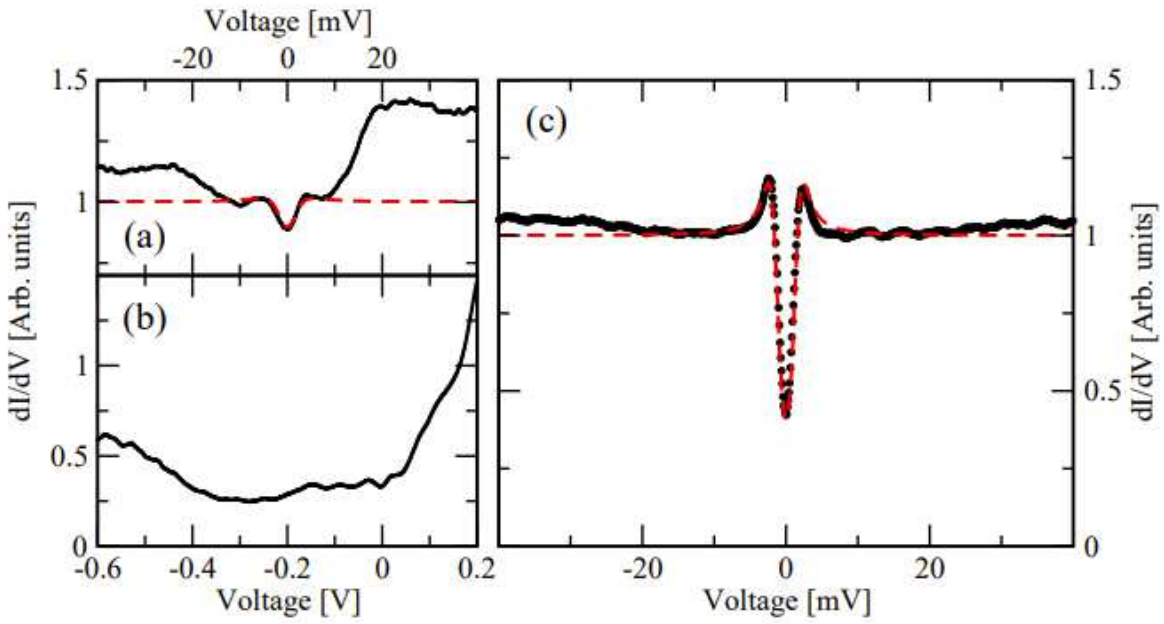

Figure A.2: Measurements on samples of type A. (a) dI/dV curves taken around the Fermi level on 40 nm Nb on Bi_2Se_3. Two gap-like features are apparent. The smaller gap appears to be of superconducting origin and has been fitted with a BCS s-wave superconducting energy gap fit. The fit parameters are T=4.2K, Δ= 1.5 meV, and mean free path l = 32nm. The larger gap is consistent with a gap like-feature found in the conduction band of Bi_2Se_3 and is not the Dirac cone. (b) Wide range measurement on the same sample, showing a local minimum around -300mV consistent with the Dirac cone of Bi_2Se_3. The gap feature at the Fermi level is consistent not with superconductivity, but the band structure feature in the conduction band of the TI. (c) Control measurement done on 40 nm Nb, fit with the BCS s-wave superconducting energy gap fit. The fit parameters are T=4.2K, Δ= 1.5 meV, and mean free path l = 200nm.

With increasing magnetic field, the large gap feature diminishes, consistent with the reduction of the superconducting energy gap (Figure B.3b), but doesn't completely disappear, indicating the original gap was a convolution of the superconducting energy gap and the gap-like feature found in Bi_2Se_3. Figure B.3a shows this superconducting energy gap diminish as a function of magnetic field on the Nb control strip.

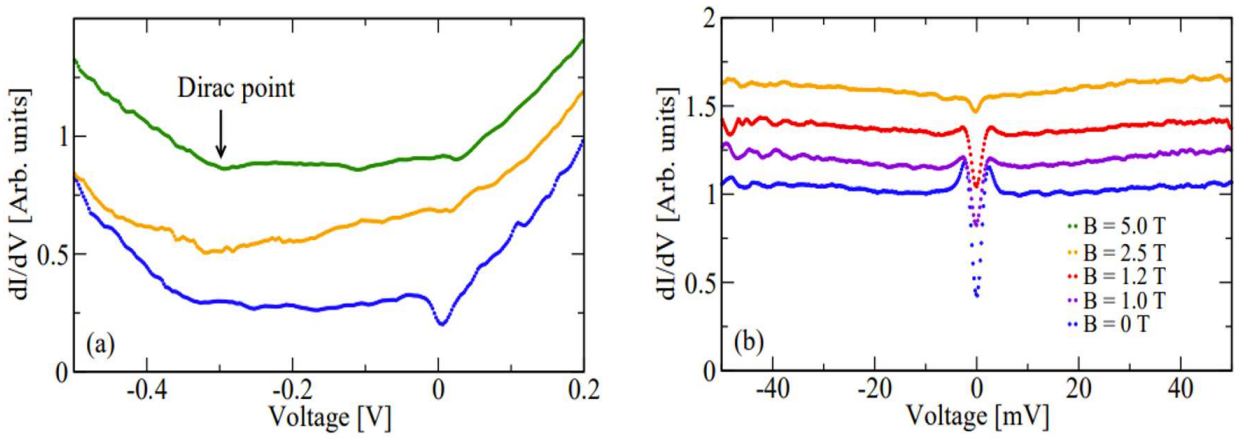

Figure A.3: Measurements on samples of type A in an external magnetic field. (a) Increasing magnetic field diminishes, but does not destroy, the gap-like feature at 0V, indicating a non-superconducting origin. 60nm Nb. (b) The reduction of the superconducting energy gap of pure Nb as a function of increasing magnetic field.

Lastly, measurements were performed on samples of type B. Nitrogen doping on Bi_2Se_3 has been shown to shift the Dirac cone towards the Fermi level. Using this effect, samples were prepared with Dirac cones close to the Fermi level, to allow for superimposed measurements of these two effects.

Our theory collaborators developed a model for samples of this type,[48] which considers the Hamiltonian of the BCS superconductor, TPSS, and a two-particle local coupling between surface states and metallic states.

$$H = H_{BCS} + H_{TPSS} + H_C \tag{A.1}$$

A phenomenological model was developed using this Hamiltonian, and a fitting function was performed on STM measurements of samples of this type. Fits shown in red below use the standard BCS s-wave superconducting energy gap fit employed in Figure B.2. Fits shown in orange are from the phenomenological model and show great agreement with the

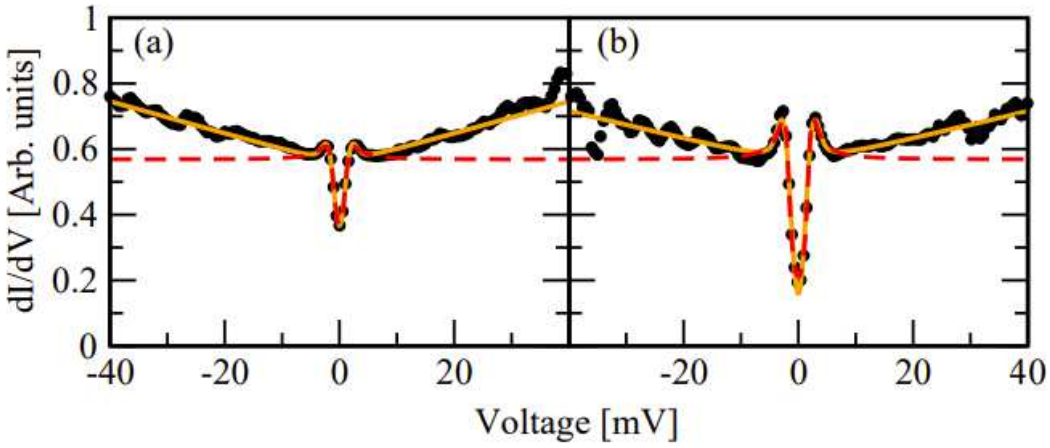

Figure A.4: Measurements on samples of type B. (a-b) STM measurements are shown in black. The phenomenological model fit is shown in orange. The BCS s-wave superconducting energy gap fit is shown in red. The model captures the salient features of the experiment, namely the lifting of the density of states outside of the superconducting energy gap quite well.

data. The presence of the superposed Dirac cone on the superconducting energy gap results in a large lifting away from the coherence peaks, a lifting capture well by the coupling term of the Hamiltonian. This indicates the TPSS are leaking to the surface.

In summary, we present evidence for a dual topological proximity effect, whereby the TPSS leaks through the superconductor to the surface. However, we were not able to discern a length scale for this effect, an important value for proximity effects generally. Ramped samples, which provide the best avenue for establishing this length scale, are being developed and should provide a robust measurement of the length scale for this dual topological proximity effect.

APPENDIX B:

Fabrication Expanded

The development of the fabrication process for SCQDM probes underwent numerous iterations at each stage of fabrication. In fact, the bulk of this thesis work was concerned with the fabrication of the SCQDM probe. The purpose of this appendix chapter is to explore alternatives and considerations for each step described in Chapter 5. The material presented here is not vital to understanding the fabrication process in its current form but provides much needed context and guidance for future researchers working on the SCQDM. For those researchers, the sections of this appendix are best read after the corresponding section in Chapter 5, as it was written with this flow in mind.

B.1 Chemical Etching

Over the course of developing this chemical etching method for the SCQDM, a few common pitfalls have been identified. Overwhelmingly, the number one mistake made in this process is etching away too much of the exposed core/cladding. The region of the tip inserted in the hydrofluoric acid will experience no tapering and be completely etched away. If the tips are mounted in the Teflon tip holder with too much of the jacket sticking out of the tip holder, or equivalently, the tip holder is placed too low into the beaker, then the resulting tips will have sub-millimeter exposed core/cladding, which makes connecting the probe to the charge sensing circuit extremely difficult and in most cases impossible.

The best way to avoid this issue is to load the tips into the tip holder with just a small amount of the jacket exposed (enough to grab with tweezers), and ensure the tip holder doesn't penetrate the surface of the oleic acid. Additionally, any angle between the tip holder and oleic acid top layer will result in different etching lengths across the tip holder. Ensuring parallel surfaces ensures uniform etching across the 30 tips, which are spread out radially from the center of the tip holder.

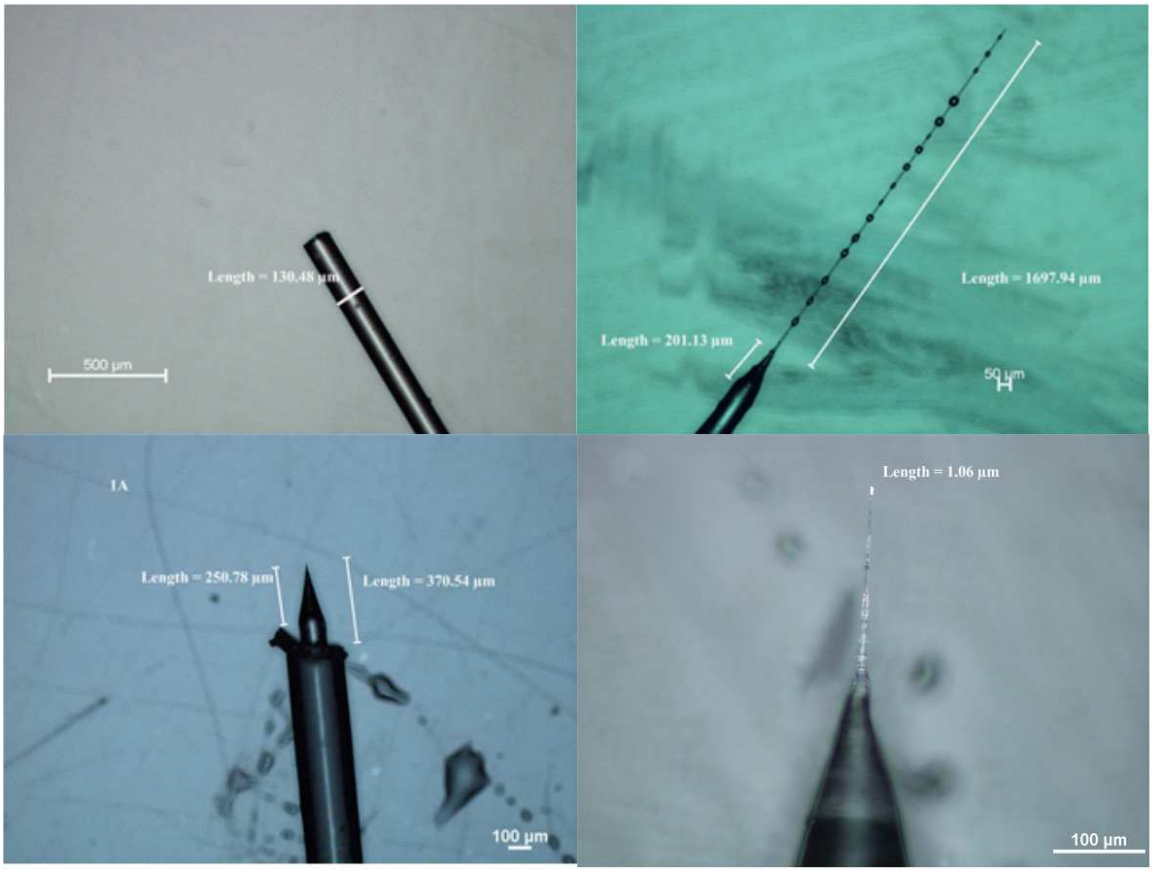

Figure B.1: Optical images of defective SCQDM optical fibers. Top Left: Optical fiber etched for too long, resulting in a flat end. Top Right: Optical fiber not etched long enough. Bottom Left: Incorrectly loaded optical fiber, resulting in too small of an optical fiber apex to mount electronics. Bottom Right: Improper etching, most likely due to moving the fibers once inserted into the etching solution.

The quoted etch time, 38 minutes 30 seconds, is both the optimal and the minimal amount of time for etching. Any less time and the apex diameter of any tip is overwhelmingly micron sized, and any more time results in completely etching the probe, resulting in a flat 125um apex.

B.2 Thermal Evaporation

While developing the thermal evaporation procedure, several modifications were tested with varying degrees of success. Some of the first iterations of the SCQDM employed titanium/gold tunneling leads, with a thin 2-3 nm end-on aluminum evaporation and oxidization prior to the quantum dot deposition. The double layer of oxide on the capacitance lead, once from native oxidization from the lead's deposition and once from the quantum dot oxide deposition, made a more insulating capacitance junction. The Ti/Au tunnel lead would not form its own native oxide, defining the asymmetry needed. None of the probes prepared in this manner successfully counted single electrons, but many were able to tunnel into the surface of a sample.

Processing temperatures were well below the critical temperature for "purple plague" and other intermetallic formations at the aluminum/gold interface, a common failure mode in high temperature bonding applications. The most likely failure mechanism was a short between the quantum dot and gold tunnel lead. In the most recent (successful) iterations, the aluminum tunnel and capacitance junctions form natively on the leads themselves prior to quantum dot evaporation. Most likely, the tunnel junction oxidation

step in these earlier iterations did not provide complete coverage over the junction area, allowing channels for conduction. A thicker aluminum deposition may fix this effect, but may also introduce unoxidized aluminum, which would serve as charge traps. Ultimately a completely aluminum probe produced consistent results and further testing with gold was abandoned. Copper leads were tested, but the formation of copper oxide is a continuous process and would result in constant degradation of the probe. Silver and Pb (lead) leads were considered but not tested. The native oxide formed on Pb is thinner than Al, so this is an attractive candidate for future development.

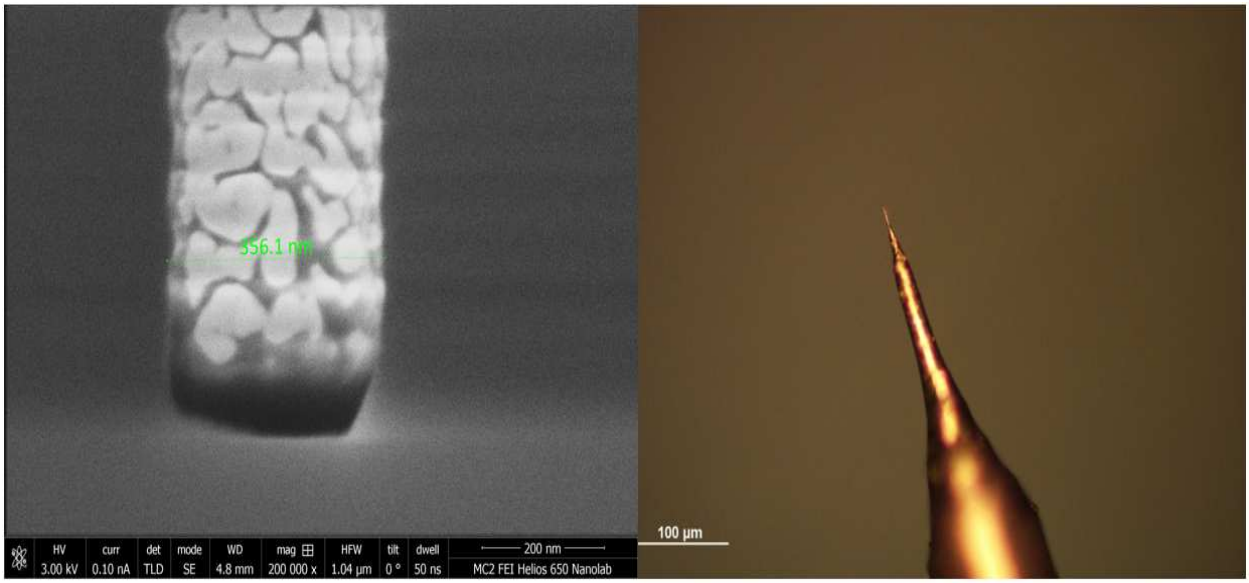

Figure B.2: Alternative metals used for leads. Left: Gold was an attractive material for the tunneling lead due to its conducting properties, but ultimately the aluminum/gold interface proved difficult. Additionally, the gold leads tended to FIB mill under ambient ion imaging, making them difficult to mill without destroying the leads completely. Right: Copper lead from the first iteration of the SCQDM probe. Copper was a poor choice and quickly abandoned.

Small tunnel junctions, such as those employed in the SCQDM, are highly sensitive to electrostatic shock. Prior to the creation of the aluminum tip holders, SCQDM were

individually mounted on copper tabs during processing and attempts to ground the leads were made with gold knots. The gold wire successfully shorted the leads, determined using a multimeter, but were deemed unnecessary once the aluminum tip holders were introduced.

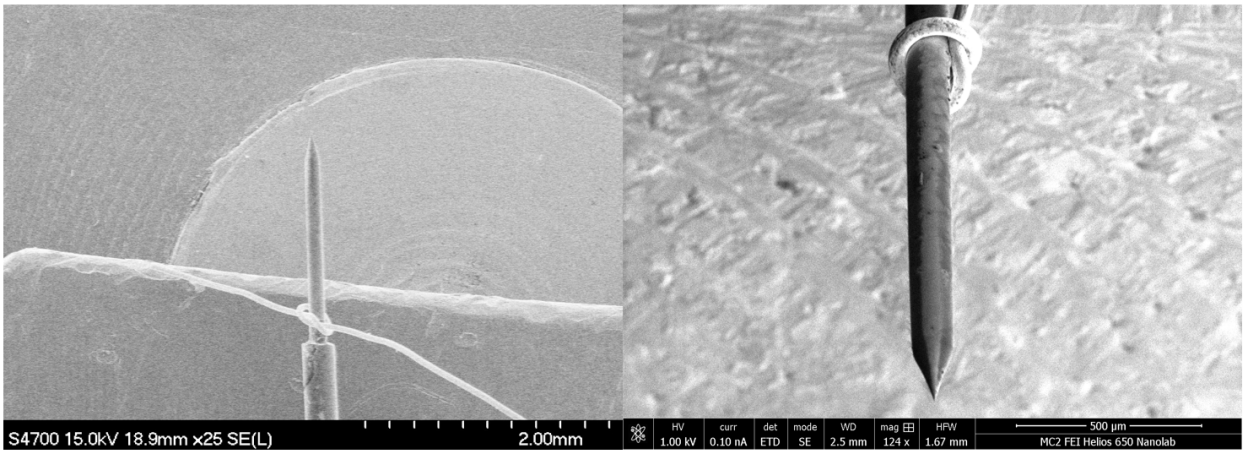

Figure B.3: SEM image of the grounding gold wire on a metalized SCQDM probe. The gold wire appears as the tied knot around the SCQDM probe. The introduction of the aluminum tip holders removed the need for this extra grounding step.

Optimal lead thickness is determined by three criteria. First, the lead must be thick enough to remain intact during probe mounting. Second, the lead must be continuous to the apex of the tip. Third, the leads must not short one another. 100+ nm lead depositions overwhelmingly short the tunnel and capacitance leads. The range of 10-20 nm seem to satisfy the three requirements best but thicknesses up to 30 nanometers should be viable under the right circumstances, with a lower bound of around 10 nm. One additional control knob available is the rotation of the thermal evaporation stage during deposition. Rotating the stage while depositing tends to the increase the radial arc covered by the deposition, resulting in covering more surface area on the probes. Rotating the stage

during the tunnel lead deposition, but not during the capacitance lead deposition, resulted in noticeable coverage difference, even with the same deposition rate and amount. The main drawback to not rotating is an increased probability of imperfect lead deposition near the apex.

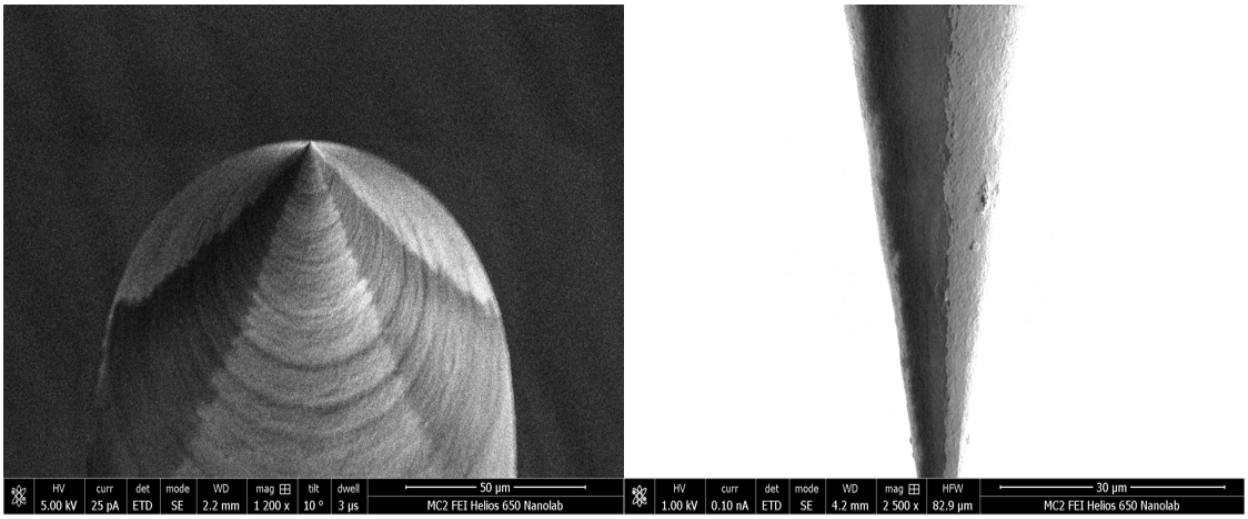

Figure B.4: Examples of lead deposition differences. Left: Different amounts of aluminum deposition results in different overall lead areas, especially near the apex. In this image, the tunnel lead is in the background and capacitance lead in the foreground. Right: A SCQDM imaged from the side, showing the thick tunnel lead on the right and a thin capacitance lead on the left, separated by the dark glass probe.

The quantum dot thickness is 5-7nm. Any thicker, and the leads can become shorted to one another if the aluminum deposited on the sloped part of the probe does not oxidize. Any thinner and the quantum dot completely oxidizes. The quantum dot at 5-7 nm still forms a native exterior oxide layer, resulting in a very thin quantum dot on the order of 1-3 nm in height. The electrostatics of the quantum dot are dominated by the surface area of the quantum dot.

Aluminum coverage on the leads strongly depends on the quality and cleanliness of the optical fiber. The cleaning stage after etching is integral to successful metal depositions. Excess debris from the glass fiber results in disruptions of the lead deposition, but the main culprit for poor lead deposition is residual solvents. Oleic acid, hydrofluoric acid, acetone, isopropyl alcohol, or water insufficiently removed from the optical fibers cause large, circular spotting where aluminum will not stick. Introduction of the final baking step prior to thermal evaporation has reduced the incident of this effect and should not be skipped. .

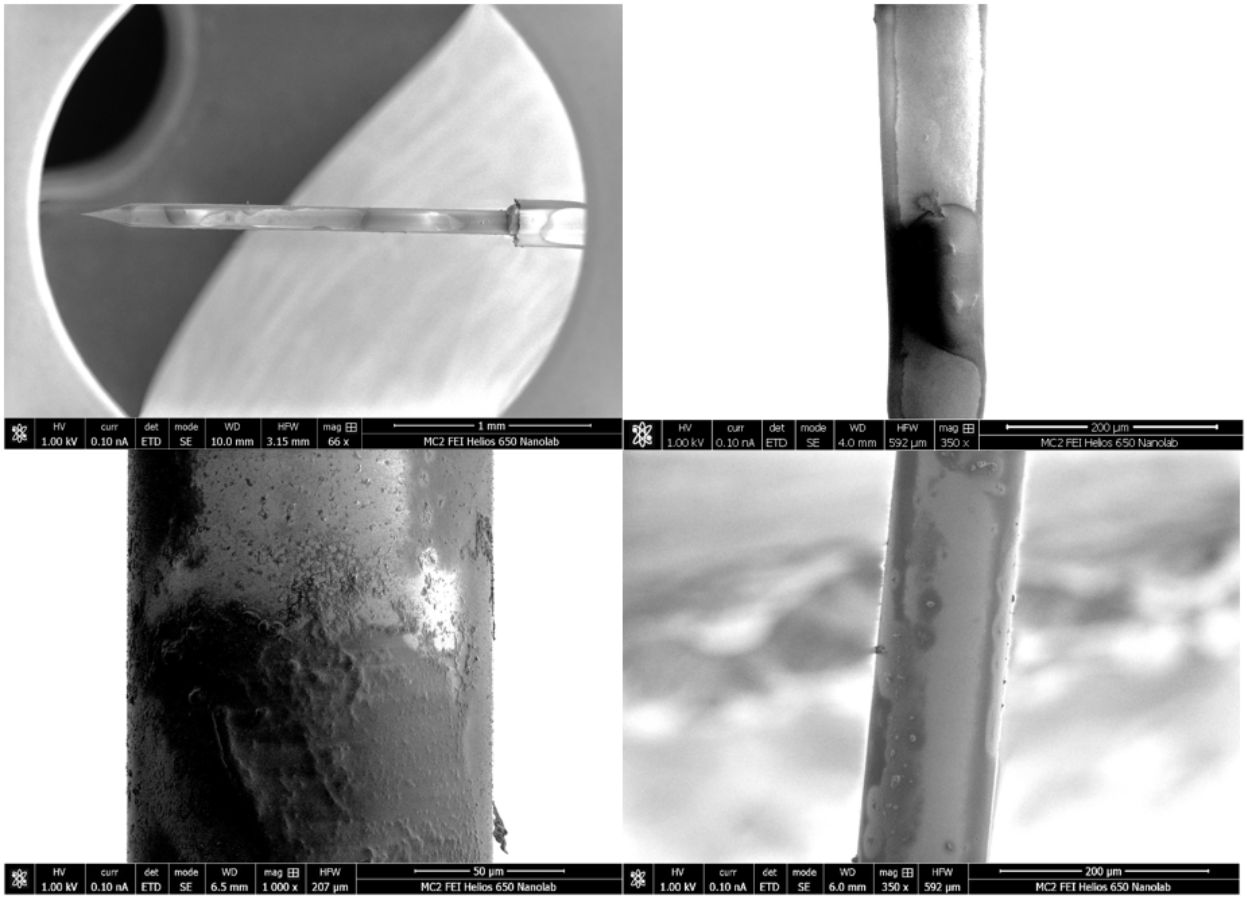

Figure B.5: SEM images of poor SCQDM lead depositions. Etching defects can cause ripples on the glass surface, which further disrupts the thin aluminum lead deposition. Improperly cleaned SCQDM probes result in splotchy lead depositions. Each effect or their combination result in poor lead quality.

Controlled oxidation was performed on several iterations, but eventually deemed unnecessary. A mixture of 90% Argon 10% Oxygen would be introduced to the thermal evaporation chamber after aluminum deposition at a pressure of 10^{-2} Torr for up to 45 minutes. The aluminum oxide comprising the tunnel and capacitance junction is formed after FIBSEM, which is not equipped to introduce oxygen to the vacuum chamber after milling, and therefore any benefits to controllably oxidizing the leads would be lost during the mill stage. The initial motivation for this controlled oxidation step was to cleanly oxide the quantum dot oxide layer (not incorporated in the final recipe) to provide robust junctions without pinholes. The final quantum dot evaporation was never considered for controlled oxidation, as pinholes through the oxide would only benefit the surface tunneling capabilities.

B.3 FIBSEM

Three SEMs were used over the course of this thesis: Hitachi S-4700 SEM, Carl Zeiss Auriga Dual Column FIBSEM, and FEI Helios 650 FIBSEM. The former was used most prior to introducing FIB processing to the fabrication and provided the poorest quality images. SCQDM are not easy to image, as the surface being imaged is either silica or aluminum oxide. The insulating probe therefore proved difficult image successfully using the Hitachi S-4700 SEM (Figure A.3 was taken using this SEM). The latter FIBSEM systems were capable of imaging the tip apexes in high detail. The Carl Zeiss, housed at the College of Engineering at MSU, provided the first FIBSEM testing on SCQDM probes and results were

promising. A combination of technical repairs and lack of live feedback during the milling stage resulted in the need for an alternative.

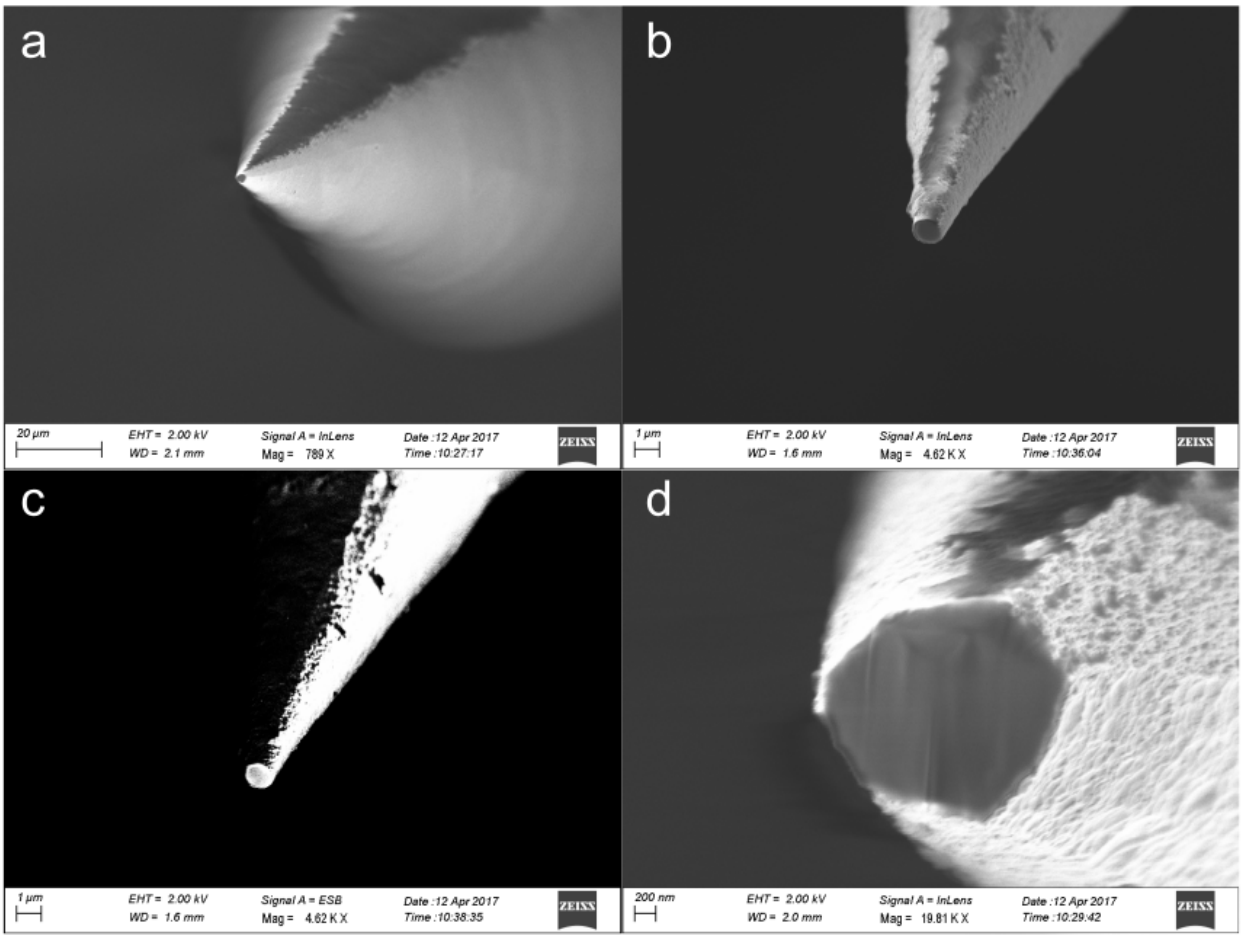

Figure B.6: SEM images taken using the Carl Zeiss FIBSEM. (a) Wide view of a SCQDM, with clear lead separation and an apex quantum dot. (b) Zoomed-in view of the SCQDM apex, showing the two leads and flat apex. (c) ESB detector, which is sensitive to atomic number, shows the gold lead (atomic number 79) clearly in white, but the aluminum lead (atomic number 13) blends in with the underlying silicon (atomic number 14). This image is a similar perspective as (b). (d) Zoomed in image of the flat apex. This QD is on the order of 1 um, much too large for SCQDM applications.

The Helios 650 FIBSEM is housed at the University of Michigan's Center for Materials Characterization. The main advantage of the Helios 650, in addition to its incredible SEM and FIB imaging capabilities, is the ability to monitor FIB mills in real time.

The SCQDM probes act as large antennas during the FIB milling stage and often move in response to the ion beam. Performing delicate and high precision cuts necessitated manual beam control during the milling stage, a functionality only the Helios 650 has. As can be seen throughout this thesis, the images and mills produced by the Helios 650 truly enabled this technology to be developed.

Interaction volume is an important quantity to consider when performing any type of charge imaging technique, whether it be ion or electron imaging. Essentially, the interaction volume is a measure of the volume a given beam current and accelerating voltage interacts with in a sample. High energy (voltage) high current beams tend to penetrate deeper into the sample, ejecting secondary and backscattered electrons from a depth of 100 nms or more. The resulting image, which is constructed from these electrons, encodes not just surface information, but composition of the underlying substrate. On the other hand, high acceleration voltages can also totally penetrate the sample, giving clear information on the surface without bulk electron poisoning. In the context of the SCQDM ignoring the interaction volume can lead to false conclusions and makes analysis more difficult. The thin nature of the aluminum leads and quantum dot means most imaging done is a combination of the aluminum and underlying silica. Near the tip apex at certain angles, the penetration direction may be transverse to the aluminum leads, resulting in the appearance of aluminum in locations where aluminum might not be, such as the apex quantum dot. Interaction volume is a general consideration when performing FIBSEM, but the unusual application and geometries involved in SCQDM probe imaging requires a solid understanding of this mechanism toward interpreting SEM images.

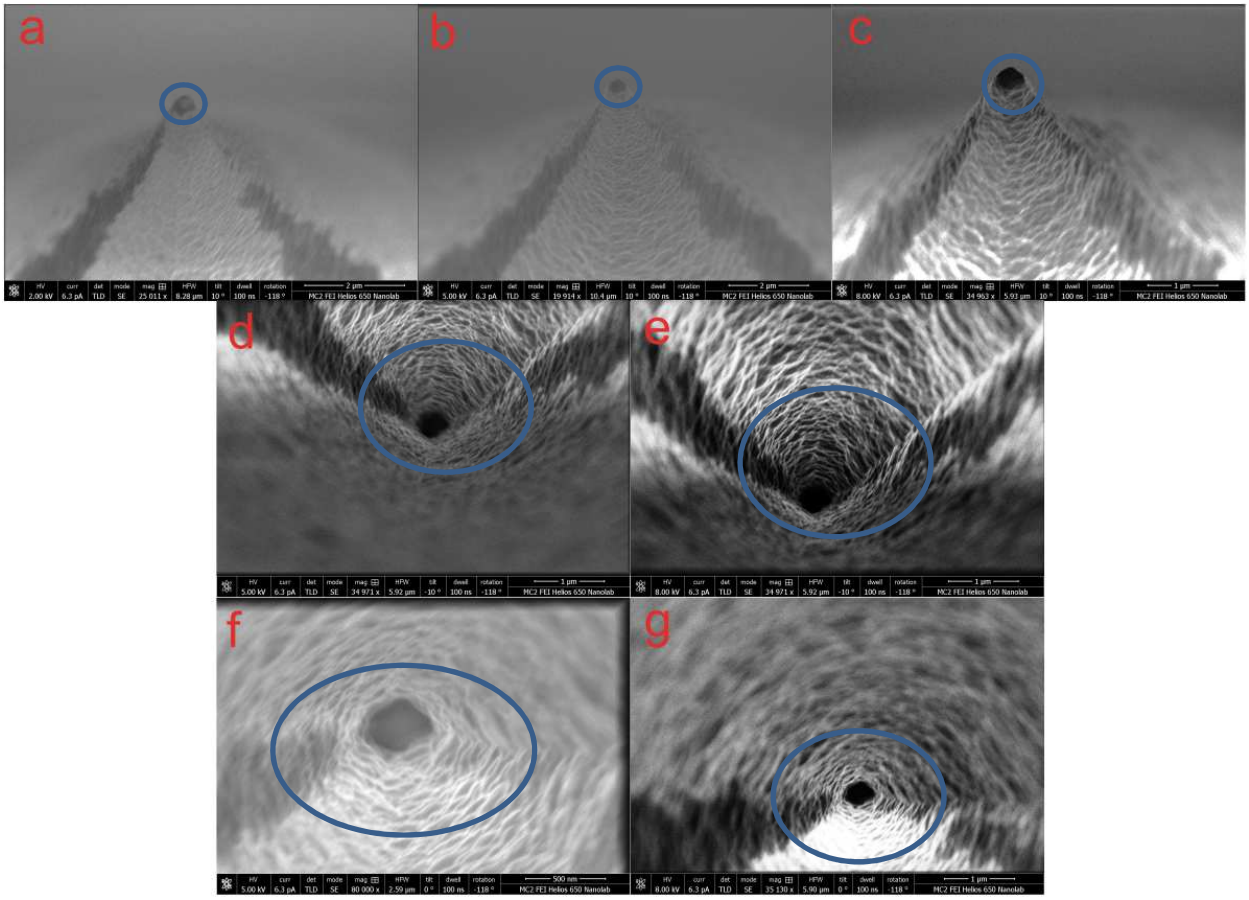

Figure B.7: SEM images using different acceleration voltages. Blue circles added for focus. (a-c) Three consecutive images of a SCQDM probe apex at (a) 2V, (b) 5V, and (c) 8V accelerating voltages. In (a), the apex quantum dot has a small portion in light grey, indicating a finite interaction volume with the aluminum surface layer on the back side of the probe. In (b), this light grey spot disappears, with (c) showing a much darker quantum dot area. This is consistent with the higher accelerating voltages (b-c) penetrating through the back-side layer of aluminum without backscattering interior electrons. (d-e) shows two images of the same quantum dot at different acceleration voltages. An accelerating voltage of 5V in (d) does not show clear lead separation, as indicated by overlapping areas of light grey to the right of the quantum dot. (e) was taken at 8V, showing a clearer image of the lead separation to the apex. (f-g) follow a similar trend, showing clearer lead separation at higher acceleration voltage. The discrepancy arises in (d-g) from penetrating and interacting with the interior glass probe, rather than the surface aluminum layer.

Dwell time is another important consideration. Due to the surface layer of aluminum oxide that forms natively, the surface of the SCQDM probes are poor conductors. Electron charge readily accumulates on the oxide layer, and dissipates only over time scales longer than the dwell time.

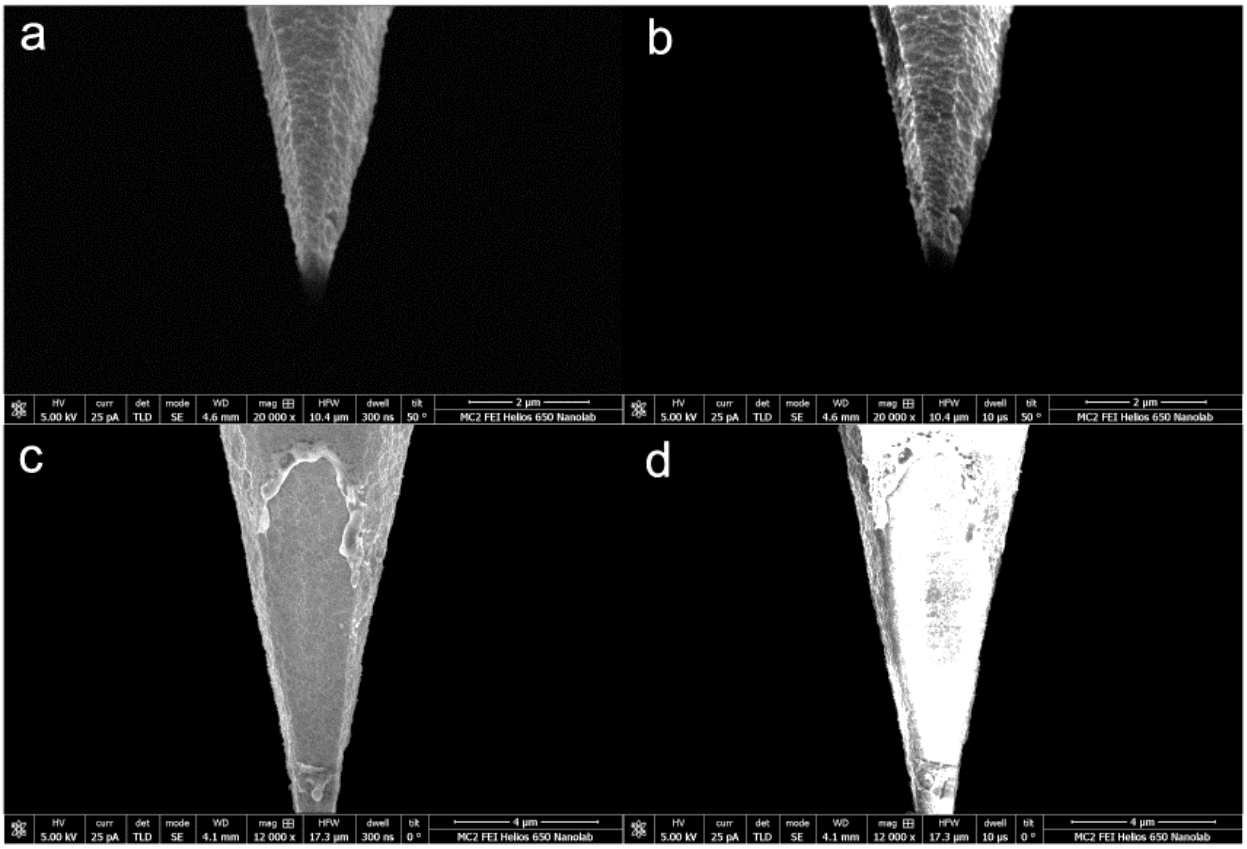

Figure B.8: Effects of dwell time on SEM image quality. (a-b) SEM images with dwell time of (a) 300 ns and (b) 10 us. The metal shown here is gold, a good conductor. The gold lead benefits from the additional exposure time, illuminating fine details as compared to the shorter dwell time. (c,d) SEM images with dwell times of (c) 300 ns and (d) 10 us. The metal shown here is aluminum, which forms a native oxide. Additionally, a large portion of the glass probe is uncovered. The prolonged dwell time in (d) results in charging effects, obscuring the image more readily clear in (c). (a,c) are integrations of 16 images taken at 300 ns exposure.

As a result, large dwell times can lead to charging effects, which obscure and distort the image.

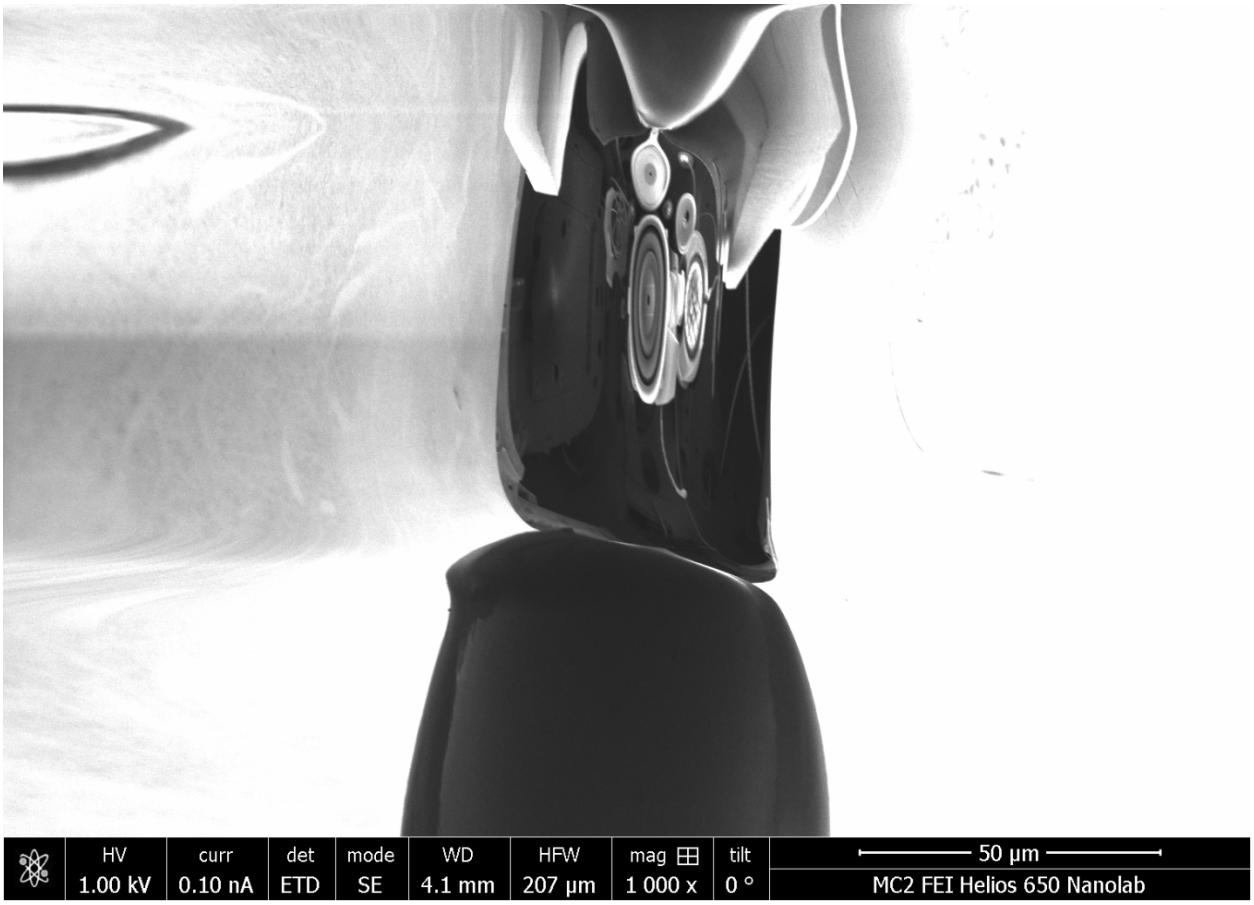

Figure B.9: High beam currents, prolonged exposure, and an insulating sample can cause strange distortions in the SEM images. Here, a prolonged exposure on a SCQDM probe without aluminum results in a complete distortion of the image due to an excess build-up of electrons.

APPENDIX C:

Majorana Theory Extended

Majorana physics is full of subtleties and complexity. Additional theoretical discussion is provided in this appendix to develop a general understanding of some aspects of these systems.

C.1 Strong Spin-Orbit Coupling

The second ingredient to realizing Majorana zero modes is strong spin-orbit coupling. Spin-orbit coupling is a relativistic interaction between a particle's intrinsic spin and momentum. Materials with strong spin-orbit interaction have restrictions on which combinations of spin and momentum can be taken by individual electrons, locking these degrees of freedom together. The spin-orbit interaction, once proximitized by a s-wave superconductor, introduces an effective momentum dependence into the pairing potential of Cooper pairs, allowing zero energy states to manifest.

Singlet, or s-wave, superconductivity discussed in the previous section conserves the spin degree of freedom.

$$Singlet\ (s\ wave) = |\uparrow\downarrow\rangle \qquad Triplet\ (p\ wave) = \begin{cases} |\uparrow\uparrow\rangle \\ |\uparrow\downarrow\rangle + |\downarrow\uparrow\rangle \\ |\downarrow\downarrow\rangle \end{cases} \tag{C.1}$$

The eigenstates of s-wave superconductors must necessarily have definite spin, including any MZMs in the system. As will be discussed in the next section, one can imagine totally spin-polarizing the system to achieve an effective spinless system, but nevertheless the spin signature will continue to exist. One way to remove spin as a conserved quantity is to introduce a strong spin-orbit coupling term to the Hamiltonian of the system

$$H_{SO} = \alpha \sigma_y k \tau_z \tag{C.2}$$

Where α determines the strength of the interaction, σ_y is the Pauli matrix in spin space, k is the momentum, and τ_z is the Pauli matrix in particle-hole space. In conjunction with an applied magnetic field in the z-direction which destroys Kramer's degeneracy, the spin-orbit interaction removes spin conservation, allowing an effective spinless system to manifest.

C.2 Magnetism / Localization / Separation

There are two ways to understand the role magnetism plays in Majorana physics. First, magnetism lifts the spin-degeneracy present in superconducting systems, allowing for a spin-polarized (effectively spinless) system. In spin degenerate systems, two MZMs would arise in the same spatial location, which is equivalent to a single zero energy fermionic mode. Magnetism intrinsically breaks time-reversal symmetry, something the strong spin-orbit interaction does not, lifting Kramer's degeneracy and allows the isolation of individual MZMs. Second, magnetism can be thought of as providing a control knob to transition between the trivial and topological phases. To change the topological

characteristics from trivial to non-trivial, a gap needs to be closed and reopened. The most natural gap in this system is the superconducting energy gap, which is first closed and then reopened into the topological phase by sweeping the magnetic field across the transition point. Magnetism can be introduced using an external magnetic field, magnetic atoms, or ferromagnetic heterostructures, the latter two which lift spin degeneracy locally.

Superconductivity, strong spin-orbit coupling, and magnetism are enough to create an effective topological superconductor. MZMs are excitations arising in topological superconductors, but there needs to exist a bulk-boundary correspondence between topologically distinct materials to localize these modes and resolve them experimentally. Further, the pair of MZMs need to be separated, reducing the pair's wavefunction overlap sufficiently enough to isolate each MZM and study/harness their interesting properties.

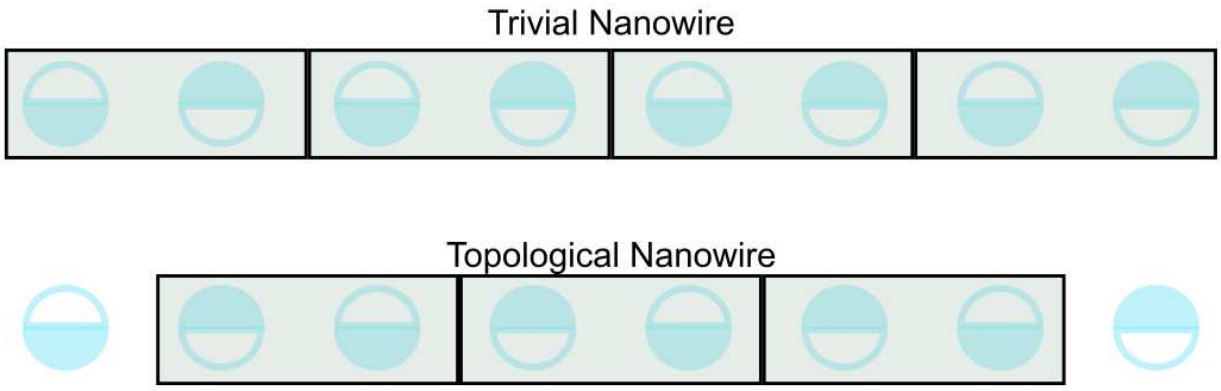

Figure C.1: Kitaev's toy model. A series of fermions (boxes) each comprised of two Majorana modes (circles). In the top configuration, the Majorana pairing is between two on-site Majorana modes and is topologically trivial. If instead, the Majorana pairing is done between two adjacent Majorana, two unpaired Majorana modes can be localized to either end.

The simplest manifestation of boundary MZMs is found in the Majorana nanowire platform, a realization of the Kitaev toy model proposed in the early 2000s.[12] Beginning

with a chain of fermions, which are further decomposed into two Majorana modes, it is possible to change the pairing of the Majorana modes to realize two localized MZMs at the ends of the nanowire platform. This cartoon pictures translates surprisingly well to realistic experimental setups, and is closely related to the SSH model, the simplest example of topology in nature.

C.3 Topological Physics

The discussion thus far has overlooked the topological aspect of this system. In part due to the history of our lab's involvement with topological insulators, a key component to several Majorana platforms, the following section will explore topological physics, from quantum hall insulators through Majorana topology. This section is not necessary for understanding how these excitations arise but provides a glimpse at the underlying topological order enabling this interesting physics.

C.3.1 Topology and Gapped Systems

Topology from a mathematical standpoint is the study of classes of objects which can be continuously deformed into one another. The somewhat infamous example is characterizing objects by the number of holes they possess.[49] In this classification scheme, a coffee cup and donut (holes=1) are the same topological class and can be smoothly deformed into one another. A sphere on the other hand (holes=0) cannot be smoothly deformed into a coffee cup, as it requires opening a hole. Topology in condensed matter physics takes the form of equivalent Hamiltonians. Specifically, if a system can be

adiabatically evolved into another, then both systems are part of the same topological class. This classification is ill-defined for metals, but by restricting the class of Hamiltonians to only those that contain an energy gap, this concept becomes well-defined and interesting physics arises.[49]

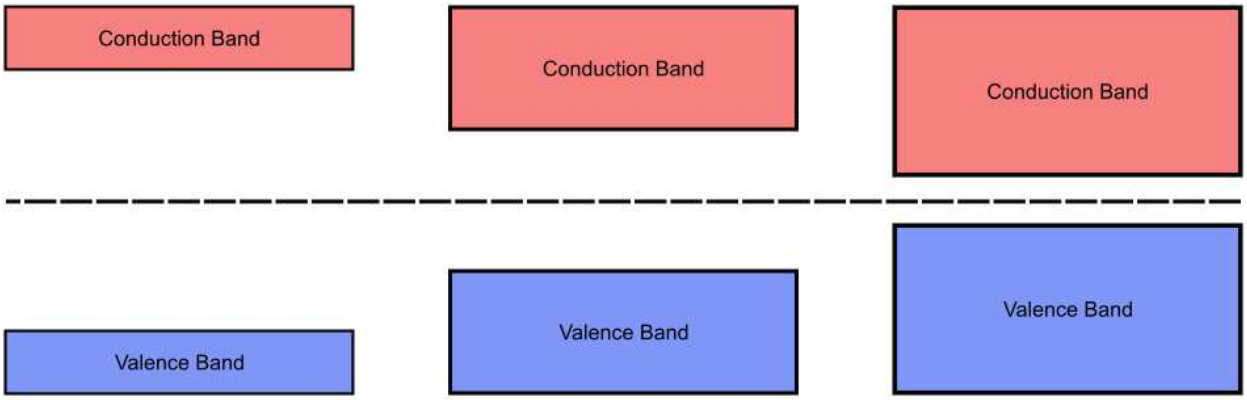

Figure C.2: Insulating systems with an energy gap can be smoothly deformed and remain in the same topological class. In this way, a large gap insulator (such as the vacuum) can be smoothly deformed into a smaller gap insulator, without changing topological class.

The number of holes determines the topological class of the coffee cup-donut-sphere, and the equivalency for condensed matter physics is the topological invariant, which takes on only discrete values as well. An entire zoo of interesting topological materials exists in different spatial dimensions and under different symmetries, each with a different topological invariant. In general, topological systems have one of three types of topological invariants. $\mathbb{Z}$ topological invariants takes on integer values (0,1,2,3,etc). $\mathbb{Z}_2$ topological invariants only have two values, either 0 or 1. And lastly, certain systems can have a $2\mathbb{Z}$ invariant, which takes on integer values (0,2,4,6,etc.).

A natural follow-up question to topological classifications is "what invokes a change in topological class?" In the simple coffee-donut-sphere classification, changing the

topological class involves a non-smooth deformation, namely puncturing the sphere or smushing the coffee cup/donut. The equivalent operation in the classification scheme for gapped systems is a non-adiabatic evolution of the system. In the well-defined case, this manifests as a closing and reopening of an energy gap, precisely because a closed energy gap has ill-defined topology. As topological invariant must change discreetly rather than continuously, the barrier between two topological distinct materials must have ill-defined topology. The nature of the gap, whether it separates the valence band and conduction (as is the case for insulators) or it separates electron and hole states (as is the case for superconductors) has implications for what the topological invariant is characterizing. Dimensionality and symmetry considerations are deciding factors as well. In general, the boundary between trivial and topological phases of matter is comprised of either metallic states (chiral or helical edge modes) or localized zero energy modes.[49]

C.3.2 Berry Phase

The adiabatic evolution of a Hamiltonian accumulates a global phase associated with the time evolution. Additionally, a geometric phase can be acquired if the adiabatic evolution is taken around a closed path in parameter space. This geometric phase is the Berry phase.[50] Over the course of the time and parameter space evolution the wavefunction picks up the total phase below, with the first exponential corresponding to the time-evolved phase and the second exponential corresponding to the parameter-evolved phase.[25] In the context of a Bloch wavefunction $|\psi(\boldsymbol{k})\rangle$ with energy $E(\boldsymbol{k})$ evolving over a closed loop in k-space

$$|\psi_m(\boldsymbol{k})\rangle = \exp[-\tfrac{i}{\hbar}\int_{t_i}^{t_f} E(\boldsymbol{k}(t))dt]e^{i\gamma(k)}|\psi_m(\boldsymbol{k})\rangle \quad \text{(C.3)}$$

where γ in this section refers to the Berry phase (in most sections this refers to the Majorana operators). The Berry phase is further defined as

$$\gamma = i\oint\langle\psi_m(\boldsymbol{k})|\nabla_{\boldsymbol{k}}\psi_m(\boldsymbol{k})\rangle d\boldsymbol{k} \quad \text{(C.4)}$$

The integrand above is known as the Berry connection A. This Berry phase can further be expressed as the surface integral of a Berry flux $F_m = \nabla \times A_m$. The topological invariant of any gapped system can then be calculated from this Berry flux, though the calculations vary widely in complexity and length. Luckily, the topological invariant for the Quantum Hall effect, the Chern invariant, has a relatively simple form

$$\nu_m = \tfrac{1}{2\pi}\int d^2k\, F_m \quad \text{(C.5)}$$

where k is the electron wave number. The total Chern number, which counts the number of edges mode in the Quantum Hall insulator, is the sum of ν over all the bands, an integer value.

The Berry flux provides a general path toward calculating any topological invariant for gapped systems. The purpose of the following section is to assign physical meaning to the topological invariant for each system.

C.3.3 Topological Invariant

The hallmark topological system is the quantum hall (QH) insulator.[51,52] The application of large perpendicular magnetic fields to certain samples causes the electrons

in the sample to fill Landau levels. The number of filled Landau levels corresponds to the topological invariant of the system, the Chern number. These filled Landau levels represent filled bands in the interior, making this system a bulk insulator. As the interface between the quantum hall insulator and the vacuum delineates a change in topology, metallic edge modes exist at the boundary, the number of which is equal to the Chern number. The Chern number is a $\mathbb{Z}$ topological invariant.

A closely related system which obeys time reversal symmetry is the quantum spin hall insulator (QSH).[53,54] The QSH insulator is characterized by a $\mathbb{Z}_2$ topological invariant. The topological state then corresponds to the presence of two spin-orbit coupled edge modes, and the trivial state corresponds to a trivial bulk insulator with no edge modes. The Quantum Anomalous Hall insulator (QAH), though breaking time reversal symmetry, is also a $\mathbb{Z}_2$ invariant, with the topological state corresponding to a single spin-polarized edge mode.[55]

Generalizing the QSH insulator to three dimensions is a material known as a topological insulator (TI).[49,56,57] The TI is characterized by the presence of topologically protected surface states which are conductive surface states with strong spin-orbit coupling. These helical edge modes form the Dirac cone, a linear energy dispersion of bands crossing the Fermi level.[57] Figure C.4 shows the Dirac cone, surface bands, along with the bulk conduction and valence bands. The surface states are additionally protected by time revseral symmetry. A $\mathbb{Z}_2$ topological invariant describes this state, which is a function of three QSH topological invariants.

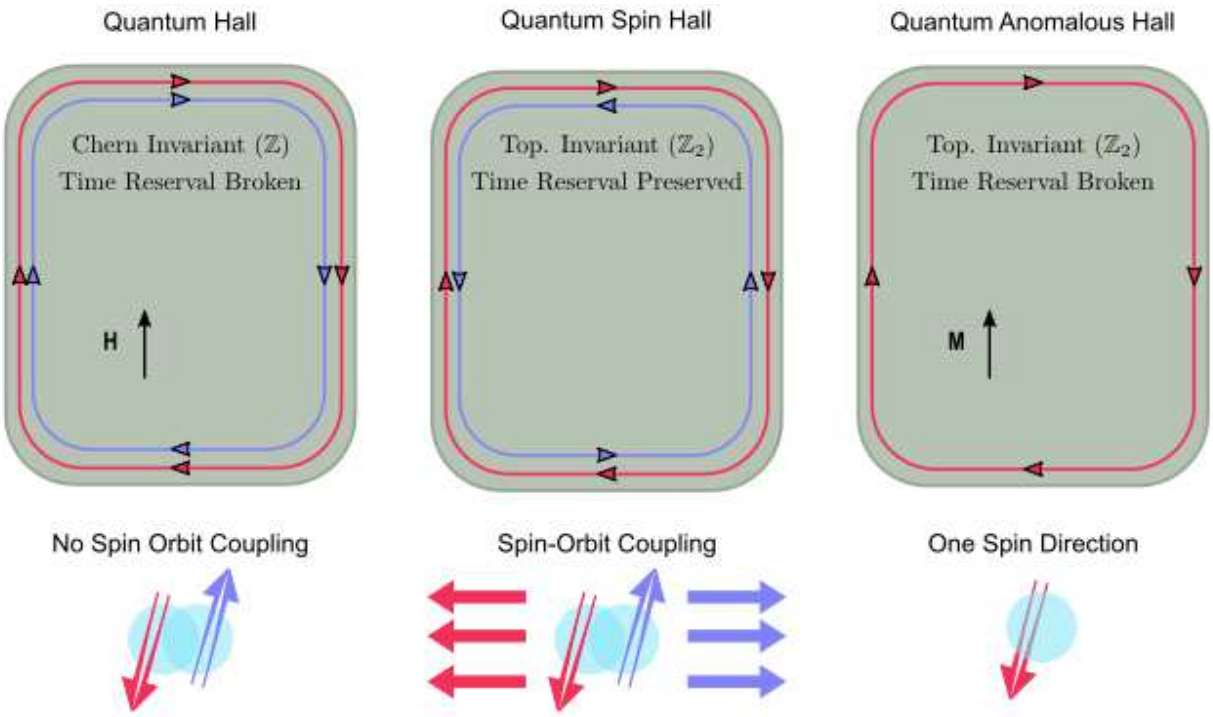

Figure C.3: Three different 2D topological systems. Left: Quantum Hall states are characterized by chiral edge modes, the number of which determines the topological invariant. Large magnetic fields are responsible for this state, which breaks time reversal symmetry. Middle: Quantum Spin Hall insulators, sometimes referred to as 2D topological insulators, are characterized by strong spin-orbit coupled edge modes, with spin-up traveling one direction and spin-down traveling the other. A $\mathbb{Z}_2$ invariant describes the system without (0) and with (1) these helical edge modes. Right: The Quantum Anomalous Hall insulator breaks time reversal symmetry locally through ferromagnetism and is characterized by a helical edge mode. Like the QSH, this system is defined by a $\mathbb{Z}_2$ invariant.

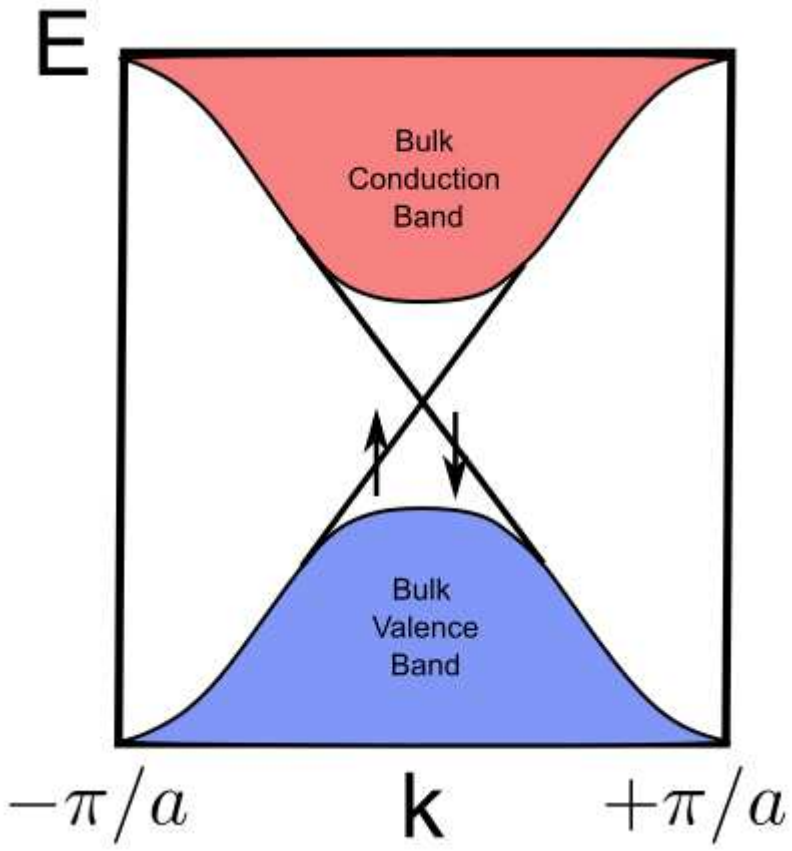

Figure C.4: The Dirac cone is the consequence of time reversal symmetry and strong spin-orbit coupling. Bulk band diagrams of topological and trivial insulators are indistinguishable. Only when the surface states are included (spin-polarized bands shown in black) does the difference become apparent, pointing to the importance of the bulk-boundary correspondence.

The preceding discussion was in relation to insulators, but ultimately Majorana physics is concerned with the topological phase transition of superconductors, another energy gapped system. As a superconductor is cooled below its critical temperature it undergoes a traditional phase change from the metallic to superconducting state, opening a gap in the electronic density of states. This phase transition is not topological, as metals in general are poorly defined entities with respect to the classification scheme chosen here. Nevertheless, the topological classification of a normal superconductor is well-defined. The

topological invariant describing topological superconductors is the fermion parity of the ground state, which changes at every zero-energy crossing i.e. superconducting gap closing and reopening. This topological invariant is referred to as the sign of the Pfaffian, a connection which will not be explored here.[58] The boundary between a topological superconductor and trivial superconductor are where MZMs are found.

C.4 Quantized Majorana Conductance

As we have explored, Majorana zero modes arise as boundary excitations in topological superconductors. The tasks of experimentalist working in this field is to provide robust signatures of Majorana zero modes. To date, there is no conclusive evidence of non-Abelian Majorana zero modes. The most prominent proposed signature of MZMs tested is the presence of a quantized zero-bias peak in tunneling conductance.[14,15,20] The following section will describe this experiment and its difficulties realizing a robust signature, which further motivates the need for another type of measurement of MZMs using QDs, the focus of the SCQDM. No quantized Majorana conductance was measured for the purpose of this thesis.

Quantized zero-bias conductance peaks remain an important measure of MZMs and are the first measurement performed on systems thought to support MZMs. In recent years, it has been discovered more trivial Andreev bound states (ABSs) and Shiba states tend to mimic this signal, but nevertheless it is a valuable tool in an experimentalist's toolbox.[16]

To understand the origin of the quantized zero-bias conductance peak in the presence of a MZM, it is best to review what happens to electrons incident on a barrier. Two processes can occur for a metal-barrier-metal (N-B-N) system when an applied voltage attempts to tunnel electrons through the barrier from left to right. The electron from the left is either transmitted through the barrier or reflected back off the barrier. In metal-barrier-superconductor (N-B-S) systems, there is an additional reflection process possible. The superconducting energy gap Δ restricts electronic states from existing in an energy band about the Fermi level in the superconductor. For incident electrons with energy $eV \ll \Delta$, there is not an electronic state to tunnel into, and further, the fundamental charge carriers in superconductors are Cooper pairs, not electrons. Electronic states are forbidden from existing in the superconducting energy gap. Andreev reflection provides an alternative to normal reflection and describes the process by which an electron incident to the barrier injects a Cooper pair into the superconductor while reflecting a hole. This conversion of incident electron to reflected hole results in a net 2e transfer from the metal to the superconductor, making charge transfer from metal to superconductor and vice-versa possible. Andreev reflection is restricted to incident electrons with energy below the superconducting energy gap, which happens to be the energy range over which MZM exist. Incident electrons above the superconducting energy gap can transmit as electrons and contribute to the overall current.

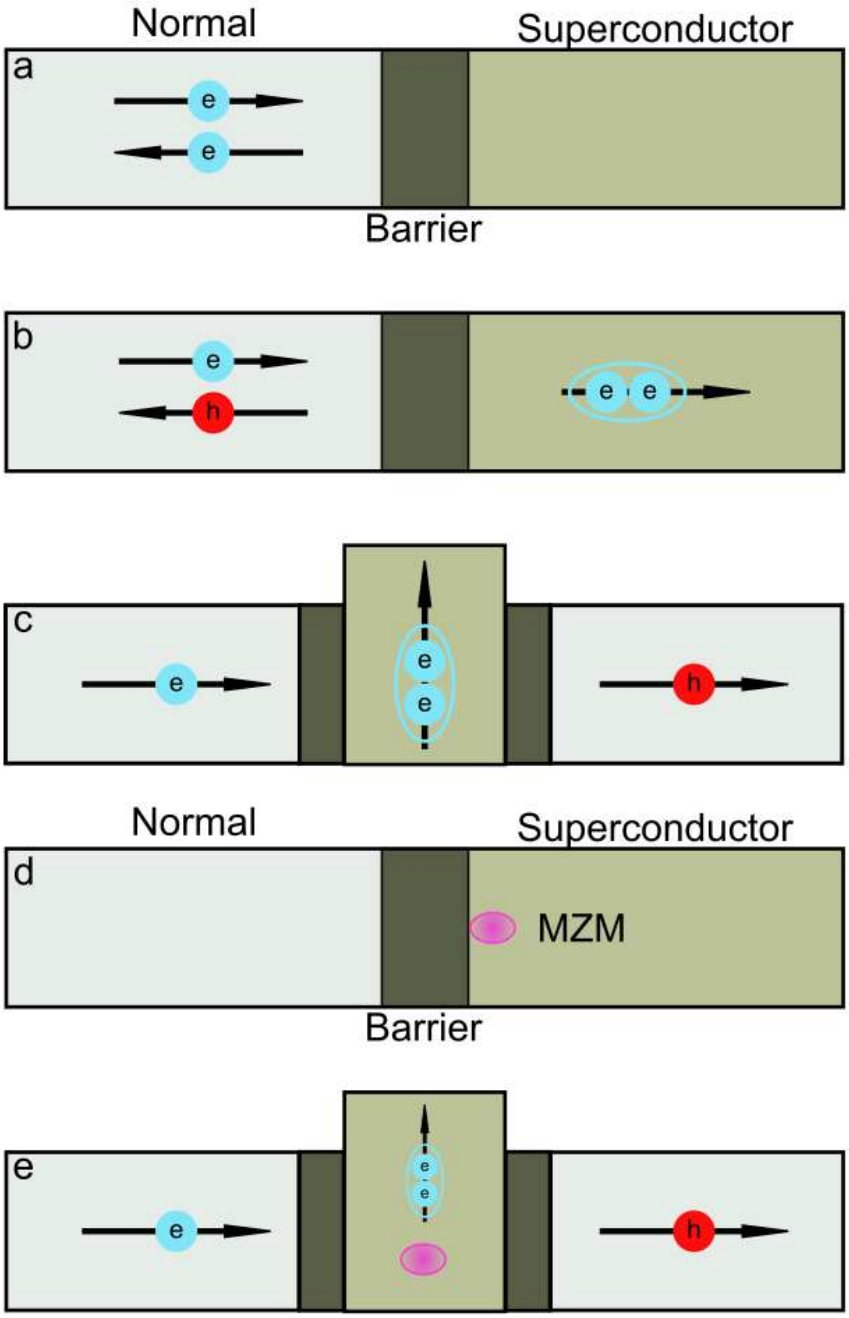

Figure C.5: Phenomena at normal metal-barrier-superconductor interfaces. (a) Reflection of an electron at the barrier. (b) Andreev reflection and injection of a Cooper pair at the barrier. (c) Andreev reflection can be modeled as a double barrier transmission problem, with one electron lead and one hole lead. (d) Metal-barrier-superconductor interface supporting a MZM. (e) Modeling (d) as a double barrier transmission problem, perfectly resonant Andreev reflection occurs, guaranteeing quantized conductance due to the presence of the MZM. Unfortunately, this phenomenon is readily mimicked by more mundane physics, such as Andreev bound states.

It is perhaps more informative to model Andreev reflection as a double barrier transmission problem. The particle-hole symmetry of superconductors and the requirement that any charge injected into the superconductor must be in increments of 2e allows one to think of this Andreev reflection process as transmission from an electron-like lead, through a superconductor, into a hole-like lead. With this image in mind, we can define the Andreev reflection amplitude r_{eh}, which when squared gives the probability of tunneling through the double barrier. This reflection amplitude, best thought of as a transmission coefficient, is directly proportional to the conductance

$$G(V) = 2G_0|r_{eh}^2| \tag{C.6}$$

The quantum of conductance, $G_0 = \frac{e^2}{h}$, is modified by a factor of two to account for the injection of Cooper pairs, whose fundamental charge is 2e. In the context of MZM, the quantized conductance peak sought after has this additional factor of 2. The value of the Andreev reflection coefficient is determined by the strength of the barrier and applied voltage under normal circumstances.

The presence of a bound state at the interface modifies the transmission characteristics drastically. If the bound state energy is resonant with the energy of the incident electron, the conductance is enhanced greatly. This phenomenon is very general and independent of the nature of the bound state. The quantized nature of the conductance peak involving MZMs requires a deeper dive into quantum mechanics and topology.

Transport through a NS interface can be described as a scattering problem. The reflection matrix for a NS interface is

$$r(V) = \begin{pmatrix} r_{ee} & r_{eh} \\ r_{he} & r_{hh} \end{pmatrix} \tag{C.7}$$

Each term in the reflection matrix describes a particular reflection process. r_{ee} and r_{hh} describe normal reflection at the interface for electrons and holes, respectively. r_{eh} and r_{he} describe Andreev reflections for an incident electron (hole) Andreev reflecting as a hole (electron). For low applied voltage ($eV \ll \Delta$), these are the only possible options for incident particles and as a result the reflection matrix is unitary, which gives the following constraints to the squared amplitudes.

$$|r_{ee}|^2 + |r_{eh}|^2 = |r_{hh}|^2 + |r_{he}|^2 = 1 \tag{C.8}$$

It is clear incident particles can only normal or Andreev reflect, but we still have no clear path with quantum mechanics arguments to arrive at quantized Majorana conductance. We must appeal to topology to gain any further ground.

MZMs are found in topological superconductors, whose $\mathbb{Z}_2$ invariant is the sign of the Pfaffian. At the boundary between a normal metal and topological superconductor, one that supports Majorana zero modes, the topological invariant must change discreetly. Topological invariants are quite often the determinants of some matrix. In this case, we will discuss the determinant of the reflection matrix r and define our topological invariant Q as $Q = det(r_o)$, which is to be understood as the reflection matrix at zero applied voltage (energy). Particle-hole symmetry dictates the determinant of r_o must be Q=±1. With this constraint, and recalling Equation C.7, the only possible conditions that satisfy both constraints are perfect normal reflection or perfect Andreev reflection. Perfect normal

reflection results in net zero conductance, whereas perfect Andreev reflection results in quantized Majorana conductance of $2G_0$.

Measuring quantized Majorana conductance is a great first step towards studying MZMs, but unfortunately more pedestrian effects can give rise to similar conductance peaks. The most prominent culprits are other sub-gap states. Andreev bound states, as the name might suggest, are responsible for sub-gap states at superconducting interfaces, whether that be a NS interface or superconducting vortex.[59] For instance, below is a measurement I performed of a zero-bias conductance peak in a superconducting vortex core on pure Nb at 4.2K performed using STM.

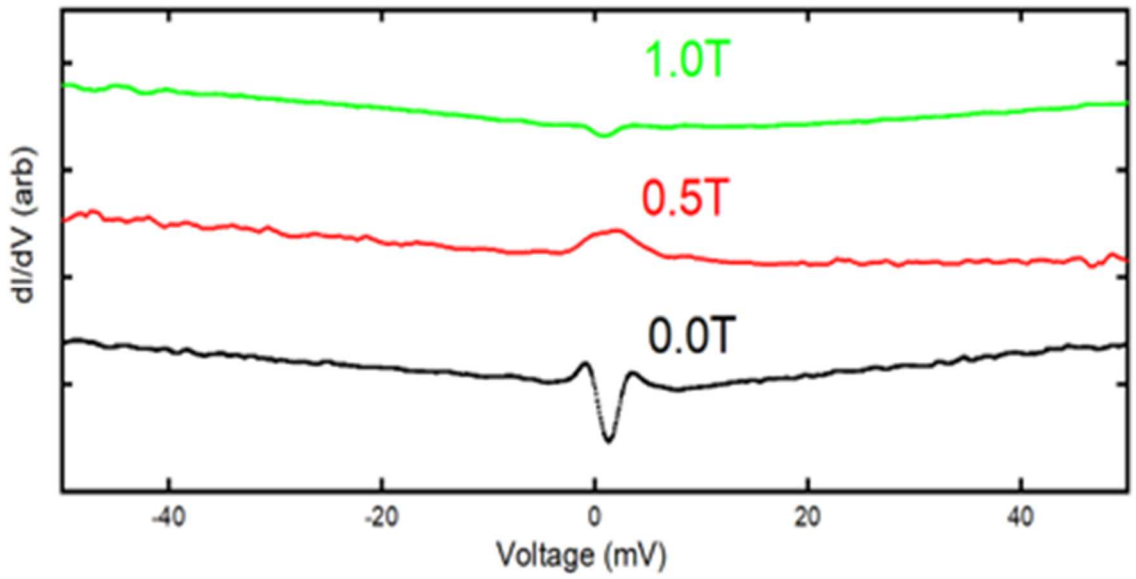

Figure C.6: STS data on pure Nb in finite magnetic field. At 0.5T, a robust zero bias peak is formed, indicating the presence of bound states inside a superconducting vortex. Pure Nb does not support Majorana zero modes.

In fact, Andreev bound states are expected to coalesce into MZMs as a changing magnetic field induces the topological phase transition.[10] Yu-Shiba-Rusinov states, sub-gap states

arising from magnetic impurities, can also mimic these signatures, a major problem for Majorana platforms utilizing magnetic atoms or ferromagnetic layers.[60] Another culprit is Caroli-de Gennes-Martricon states, low energy excitations within vortex cores of type-II superconductors.[61] The symmetric, low-energy nature of these states make it difficult to resolve them, and often low-energy resolution results in these states forming a symmetric zero-bias peak. A recent paper by in fact suggest every zero-bias peak measurement in the Majorana nanowire platform has arisen from these nontopological effects.[15] The outlook for this measurement providing a smoking gun signature of MZMs is hopeful, but there are other attractive avenues to explore. These present difficulties contributed to the desire to develop the SCQDM.

BIBLIOGRAPHY

BIBLIOGRAPHY

[1] Binnig, Gerd, and Heinrich Rohrer. "Scanning tunneling microscope." U.S. Patent 4,343,993, issued August 10, 1982.Yoo, M. et al. Scanning Single-Electron Transistor Microscopy: Imaging Individual Charges. Science 25, 579-582 (1997).

[2] Tessmer, S. H., P. I. Glicofridis, R. C. Ashoori, L. S. Levitov, and M. R. Melloch. "Subsurface charge accumulation imaging of a quantum Hall liquid." Nature 392, no. 6671 (1998): 51-54.

[3] Ashoori, R. C., H. L. Stormer, J. S. Weiner, L. N. Pfeiffer, S. J. Pearton, K. W. Baldwin, and K. W. West. "Single-electron capacitance spectroscopy of discrete quantum levels." *Physical review letters* 68, no. 20 (1992): 3088.

[4] Liu, Dong E., Alex Levchenko, and Roman M. Lutchyn. "Majorana zero modes choose Euler numbers as revealed by full counting statistics." *Physical Review B* 92, no. 20 (2015): 205422.

[5] Majorana, Ettore. "Teoria simmetrica dell'elettrone e del positrone." *Il Nuovo Cimento (1924-1942)* 14, no. 4 (1937): 171.Moore, G., & Read, N. (1991). Nonabelions in the fractional quantum Hall effect. Nuclear Physics B, 360(2-3), 362-396.

[6] Kitaev, A. Yu. "Fault-tolerant quantum computation by anyons." *Annals of Physics* 303, no. 1 (2003): 2-30.

[7] Nayak, Chetan, Steven H. Simon, Ady Stern, Michael Freedman, and Sankar Das Sarma. "Non-Abelian anyons and topological quantum computation." *Reviews of Modern Physics* 80, no. 3 (2008): 1083.

[8] Lutchyn, Roman M., Erik PAM Bakkers, Leo P. Kouwenhoven, Peter Krogstrup, Charles M. Marcus, and Yuval Oreg. "Majorana zero modes in superconductor–semiconductor heterostructures." *Nature Reviews Materials* 3, no. 5 (2018): 52-68.

[9] Qi, Xiao-Liang, and Shou-Cheng Zhang. "Topological insulators and superconductors." *Reviews of Modern Physics* 83, no. 4 (2011): 1057.

[10] Kitaev, A. Yu. "Unpaired Majorana fermions in quantum wires." *Physics-Uspekhi* 44, no. 10S (2001): 131.

[11] Fu, Liang, and Charles L. Kane. "Superconducting proximity effect and Majorana fermions at the surface of a topological insulator." *Physical review letters* 100, no. 9 (2008): 096407.

[12] Mourik, Vincent, Kun Zuo, Sergey M. Frolov, S. R. Plissard, Erik PAM Bakkers, and Leo P. Kouwenhoven. "Signatures of Majorana fermions in hybrid superconductor-semiconductor nanowire devices." *Science* 336, no. 6084 (2012): 1003-1007.

[13] Zhang, Hao, Chun-Xiao Liu, Sasa Gazibegovic, Di Xu, John A. Logan, Guanzhong Wang, Nick Van Loo et al. "Quantized majorana conductance." *Nature* 556, no. 7699 (2018): 74-79.

[14] Pan, Haining, and S. Das Sarma. "Physical mechanisms for zero-bias conductance peaks in Majorana nanowires." *Physical Review Research* 2, no. 1 (2020): 013377.

[15] Liu, Dong E., and Harold U. Baranger. "Detecting a Majorana-fermion zero mode using a quantum dot." *Physical Review B* 84, no. 20 (2011): 201308.

[16] Wang, Dongfei, Lingyuan Kong, Peng Fan, Hui Chen, Shiyu Zhu, Wenyao Liu, Lu Cao et al. "Evidence for Majorana bound states in an iron-based superconductor." *Science* 362, no. 6412 (2018): 333-335.

[17] Nadj-Perge, Stevan, Ilya K. Drozdov, Jian Li, Hua Chen, Sangjun Jeon, Jungpil Seo, Allan H. MacDonald, B. Andrei Bernevig, and Ali Yazdani. "Observation of Majorana fermions in ferromagnetic atomic chains on a superconductor." *Science* 346, no. 6209 (2014): 602-607.

[18] Sun, Hao-Hua, Kai-Wen Zhang, Lun-Hui Hu, Chuang Li, Guan-Yong Wang, Hai-Yang Ma, Zhu-An Xu et al. "Majorana zero mode detected with spin selective Andreev reflection in the vortex of a topological superconductor." *Physical review letters* 116, no. 25 (2016): 257003.

[19] Stuart Tessmer, "Quasiparticle bound states in normal metal/superconductor structures probed by scanning tunneling microscopy," (University of Illinois at Urbana-Champaign, 1995).

[20] Chen, C. Julian. *Introduction to scanning tunneling microscopy*. Vol. 4. Oxford University Press on Demand, 1993.

[21] Besocke, Karl. "An easily operable scanning tunneling microscope." *Surface Science* 181, no. 1-2 (1987): 145-153.

[22] Wang, Zhenyu, Jorge Olivares Rodriguez, Lin Jiao, Sean Howard, Martin Graham, G. D. Gu, Taylor L. Hughes, Dirk K. Morr, and Vidya Madhavan. "Evidence for dispersing 1D Majorana channels in an iron-based superconductor." *Science* 367, no. 6473 (2020): 104-108.

[23] Chamon, Claudio, Mark O. Goerbig, Roderich Moessner, and Leticia F. Cugliandolo, eds. *Topological Aspects of Condensed Matter Physics: École de Physique Des Houches, Session CIII, 4-29 August 2014*. Vol. 103. Oxford University Press, 2017.

[24] Kasha, Michael, H. R. Rawls, and M. Ashraf El-Bayoumi. "The exciton model in molecular spectroscopy." *Pure and Applied Chemistry* 11, no. 3-4 (1965): 371-392.

[25] Wimmer, Michael, A. R. Akhmerov, J. P. Dahlhaus, and C. W. J. Beenakker. "Quantum point contact as a probe of a topological superconductor." *New Journal of Physics* 13, no. 5 (2011): 053016.

[26] Beenakker, C. W. J. "Search for Majorana fermions in superconductors." *Annu. Rev. Condens. Matter Phys.* 4, no. 1 (2013): 113-136.

[27] London, Fritz, and Heinz London. "The electromagnetic equations of the supraconductor." *Proceedings of the Royal Society of London. Series A-Mathematical and Physical Sciences* 149, no. 866 (1935): 71-88.

[28] Bardeen, John, Leon N. Cooper, and John Robert Schrieffer. "Theory of superconductivity." *Physical review* 108, no. 5 (1957): 1175.

[29] Tinkham, Michael. *Introduction to superconductivity*. Courier Corporation, 2004.

[30] Nakamura, James, Shuang Liang, Geoffrey C. Gardner, and Michael J. Manfra. "Direct observation of anyonic braiding statistics." *Nature Physics* 16, no. 9 (2020): 931-936.

[31] Leijnse, Martin, and Karsten Flensberg. "Scheme to measure Majorana fermion lifetimes using a quantum dot." *Physical Review B* 84, no. 14 (2011): 140501.

[32] Golub, A., I. Kuzmenko, and Y. Avishai. "Kondo correlations and Majorana bound states in a metal to quantum-dot to topological-superconductor junction." *Physical Review Letters* 107, no. 17 (2011): 176802.

[33] Cheng, Meng, Michael Becker, Bela Bauer, and Roman M. Lutchyn. "Interplay between Kondo and Majorana interactions in quantum dots." *Physical Review X* 4, no. 3 (2014): 031051.

[34] Deng, M. T., S. Vaitiekėnas, Esben Bork Hansen, Jeroen Danon, M. Leijnse, Karsten Flensberg, Jesper Nygård, P. Krogstrup, and Charles M. Marcus. "Majorana bound state in a coupled quantum-dot hybrid-nanowire system." *Science* 354, no. 6319 (2016): 1557-1562.

[35] Grabert, Hermann, and Michel H. Devoret, eds. *Single charge tunneling: Coulomb blockade phenomena in nanostructures*. Vol. 294. Springer Science & Business Media, 2013.

[36] Likharev, Konstantin K. "Single-electron devices and their applications." *Proceedings of the IEEE* 87, no. 4 (1999): 606-632.

[37] Ashoori, R. C., H. L. Stormer, J. S. Weiner, L. N. Pfeiffer, S. J. Pearton, K. W. Baldwin, and K. W. West. "Single-electron capacitance spectroscopy of a few electron box." *Physica B: Condensed Matter* 189, no. 1-4 (1993): 117-124.

[38] Tao, Miaomiao, Yonglong Jin, Ning Gu, and Lan Huang. "A method to control the fabrication of etched optical fiber probes with nanometric tips." *Journal of Optics* 12, no. 1 (2009): 015503.

[39] Lazarev, Alexander, Nicholas Fang, Qi Luo, and Xiang Zhang. "Formation of fine near-field scanning optical microscopy tips. Part I. By static and dynamic chemical etching." *Review of scientific instruments* 74, no. 8 (2003): 3679-3683.

[40] McLeod, Euan, and Aydogan Ozcan. "Nanofabrication using near-field optical probes." *Journal of laboratory automation* 17, no. 4 (2012): 248-254.

[41] Benjamin Ezekiel Feldman, "Measurements of interaction driven states in monolayer and bilayer graphene," (Harvard University. 2013)

[42] Sedlmayr, Nicholas, E. W. Goodwin, Michael Gottschalk, Ian M. Dayton, Can Zhang, Erik Huemiller, Reza Loloee et al. "Dirac surface states in superconductors: a dual topological proximity effect." *arXiv preprint arXiv:1805.12330* (2018).

[43] Dayton, Ian M., Nicholas Sedlmayr, Victor Ramirez, Thomas C. Chasapis, Reza Loloee, Mercouri G. Kanatzidis, Alex Levchenko, and Stuart H. Tessmer. "Scanning tunneling microscopy of superconducting topological surface states in Bi 2 Se 3." *Physical Review B* 93, no. 22 (2016): 220506.

[44] Trang, C. X., N. Shimamura, K. Nakayama, S. Souma, K. Sugawara, I. Watanabe, K. Yamauchi et al. "Conversion of a conventional superconductor into a topological superconductor by topological proximity effect." *Nature communications* 11, no. 1 (2020): 1-6.

[45] Romanowich, Megan, Mal-Soon Lee, Duck-Young Chung, S. D. Mahanti, Mercouri G. Kanatzidis, and Stuart H. Tessmer. "Interplay of topological surface and bulk electronic states in Bi 2 Se 3." *Physical Review B* 87, no. 8 (2013): 085310.

[46] Sedlmayr, Nicholas, and Alex Levchenko. "Hybridization mechanism of the dual proximity effect in superconductor-topological insulator interfaces." *arXiv preprint arXiv:2010.14066* (2020).

[47] Hasan, M. Zahid, and Charles L. Kane. "Colloquium: topological insulators." *Reviews of modern physics* 82, no. 4 (2010): 3045.

[48] Berry, Michael Victor. "Quantal phase factors accompanying adiabatic changes." *Proceedings of the Royal Society of London. A. Mathematical and Physical Sciences* 392, no. 1802 (1984): 45-57.

[49] Prange, R. E., and S. M. Girvin. "The Quantum Hall effect, Springer verlag." *New York* (1990).

[50] Klitzing, K. V., Gerhard Dorda, and Michael Pepper. "New method for high-accuracy determination of the fine-structure constant based on quantized Hall resistance." *Physical Review Letters* 45, no. 6 (1980): 494.

[51] Kane, Charles L., and Eugene J. Mele. "Z 2 topological order and the quantum spin Hall effect." *Physical review letters* 95, no. 14 (2005): 146802.

[52] Bernevig, B. Andrei, and Shou-Cheng Zhang. "Quantum spin Hall effect." *Physical review letters* 96, no. 10 (2006): 106802.

[53] Haldane, F. Duncan M. "Model for a quantum Hall effect without Landau levels: Condensed-matter realization of the" parity anomaly"." *Physical review letters* 61, no. 18 (1988): 2015.

[54] Fu, Liang, Charles L. Kane, and Eugene J. Mele. "Topological insulators in three dimensions." *Physical review letters* 98, no. 10 (2007): 106803.

[55] Moore, Joel E., and Leon Balents. "Topological invariants of time-reversal-invariant band structures." *Physical Review B* 75, no. 12 (2007): 121306.

[56] Levin, Michael, Bertrand I. Halperin, and Bernd Rosenow. "Particle-hole symmetry and the Pfaffian state." *Physical review letters* 99, no. 23 (2007): 236806.

[57] Andreev, A. F. "The thermal conductivity of the intermediate state in superconductors." *Журнал экспериментальной и теоретической физики* 46, no. 5 (1964): 1823-1828.

[58] Li, Jian, Sangjun Jeon, Yonglong Xie, Ali Yazdani, and B. Andrei Bernevig. "Majorana spin in magnetic atomic chain systems." *Physical Review B* 97, no. 12 (2018): 125119.

[59] Caroli, C., P. G. De Gennes, and J. Matricon. "Bound fermion states on a vortex line in a type II superconductor." *Physics Letters* 9, no. 4 (1964): 307-309.